Summer 8-23-2019

Mechanisms of Ice Core Stable Isotope Variability in the Upper Kaskawulsh-Donjek Region, St. Elias Mountains, Yukon, Canada

Erin A. McConnell
University of Maine, erin.mcconnell@maine.edu

Recommended Citation

MECHANISMS OF ICE CORE STABLE ISOTOPE VARIABILITY IN THE UPPER KASKAWULSH-DONJEK

REGION, ST. ELIAS MOUNTAINS, YUKON CANADA

By

Erin McConnell

B.A. Dartmouth College, 2017

A THESIS

Submitted in Partial Fulfillment of the

Requirements for the Degree of

Master of Science

(in Quaternary and Climate Studies)

The Graduate School

The University of Maine

August 2019

Advisory Committee:

Dr. Karl Kreutz, Professor of Earth and Climate Sciences and Climate Change Institute, Advisor

Dr. Bradfield Lyon, Associate Research Professor of Earth and Climate Sciences and Climate Change Institute

Dr. Kristin Schild, Research Assistant Professor of Earth and Climate Sciences and Climate Change Institute

Dr. Dominic Winski, Research Assistant Professor of Earth and Climate Sciences and Climate Change Institute

MECHANISMS OF ICE CORE STABLE ISOTOPE VARIABILITY IN THE UPPER KASKAWULSH-DONJEK

REGION, ST. ELIAS MOUNTAINS, YUKON CANADA

By Erin McConnell

Thesis Advisor: Dr. Karl Kreutz

An Abstract of the Thesis Presented
in Partial Fulfillment of the Requirements for the
Degree of Master of Science
(in Quaternary and Climate Studies)
August 2019

I use instrumental and ice core records to examine drivers of observed isotope variability in the Upper Kaskawulsh-Donjek (UKD) region of the St. Elias Mountains, Yukon, Canada over the time frame of instrument-proxy overlap (mid-1900s to present). One of the drivers of post-depositional isotope signal alteration is the vertical percolation of meltwater from the glacier surface through shallow layers of snow, which causes a reduction in the amplitude of the isotope signal recorded in ice cores. I examine isotope signal preservation in two sites in the St. Elias Mountains: Eclipse Icefield and Icefield Divide. These sites are relatively close (~30 km apart and 414 m elevation difference), yet display marked differences in melt amounts and isotope signal preservation related a ~1.8 °C increase in temperature along the downward altitudinal transect from Eclipse Icefield to Icefield Divide. The increase in melt and loss of isotope signal preservation in response to this relatively small temperature rise suggests that the isotope signal at Eclipse Icefield will begin to degrade by the mid-21st century if rapid Arctic warming continues as projected. However, recent evidence has shown that temperatures in northwestern Canada have already exceeded those of the Holocene Thermal Maximum. This indicates that, given Eclipse Icefield's lack of melt-related signal alteration at present, its ice may contain a complete and unaltered record of *past* regional climate variability through the Holocene— regardless of its ability to

record climate variability in the near future. Extending this analysis to other ice core sites in the Arctic, I identify a meteorological threshold for melt-related signal alteration, characterized by high mean summer temperatures (approximately -1.5 °C and above) and low accumulation rates (less than ~1.2 m water-equivalent snowfall per year).

In addition, I investigate mechanisms driving observed seasonality in the Eclipse Icefield isotope record using instrumental records and climate reanalysis products, which summarize broad-scale meteorological patterns. A local weather station record from Icefield Divide shares 15% variance, at most, with the Eclipse stable isotope timeseries on annual and seasonal timescales. Seasonal anomaly composites of sea level pressure fields and geopotential height at the surface and mid-troposphere, which are indicators of atmospheric circulation, show the most consistent patterns during cold seasons with high isotope ratios and high deuterium excess values. These patterns are characteristic of the Pacific-North America atmospheric teleconnection pattern and its expression at sea level, the Aleutian Low Pressure System. I conclude that seasonal differences in atmospheric circulation are a probable driver of isotope variability at Eclipse, with high isotope ratio cold seasons characterized by a more zonal moisture flow regime and local moisture sources. This finding suggests that high-isotope ratio cold seasons in the Eclipse Icefield record may provide a useful proxy of past variability in the Pacific-North America pattern and Aleutian Low Pressure System.

ACKNOWLEDGEMENTS

TABLE OF CONTENTS

LIST OF TABLES

LIST OF FIGURES

CHAPTER 1

CLIMATE RECONSTRUCTION IN THE NORTH PACIFIC

1.1. Background

Temperatures in the Arctic have increased rapidly in comparison with the rest of the world, making an understanding of natural system dynamics critical to climate change adaptation in populated Arctic areas. The North Pacific region lies under the influence of several interacting atmospheric and oceanic cycles of variability that cause changes in local meteorological and climatic conditions such as temperature, precipitation, and storminess over annual to decadal timescales. These changes impact humans and other species that populate the region. For example, dramatic population changes in salmon, an important source of food and income for local communities, have been linked to regime shifts of the Pacific Decadal Oscillation (PDO), an interdecadal cycle of sea surface temperature (SST) variability in the North Pacific (Mantua et al. 1997). PDO regime shifts are also associated with population changes in other marine organisms such as sea lions (Rodionov et al. 2005), phytoplankton (Venrick et al. 1987), and zooplankton (McFarlane and Beamish 1992), all of which are crucial to the well-being of regional ecosystems. The characteristics of the PDO are quantified by the PDO Index, where the positive phase is associated with warmer SSTs in the Gulf of Alaska (GOA) and surrounding ocean (Mantua et al. 1997).

The PDO cycle is linked with atmospheric variability, with warmer SSTs in the positive phase associated with the enhanced transport of warm, moist air masses into the GOA region due to enhanced cyclonic (counterclockwise) circulation (Mantua et al. 1997). This counterclockwise circulation pattern is known as the Aleutian Low Pressure Center (ALow). The ALow is a predominantly wintertime phenomenon located in the vicinity of the Aleutian Islands, first described by Trenberth and Hurrell (1994). In 1976 the PDO underwent a phase shift from negative to positive phase, and the PDO index maintained predominantly positive values for the period 1977 – 2001 (Hartmann and Wendler 2005).

1

This led the ALow to strengthen in magnitude, which manifests as warmer, wetter conditions in southern Alaska and western Canada. Since the 1970s, winter temperatures in Alaska have warmed by as much as 3 °C (Hartmann and Wendler 2005). Proxy and instrumental records indicate that variability in the ALow is partially linked to tropical conditions, connected to the North Pacific through the Pacific-North America (PNA) atmospheric teleconnection pattern (Figure 1.1; Wallace and Gutzler 1981, Trenberth and Hurrell 1994, Fisher et al. 2008, Osterberg et al. 2014, Winski et al. 2017). The PNA pattern is expressed as variability in mid-troposphere geopotential heights, in which the positive phase is associated with deeper geopotential heights (a "trough") over the North Pacific and Gulf of Alaska region, paired with higher geopotential heights (a "ridge") over western North America and Alaska (Wallace and Gutzler 1981).
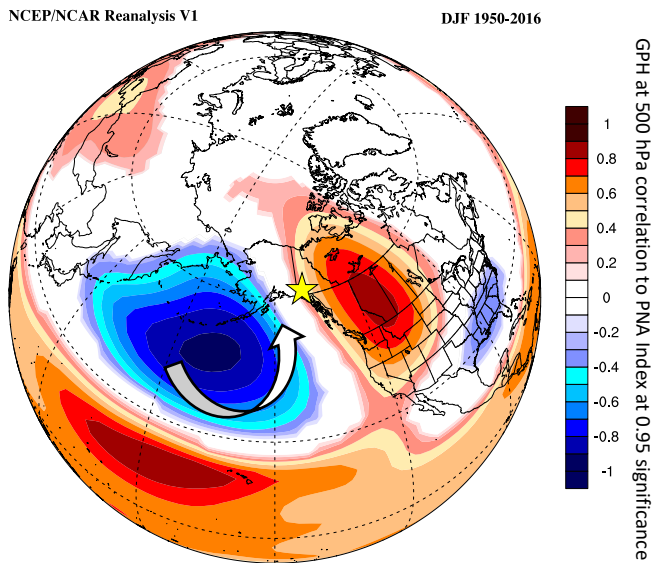
Figure 1.1 Pacific-North America Pattern (PNA). NCEP/NCAR Reanalysis map showing correlation between 500 hPa geopotential height (GPH) and the PNA Index in winter (DJF, 1950 – 2016). Warm colors indicate positive correlations, cool colors indicate negative correlations. White arrow indicates cyclonic circulation that drives enhanced southerly moisture transport into the Gulf of Alaska. Approximate location of study site is marked by yellow star. Image produced using Climate Reanalyzer, Climate Change Institute, University of Maine , USA

North Pacific alpine glaciers present an opportunity to quantify regional climate dynamics using glaciochemical signals in ice cores. Mt. Logan (60.57 °N, 140.41 °W) is located in the St. Elias Mountains of Yukon, Canada (Figure 1.2). At 5,340 m elevation and 500 hPa tropospheric height, the placement of its summit plateau at the end of the North Pacific storm track (Blackmon 1976) allows its ice to record extratropical responses to the El Niño Southern Oscillation (ENSO) cycle (Moore et al. 2001). Using an ice

core from Mt. Logan, Osterberg et al. (2014) showed that the ALow is sensitive to ENSO-related

variability in the tropical Pacific. Winski et al. (2017) found a similar result using annual accumulation

recorded in an ice core from Mt. Hunter in nearby Denali National Park, Alaska. The Mt. Hunter record

showed that warming temperatures in the western tropical Pacific and Indian Oceans are associated

with a near-doubling of precipitation in Alaska since 1850 through the strengthening influence of the

ALow.
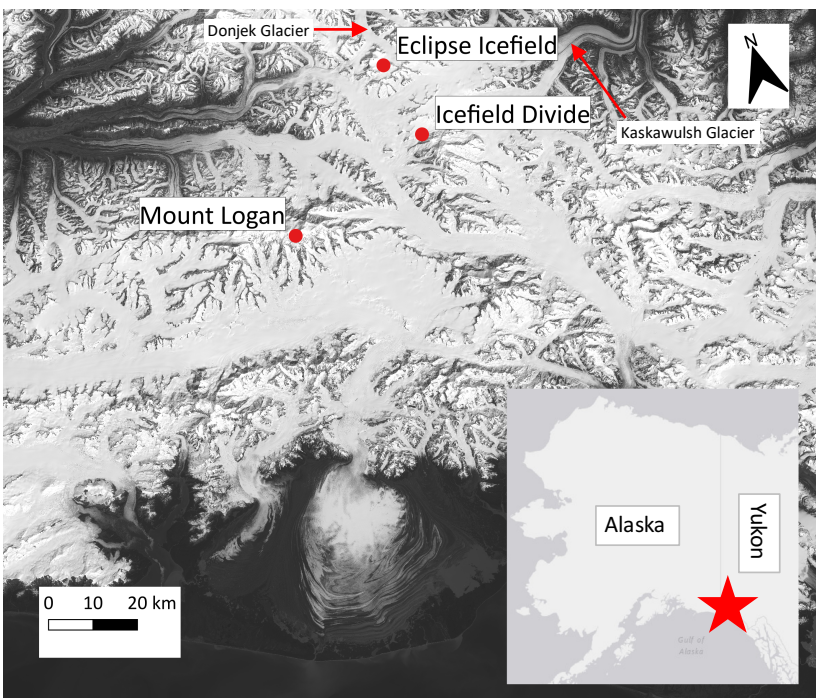
Figure 1.2 Map of St. Elias Field Area. Map shows Eclipse Icefield and Icefield Divide (the two sites of interest in this study) as well as Mt. Logan, from which many previous studies have retrieved and analyzed ice cores (Zdanowicz et al. 2014). Image from Landsat-8 (USGS), acquired June 9, 2016.

Normally, paleoclimate reconstruction based on stable isotopes in ice cores relies on the

established linear relationship in polar regions between stable isotope fractionation in ice and the air

temperature at the time when the ice was initially deposited as snow (Dansgaard 1964). Isotope

fractionation involves the separation of heavy isotopes (in the water molecule, ^{18}O and ^{2}H) from light

isotopes (^{16}O and ^{1}H). It is a temperature-dependent thermodynamic process, leading to generally

higher isotope ratios during warm climate regimes and lower isotope ratios during cooler climate

regimes. This relationship is especially well-behaved in sites located inland on the large ice sheets of

Greenland and Antarctica. However, the isotope-temperature relationship is static in neither time nor space due to differences in local topography, atmospheric characteristics, and climate regimes. In order to reliably reconstruct paleotemperatures via isotopic analysis, the proxy isotope record must be calibrated with instrumental observations, such as air and surface temperature records (Jouzel et al. 1997). It is also important to determine the relative contributions of other mechanisms, such as precipitation amounts, the seasonal distribution of precipitation, and atmospheric circulation patterns, as the isotope signal in a particular location can be influenced by factors other than temperature.

In the North Pacific, Holdsworth et al. (1992) found that the stable isotope signal in Mt. Logan ice cores is poorly correlated with regional air temperature records. This is due to the large elevation difference between ice core sites on Mt. Logan's summit plateau and weather stations near the Pacific coast in Canada and Alaska, which usually receive moisture from different air masses of distinct isotopic signatures. This causes a step-like separation in isotope fractionation sequences between sites of 1,750 – 3,350 m elevation and those above 5,300 m (Holdsworth et al. 1991). Rupper et al. (2004) found similarly poor relationships between snow accumulation measured in the Mt. Logan ice core record and accumulation recorded by regional weather stations and reanalysis products.

Eclipse Icefield (60.84 °N, 139.84 °W; 3,017 m elevation) is located on the Donjek Glacier (Figure 1.2), 45 km northeast and 2 km lower in elevation than the Mt. Logan coring sites, with an accumulation rate almost five times greater (Wake et al. 2002). Throughout this thesis, I refer to Eclipse Icefield as "Eclipse". Owing to the Eclipse ice core site's high accumulation rate, low amount of melt, and low elevation in comparison to Mt. Logan, ice cores from Eclipse provide a strong potential for reconstructing regional hydroclimate variability (Wake et al. 2002, Yalcin et al. 2007, Kelsey et al. 2012, Zdanowicz et al. 2014). However, Eclipse is still much higher in elevation than most regional weather stations. While past work has revealed correlations between air temperature and precipitation recorded by Canadian and Alaskan weather stations and stable isotope fractionation and accumulation in the

Eclipse ice core record, these correlations were only significant in years with extreme fractionation and/or accumulation in the ice core (Kelsey et al. 2012).

A lack of reliable instrumental data at or near ice core sites in the St. Elias, due to harsh meteorological conditions that prevent access and maintenance of the instrumentation, has presented a barrier to accurate, site-specific interpretations of the ice core record. An automated weather station (AWS) is located at Icefield Divide (60.68 °N, 139.78 °W; 2,603 m elevation), approximately 30 km from Eclipse in the accumulation zone of the Kaskawulsh Glacier (Figure 1.2). I will be referring to Icefield Divide as "Divide" hereafter. The combination of datasets from the Divide AWS and Eclipse ice cores provides an opportunity to interpret and calibrate isotope records in the North Pacific, which was not possible in work completed prior to the installation of the station and may lead to more accurate reconstructions of regional paleoclimate dynamics.

1.2. Goals

Broadly, I aim to advance ice core-based paleoclimate reconstruction efforts in the St. Elias by identifying relationships between ice core records and instrumental data. Each of the following chapters has been written with the intent of publication, and each has its own set of goals and objectives. Chapter 2, "Climate Threshold for Isotope Signal Preservation in the St. Elias Mountains," is guided by the goal of quantifying a climate threshold over which the isotope signal suffers melt-related alteration. I examine mean annual temperature, accumulation rate, and melt percentage, in comparison with isotope signal preservation, at Eclipse and Divide as well as other Arctic coring sites with published results. In Chapter 3, "Investigation of Climatic Significance and Seasonality in Stable Isotope Records from Eclipse Icefield, St. Elias Mountains, Yukon, Canada" I compare the well-preserved isotope record from Eclipse with climate reanalysis products, climate indices, and data from the Divide AWS to determine the relationship between the ice core record and large-scale hydroclimate dynamics. The

identification of such relationships provides a context for the paleoclimatic interpretation of Eclipse ice

core stable isotope records in future work.

CHAPTER 2

CLIMATE THRESHOLD FOR ISOTOPE SIGNAL PRESERVATION IN THE ST. ELIAS MOUNTAINS

2.1. Background and Motivation

Surface melt in glacier systems affects the use of ice core stable isotopes for paleoclimate

reconstruction, as meltwater percolation through the snowpack alters the original isotope signal (Moran

and Marshall 2009). The amount and type of alteration that shallow layers of snow and firn experience

post-deposition depends on factors specific to each coring site, e.g. temperature, accumulation rate,

percentage of annual accumulation that melts during the warm season, and amount of meltwater that

accumulates in the system (e.g. Campbell et al. 2012). Early in the warm season, signal alteration tends

to be dominated by the downward percolation of meltwater, which results in the reduction of isotope

signal amplitude in firn layers (Taylor et al. 2001, Pohjola et al. 2002, Moran et al. 2011, Winski et al.

2012). Here and throughout this chapter, reduction in isotope signal amplitude refers to the decrease in

isotopic range with increasing core depth, resulting in a "flat-lined" isotope signal measured in firn and

ice layers. Later in the melt season, when the system contains more meltwater, isotopic enrichment can

occur due to ongoing fractionation between meltwater and water vapor in the surrounding air (Moran

and Marshall 2009, Moran et al. 2011, Winski et al. 2012). This enrichment occurs when meltwater

evaporates because the process of evaporation favors lighter isotopes.

   Meltwater-induced isotope signal alteration in ice core sites results directly from melt, which

occurs when the air temperature exceeds the freezing point (Ohmura 2001). The amount of time each

year during which a site experiences above-freezing temperatures is quantified using positive degree

days (PDD). Coring sites are often located at high latitude or elevation to minimize the consequences of

PDD, such as Lomonosovfonna Icefield in Svalbard (78.87°N, 17.43°E; Divine et al. 2011, Pohjola et al.

2002), Penny Ice Cap on Baffin Island (67.25°N, 65.75°W; Fisher et al. 2003), and Mt. Hunter in Denali

National Park (3,900 m above sea level [ASL]; Winski et al. 2017, 2018) (Figure 2.1). Temperatures at

these sites rarely rise above freezing at any point during the year, so melt is minimal such that the

isotope signal remains intact (Fisher et al. 1995, Moran et al. 2011, Grumet et al. 1998). The isotope

records contained in ice cores from lower latitude or elevation sites tend to be more impacted by melt,

such as a core drilled on Høghetta Ice Dome in northern Spitsbergen, Svalbard (79.28°N, 16.83°E, 1,200

m ASL). The Høghetta core was composed entirely of ice that had melted and refrozen, preventing

precise paleoclimate interpretation based on the stable oxygen isotope record (Fujii et al. 1990, Koerner

1997). The mean summer (June – August, JJA) temperature at Høghetta is slightly above freezing (0.9

°C), indicating that the site experiences many PDDs during the summer.
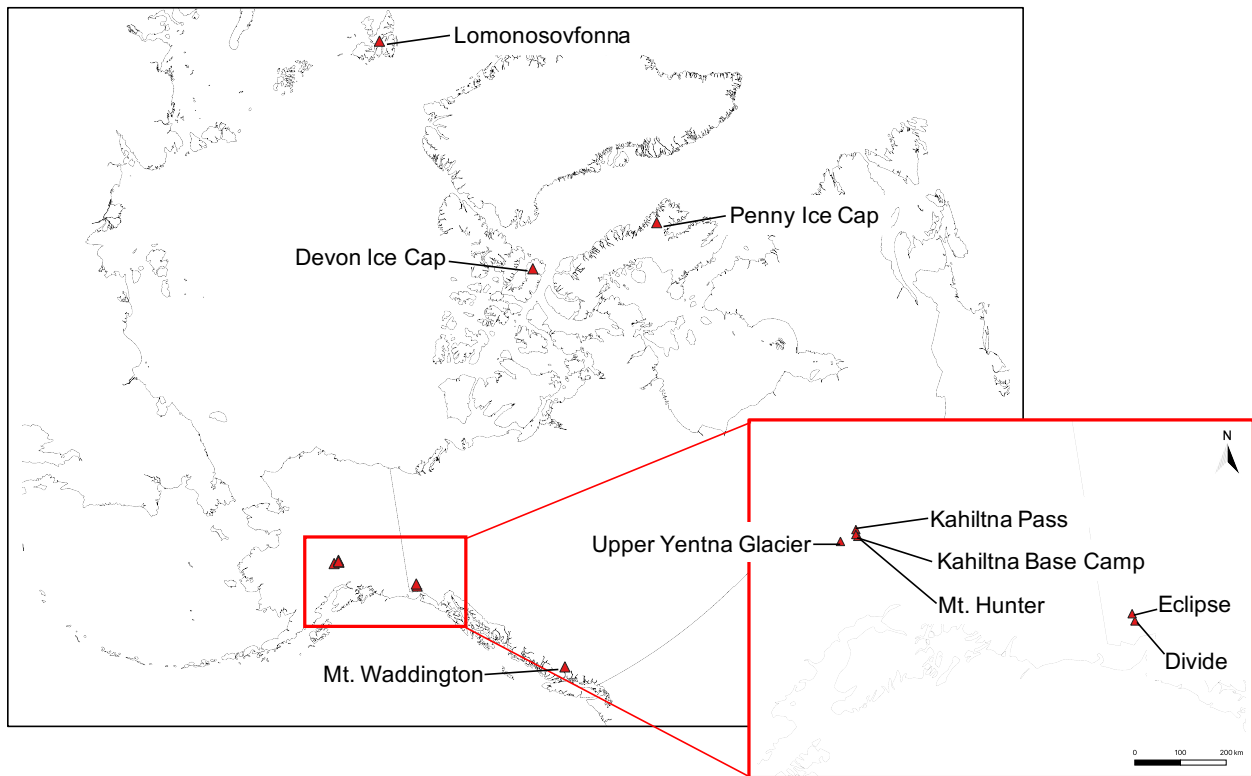
Figure 2.1 Selected Arctic Ice Core Sites. The locations of Eclipse, Divide, and eight other Arctic ice core
sites are marked with red triangles. Inset map shows six ice core sites in the North Pacific region.

Annual accumulation rate also plays a role in signal preservation, making the relationship

between temperature, melt percentage, and signal alteration less clear. In order to significantly alter the

isotope signal, summer melt must penetrate through the entire annual snowpack. Using an ice core

from Combatant Col, Mt. Waddington, Canada, Neff et al. (2012) found a well-preserved seasonal

isotope signal despite a relatively high mean annual temperature of -5 °C and an above-freezing mean summer temperature. Because this core site receives an average accumulation rate of 6.8 m water-equivalent (w.e.) snowfall per year, meltwater is unable to percolate throughout the annual snowpack, so isotope signal amplitude is preserved (Neff et al. 2012). Høghetta Ice Dome (Svalbard), while experiencing summers approximately 2 °C cooler than summers at Mt. Waddington, receives an accumulation rate of only 0.2 m w.e. yr^{-1}, resulting in complete percolation of the annual layer by meltwater (Koerner 1997).

Temporal variations in isotope signal alteration from melt exist as well, particularly in sites with ice core records extending through the Holocene Thermal Maximum (HTM) 8,000 years before present (BP). The high latitude of Agassiz Ice Cap (80.7 °N, 73.1 °W) results in a cold mean annual temperature of -22.4 °C. The ice core proxy record from Agassiz Ice Cap shows temperatures at the coring site during the HTM to have been 2 °C warmer than they were in 1984, when Fisher et al. (1995) retrieved a core from the top of the ice cap. While the authors found the section of the core from surface (1984) to ~7,500 years BP to contain a well-preserved oxygen isotope record, the record contained discontinuities and noise during the depth interval between 7,500 years BP and c. 10,000 years BP, coincident with melt percentages of up to 100%. The authors attribute these observations to high summer melt and net ablation early in the Holocene, consistent with the timing of the HTM (Fisher et al. 1995). A guiding goal of this project is to examine how the HTM may be expressed in ice cores from the St. Elias Mountains in terms of melt-related isotope signal degradation, which will inform future drilling efforts in a region where complete Holocene ice core records are sparse.

Here, I compare instrumental and ice core proxy records from the Upper Kaskawulsh-Donjek (UKD) region (Eclipse Icefield [60.84 °N, 139.84 °W, 3,017 m ASL, hereafter referred to as "Eclipse"] and Icefield Divide [60.68 °N, 139.78 °W, 2,603 m ASL, hereafter referred to as "Divide"] in the St. Elias Mountains, Yukon, Canada) as well as published results from other Arctic ice core sites, to address three

questions: *(1)* How well-preserved are isotope signals at Eclipse and Divide, in comparison to each other and to other Arctic ice cores? *(2)* Given an existing automated weather station (AWS) record of air temperature and snow accumulation at Divide, what are the meteorological thresholds for isotope signal alteration in the St. Elias Mountains? *(3)* What meteorological thresholds for signal preservation exist in other Arctic ice coring sites? To investigate these questions at Eclipse and Divide, I used *in situ* records of temperature collected by the AWS and an iButton temperature sensor, snow accumulation using the AWS and ice cores, isotopes and melt using ice and firn cores, and subsurface stratigraphy using ground-penetrating radar (GPR). I also use remotely-sensed land surface temperature (LST) data from the National Aeronautics and Space Administration (NASA)'s Moderate Resolution Imaging Spectroradiometer (MODIS) dataset. The short (~30 km) distance between the Divide AWS and ice core site and the Eclipse ice core site, as well as the 16-year temporal overlap between the Divide AWS dataset and Eclipse ice core record, give a unique opportunity to investigate thresholds for isotope signal preservation in neighboring locations, as studies in the past have been limited by short proxy-instrument timescale overlaps (Wake et al. 2002, Kelsey et al. 2012). The results improve our understanding of ice core-based paleoclimate reconstruction in areas that have been or will be affected by melt. Results also have implications for the accuracy of remotely-sensed temperature products in regions with spatially variable snow types.

2.2. Methods

2.2.1. Ground-Penetrating Radar

GPR methods are based upon those used in nearby Denali National Park by Campbell et al. (2012) to examine the subsurface stratigraphy of several potential ice coring sites. Our group collected high-resolution GPR profiles of the upper ~20 – 30 m of firn at Eclipse (in 2016) and Divide (in 2018) using a Geophysical Survey Systems Inc. (GSSI) SIR-3000 control unit coupled with a model 5103 400MHz bistatic antenna unit. The antenna was towed by hand at an approximate speed of 0.3 – 0.5 m s^{-1} and

polarized orthogonally to the profile direction. Two-way travel time (TWTT) was 250 – 300 ns for the profile traces, with 2,048 samples per scan and 24 scans per second. The GPR profiles were recorded using range gain to compensate for attenuation. I also collected low-resolution GPR profiles using Blue System Integration's IceRadar system (Mingo and Flowers 2010) with 5MHz and 10Mz antenna units at Divide (in 2018) and Eclipse (in 2016), respectively.

2.2.2. Ice Coring

This study utilizes firn cores drilled at Eclipse in 2016 and 2017 and at Divide in 2018, as well as an ice core drilled at Eclipse in 2002 (Kelsey et al. 2012, Yalcin et al. 2006). At Divide, I dug a 2.20 m snow pit and sampled from it at 5 cm vertical increments, removing several centimeters of snow from the surface of the walls with a clean scraper to prevent contamination. I weighed each sample to create a snowpack density profile. From the bottom of this pit I drilled a 17.93 m firn core, with the pit and core length totaling 20.13 m. I processed the core in the field by cutting it into ~10 cm increments, noting the depths and lengths of all refrozen melt layers, and weighed each sample for density calculations. The thickness of annual layers (~3 m yr^{-1}) in the upper firn column allows for approximately 30 samples per year at this sampling resolution. After allowing the core and snow pit samples to melt in Whirl-Pak bags, I decanted equal portions of meltwater from each sample into separate vials, which were transported back to the stable isotope laboratory at the University of Maine in Orono, ME, USA. Here, the samples were analyzed for stable hydrogen and oxygen isotope ratios (D/H and $^{18}O/^{16}O$, respectively) using a Picarro L-2130-i laser cavity ring-down spectrometer linked to a high throughput vaporizer with 0.1 ‰ precision for δD and δ^{18}O. Isotope values are reported in standard δ notation:

$$\delta^{18}O \text{ or } \delta D = (\frac{R_{sample}}{R_{standard}} - 1) * 1000,$$

with R$_{standard}$ referencing the Vienna-Standard Mean Ocean Water (V-SMOW) accepted standard. In this equation, R is equal to the ratio of heavy to light isotopes in the sample or standard.

The firn cores retrieved from Eclipse in 2017 and 2016 were drilled to depths of 18.60 m and 58.96 m, respectively, and analyzed for isotopes and ions according to the above procedure. The 2002 Eclipse core was drilled to a depth of 315.12 m, processed, and analyzed by Kelsey et al. (2012). To derive a depth-age scale for the Eclipse cores, I used cyclic glaciochemical signals to delineate annual layers within the cores. Seasonal oscillations in stable oxygen and hydrogen isotopes ($\delta^{18}O$ and δD), deuterium excess (d-excess = $\delta D - 8\delta^{18}O$), and certain ions (Na^+, Mg^{2+}, and Ca^{2+}) have been utilized frequently in North Pacific ice core studies to construct depth-age scales (Yalcin and Wake 2001, Wake et al. 2002, Yasunari et al. 2007, Osterberg et al. 2014, Winski et al. 2017). To formulate the core chronology, four researchers (E. McConnell, K. Kreutz, D. Winski, W. Kochtitzky) independently picked the approximate position of January 1st for each annual layer using $\delta^{18}O$, δD, and d-excess for the 2017 and 2016 cores, and δD, Na^+, Mg^{2+}, and Ca^{2+} for the 2002 core. These picks were then reconciled to finalize the timescale. The temporal range of the 2002 core allows for verification of the timescale using sulfate peaks from regional volcanic eruptions throughout the 1900s (categorized by Yalcin et al. 2007), and the well-documented 1963 peak in cesium (Cs-137) resulting from nuclear weapons testing (Wake et al. 2002, Yalcin et al. 2007). The 2016 core timescale does not overlap with these documented events. However, it overlaps with the 2002 core, providing an opportunity to verify its timescale using the volcanic and cesium reference horizons when both cores are combined into a composite record. Our group dated the 2016 and 2017 Eclipse cores, and re-dated the 2002 core, to bottom ages of 2011, 1985, and 1397, respectively. Our 2002 core chronology deviates from the depth-age scale formulated by Yalcin et al. (2006) by <2%.

Annual accumulation recorded in the 2016 and 2017 Eclipse cores is equal to the water equivalent thickness of each annual layer. Flow modelling to account for layer thinning was not applied to annual accumulation calculations because the bottom core depth is relatively shallow in comparison to the total ice thickness. Annual layer thicknesses were converted to m w.e. using the firn density,

which ranges from 0.43 g cm^{-3} at the surface to 0.91 g cm^{-3} at the base of the 2016 core. From the 2016

Eclipse core, I estimate the annual accumulation rate at Eclipse to be about 1.4 (± 0.3) m w.e. yr^{-1}.

I formulated a depth-age scale for the Divide 2018 core using d-excess, which peaks in the

winter, as it showed a more amplified seasonal signal than either oxygen or hydrogen isotopes alone. I

dated the core to a bottom age of approximately 2010, with significant uncertainty due to the effects of

meltwater percolation on the isotope signal (discussed in detail below).

Using noted melt layer stratigraphy from Eclipse and Divide cores, I calculate melt percentage

(MP) as $\frac{melted\ annual\ accumulation}{total\ annual\ accumulation}$ x 100. Melted accumulation is calculated by measuring the cumulative

length of all refrozen melt layers contained within an ice or firn core.

2.2.3. *In Situ* Meteorological Records

The Divide AWS, maintained by the University of Ottawa, is located at Icefield Discovery Camp (60.68 °N,

139.78 °W; 2,603 m elevation) and is placed atop a nunatak to avoid burial. The station's temperature

record spans 2002 – present, composed of readings from a Campbell 107 temperature probe (± 0.2 °C),

in place on the station from 2002 – 2015, and a HOBO S-THB-M008 12-bit temperature sensor (± 0.21

°C) in place from 2009 – present. Both sensors record hourly air temperature measurements (Zdanowicz

et al., in prep.; Williamson et al., in review).

At Eclipse, a Maxim Integrated iButton Data Logger DS1922L (uncertainty = ± 0.5 °C) recorded air

temperatures at 3-hour intervals from May 21, 2016 through May 17, 2017 on a bedrock outcrop ~3 km

from the ice core drill site. The iButton was located inside of a plastic container and shielded by several

rocks to protect the device and aid retrieval.

For each dataset, I compared daily and monthly (30-day) mean temperatures and variance, as

well as monthly and seasonal correlation coefficients (r), with "spring" = March – May, "summer" = June

– August , "fall" = September – November, and "winter" = December – February.

The Divide snow accumulation record is composed of twice-daily readings from a Campbell

Scientific SR50 snow depth sounder instrument, which was operational at Icefield Discovery Camp from

2003 – 2012. The instrument measures accumulation and ablation based on the distance from the

instrument to the snow surface (Zdanowicz et al., in prep.; Williamson et al., in review). Instrumental

accuracy is the greater of ±1 cm or 0.4 % of the distance to the snow surface. Tilt of the station's mast

and/or burial of the station by snowfall occasionally impacts the accuracy of snow depth readings. To

correct for this, I manually checked snow depth records for blank values and sudden, unnatural

accumulation or ablation and removed these from the dataset. Annual accumulation is equal to the

difference between the snow depth at the date of year's end and at the date of minimum depth, with

depth reset to zero at the beginning of each year. If the station record lacked reliable data coverage

between the date of minimum snow depth and the date of year's end for any year, that year was

removed from the analysis. In total, five years were removed (2007, 2009, 2010, 2011, and 2012), and

five years were kept (2003, 2004, 2005, 2006, and 2008). Annual accumulation values were then scaled

according to the average density of the top 5 m of snow and firn (0.49 g cm^{-3}), which I calculated using

the firn core and snow pit samples retrieved from Divide in 2018. The density scaling procedure makes

the instrumental accumulation record comparable with ice core-derived accumulation values.

2.2.4. Remote Sensing of Land Surface Temperatures

I obtained remotely-sensed LSTs for both sites from NASA's MODIS/Terra Land Surface Temperature

data product (MOD11A1) at daily 1 km spatiotemporal resolution (downloaded from

https://earthdata.nasa.gov). The MODIS algorithm derives LSTs using a classification-based emissivity

method, assigning a land cover type to pixels based on land and snow cover inputs. Output values can

be downloaded in units of Kelvin (±2 K) with a scaling factor of 0.02 (Wan 2014). In clear sky conditions

over non-forested alpine areas, the fractional snow cover measured by MODIS has been shown to be

almost identical (90% overall accuracy) to *in situ* and higher spatial resolution satellite estimates (Pu et al. 2007).

My MODIS data collection spans the length of the Divide AWS dataset (2002 – 2017), excluding days in which the pixels covering Eclipse and Divide both lack data due to cloud cover. The MODIS LST data were processed using QGIS software. Pixel values were extracted from the 1 km pixel containing each site, converted to °C, and compared using annual and seasonal means as well as seasonal correlation coefficients. I also calculated differences and correlations between MODIS LST readings and air temperature readings from the Divide AWS and the Eclipse iButton. Figure 2.2 gives an example of the imagery and LST extraction procedure.

-24 °C   -15 °C
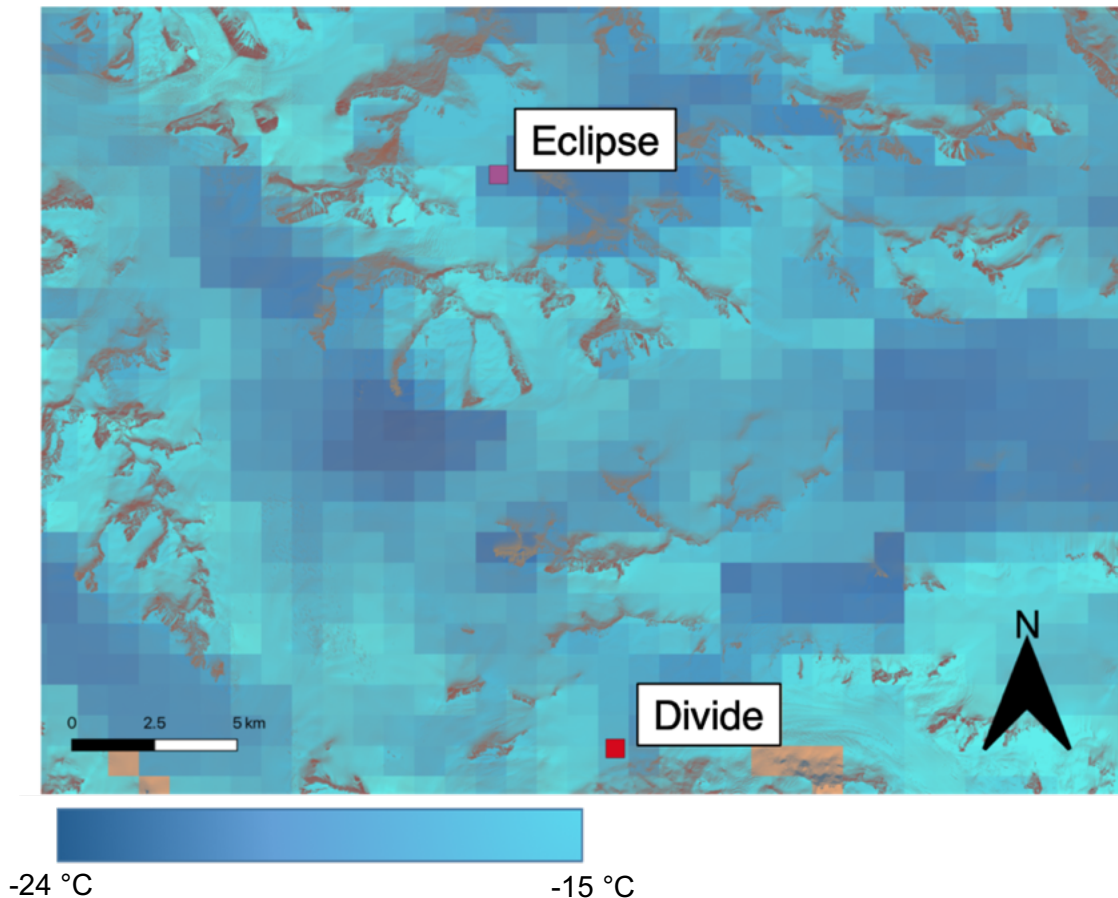
Figure 2.2 MODIS Land Surface Temperature Extraction. Example day (January 2, 2017) of MODIS imagery, overlaid on a Landsat-8 image of the region, used to compare land surface temperatures at Eclipse (purple square) and Divide (red square). Colder colors represent colder temperature values. Pixel resolution is 1 km^2.

2.2.5. Climate and Isotope Comparison of Arctic Ice Core Sites

I obtained mean summer temperatures, annual accumulation rates, mean melt percentages (where

available), and isotope signal amplitudes for eight Arctic ice core sites in addition to Divide and Eclipse

(Table 2.1). I use mean summer temperature as an analog for PDD, as these two variables are strongly

related ($r^2 = 0.92$, $p < 0.0001$) according to AWS air temperature observations at Divide (Figure 2.3). In

contrast, PDD values show a weak and statistically insignificant relationship with mean *annual*

temperature ($r^2 = 0.26$, $p = 0.07$).
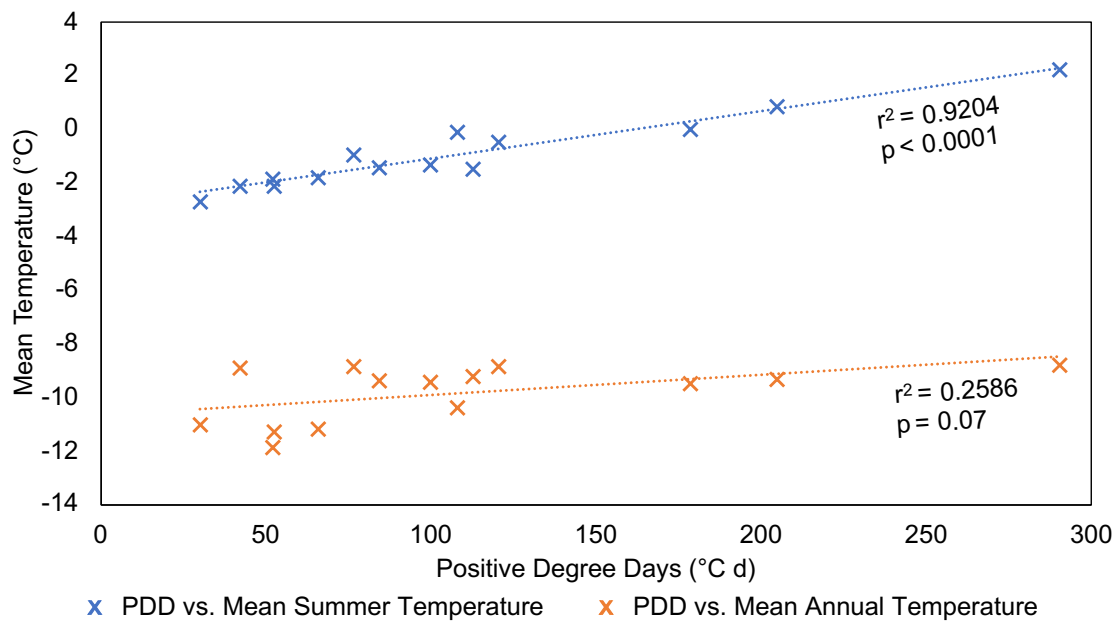
Figure 2.3 Positive Degree Day Scatter Plot. PDD vs. mean summer (JJA) temperature scatter plot and linear fit (top, blue), and PDD vs. mean annual temperature scatter plot and linear fit (bottom, orange), with r^2 values for each. Data points are constructed from Divide weather station hourly temperature readings from 2003 – 2016.

For mean summer temperatures at Penny Ice Cap (PIC) and Devon Ice Cap (DIC), I used the

University of East Anglia Climatic Research Unit (UEA CRU)'s Time-Series Version 4.1 of High Resolution

(0.5° latitude/longitude cell) Gridded Data of Month-by-Month Variation in Climate, an analysis product

with temperature data spanning 1901 – 2016 (Harris et al. 2014). I calculated 30-year climate averages

of summer temperatures for each site, with the 30-year timespan ending in the year during which the

ice core was drilled. To estimate the mean summer temperature at the Combatant Col ice core site on

Mt. Waddington, I calculated the mean summer temperature at Tiedemann Glacier using monthly mean air temperature data (1961-1990) from a weather station maintained by the University of Northern British Columbia. The station is located 1,205 m ASL and 4 km southeast of the Combatant Col ice core site. I adjusted the mean summer temperature to the elevation of the ice core site (3,000 m ASL) using an assumed wet adiabatic lapse rate of 7 °C km^{-1} for the region (P. Jackson, unpublished information). For four sites in Denali National Park, Alaska, USA, I calculated an average lapse rate of -4.6 °C km^{-1} based on mean summer temperatures reported for Mt. Hunter (Winski et al. 2018) and temperatures recorded hourly at Kahiltna Base Camp (KBC) by a University of Maine AWS installed in 2008. I used this lapse rate to estimate mean summer temperatures at the Upper Yentna Glacier (UYG) and Kahiltna Pass ice core sites. For Lomonosovfonna, I derived the mean summer temperature using data reported for Longyearbyen, Svalbard and a known lapse rate of 4.4 °C km^{-1} for the area (Pohjola et al. 2002).

Annual accumulation rates were reported in the literature for PIC (Grumet et al. 1998), UYG and Kahiltna Pass (Campbell et al. 2012), Mt. Hunter (Winski et al. 2018), Mt. Waddington (Neff et al., 2012), DIC (Mair et al. 2005), and Lomonosovfonna (Pohjola et al. 2002). For KBC, I used daily snow depth values recorded by the AWS from 2008 – 2013 to derive an annual accumulation rate.

Melt percentages were reported in the literature for PIC (Grumet et al. 1998), Kahiltna Pass (Campbell et al. 2012), and Lomonosovfonna (Pohjola et al. 2002). I calculated MP using melt-layer stratigraphy data for UYG (Kelsey et al. 2010), Mt. Hunter (Winski et al. 2018) and DIC (Fisher 1979). To quantify the effect of melt on isotope signal amplitude, I compared the oxygen or hydrogen isotopic range (in per mil, ‰) in the top quarter of a firn core drilled in each site with the isotopic range in the bottom quarter of the firn core. Firn core depths ranged from 9 – 25 m. This process allows for comparison of the isotope signal in surface snow versus in lower firn layers that have experienced meltwater percolation. Isotope amplitude reduction values from core top to core bottom are reported

as percentages and are based on isotope data from PIC (Fisher et al. 2003), UYG and Kahiltna Pass

(Kelsey et al. 2010), Mt. Hunter, Mt. Waddington (Neff et al. 2012), DIC (Fisher 1979), and KBC.

Table 2.1 Arctic Ice Core Site Information. Site name, region and location, elevation above sea level, mean summer (JJA) temperature, annual accumulation rate, melt percentage, and isotope amplitude reduction, which refers to the percentage of oxygen or hydrogen isotope signal amplitude reduction from the top quarter of a firn core to the bottom quarter of the core. Missing melt percentage values are from sites where the melt percentage and/or melt layer stratigraphy were not reported.

Ice Core Site	Region	Coordinates	Elevation (m)	Mean Summer Temp. (°C)	Accum. Rate (m w.e. yr^{-1})	Melt (%)	Isotope Amplitude Reduction (%)
Divide	NW Canada	60.68°N, 139.78°W	2,603	-1.0	1.6	4.8	81.25
Eclipse	NW Canada	60.84°N, 139.84°W	3,017	-1.8	1.4	8.5	2.13
Penny Ice Cap[1]	Canadian Arctic	67.25°N, 65.75°W	1,900	-3.4	0.4	50	23.51
Upper Yentna Glacier[2]	Alaska	62.81°N, 151.83°W	2,812	-1.2	1.8	3.4	37.30
Kahiltna Pass[2]	Alaska	63.07°N, 151.17°W	2,970	-2.0	0.8	9	51.32
Mt. Hunter[3]	Alaska	62.93°N, 151.08°W	3,912	-6.3	1.5	0.4	4.56
Mt. Waddington[4]	West Canada	51.39°N, 125.26°W	3,000	2.6	6.8	--	26.27
Devon Ice Cap[5]	Canadian Arctic	75.33°N, 82.50°W	1,800	-2.0	0.2	17.1	63.14
Kahiltna Base Camp[2]	Alaska	62.97°N, 151.17°W	2,194	1.6	1.3	--	92.23
Lomonosovfonna[6]	Svalbard	78.87°N, 17.43°E	1,255	-1.5	0.4	33	47.06

1. Fisher et al. 2003, Grumet et al. 1998; 2. Campbell et al. 2012, Kelsey et al. 2010; 3. Winski et al. 2018; 4. Neff et al. 2012; 5. Mair et al. 2005, Fisher 1979; 6. Divine et al. 2011, Pohjola et al. 2002

2.3. Results

2.3.1. Subsurface Stratigraphy

Deep (surface to bedrock) and shallow (surface to ~20 m depth) GPR imaging transects of the Eclipse

and Divide ice core sites show stratigraphic differences characteristic of more summer melt and a wetter

snowpack at Divide in comparison with Eclipse. In the deep (10 MHz) radar profile from Divide, the most

notable stratigraphic difference is a layer of heightened reflectance at ~25 m depth (Figure 2.4). The

feature resembles a strong GPR horizon at ~50 m depth in the UYG, which was interpreted as evidence

of a water table at the firn/ice transition zone due to meltwater percolation through the snowpack

(Campbell et al. 2012). Thus, I interpret the GPR horizon at Divide as an indication of a liquid water table

resting just below the bottom depth of the 2018 firn core. I do not see the same feature in the Eclipse

subsurface profile (Figure 2.4). Similarly, shallow (400 MHz) radar transects of the upper ~20 – 30 m of

firn at both sites show evidence of a wetter subsurface at Divide than at Eclipse, indicated by greater

radar signal attenuation within the firn at Divide (Figure 2.5).
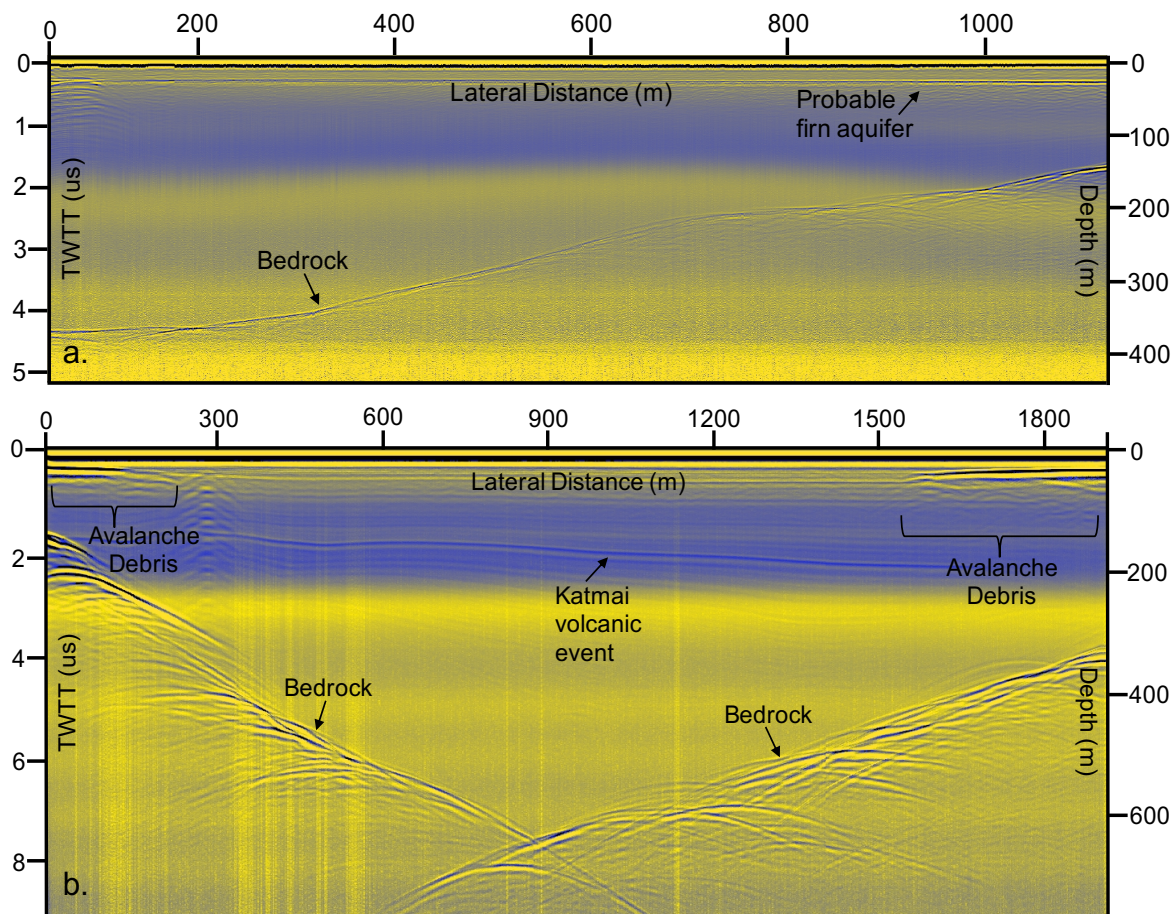
Figure 2.4 Deep Radar Profiles. Surface to bedrock stratigraphy profiles at Divide (10 MHz antenna, a) and Eclipse (5 MHz antenna, b) have prominent features noted, including bedrock depth, avalanche debris, a volcanic ash layer from the Katmai eruption, and a layer of high reflectance at ~25 m depth at Divide, which I infer to be a liquid water table. Two-way travel time of the GPR signal is marked on the left axis, lateral distance across-glacier on the upper axis, and depth within the ice on the right axis.
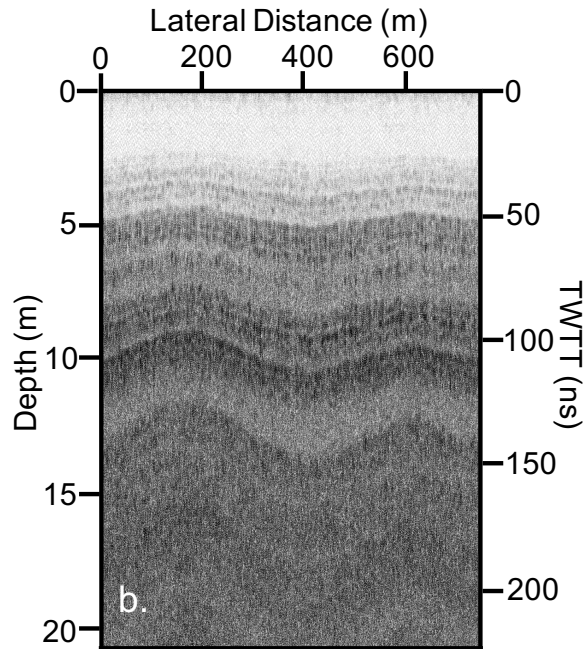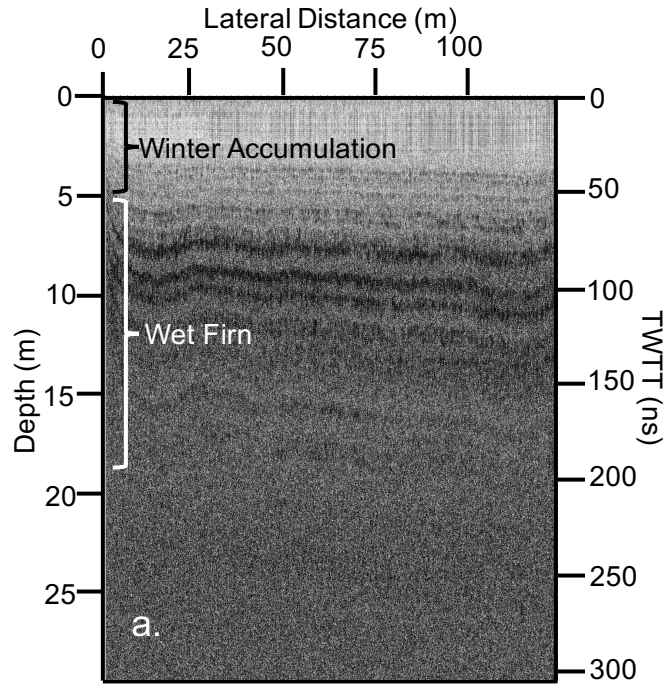
Figure 2.5 Shallow Radar Profiles. 400 MHz GPR profiles show greater signal attenuation at Divide (a) in comparison with Eclipse (b), indicating a wetter snowpack and more saturated firn at Divide. Depth within the ice is noted on the left axis, lateral distance across-glacier on the upper axis, and two-way travel time of the GPR signal on the right axis.

2.3.2. Meteorological Comparison: *In Situ* Temperature Data (2016 – 2017)

I found strong spatial coherence of daily mean air temperatures over the Eclipse – Divide distance during

the year of overlap between *in situ* datasets (2016 – 2017). Temperatures recorded by the Divide AWS

and Eclipse iButton show a correlated pattern of warm and cool periods (Figure 2.6). The amplitude of

warm and cool peaks is slightly dampened at Eclipse, which experienced a temperature range of 37 °C

(minimum -33 °C, maximum 4.1 °C) during 2016 – 2017 compared with Divide's range of 41 °C (minimum

-35 °C, maximum 5.6 °C). This may be due to differences in instrumentation (discussed below). Divide

was approximately 1 °C warmer than Eclipse, with an annual average of -11.3 °C at Eclipse and -10.3 °C

at Divide.

Figure 2.6 Air Temperature Records from Eclipse and Divide (May 2016 – May 2017). Divide temperatures are plotted in blue, Eclipse in orange. Plot shows daily mean air temperatures recorded by *in situ* instrumentation at Eclipse (iButton) and Divide (AWS).

Seasonally, I found the strongest air temperature correlations in 2016 – 2017 between mean daily temperatures at the Eclipse and Divide sites to occur during the spring ($r^2 = 0.96$), with slightly lower correlations in summer ($r^2=0.76$), fall ($r^2=0.74$), and winter ($r^2=0.74$) (Figure 2.7). These correlations are all significant ($p<0.0001$). Statistical results are summarized in Table 2.2.
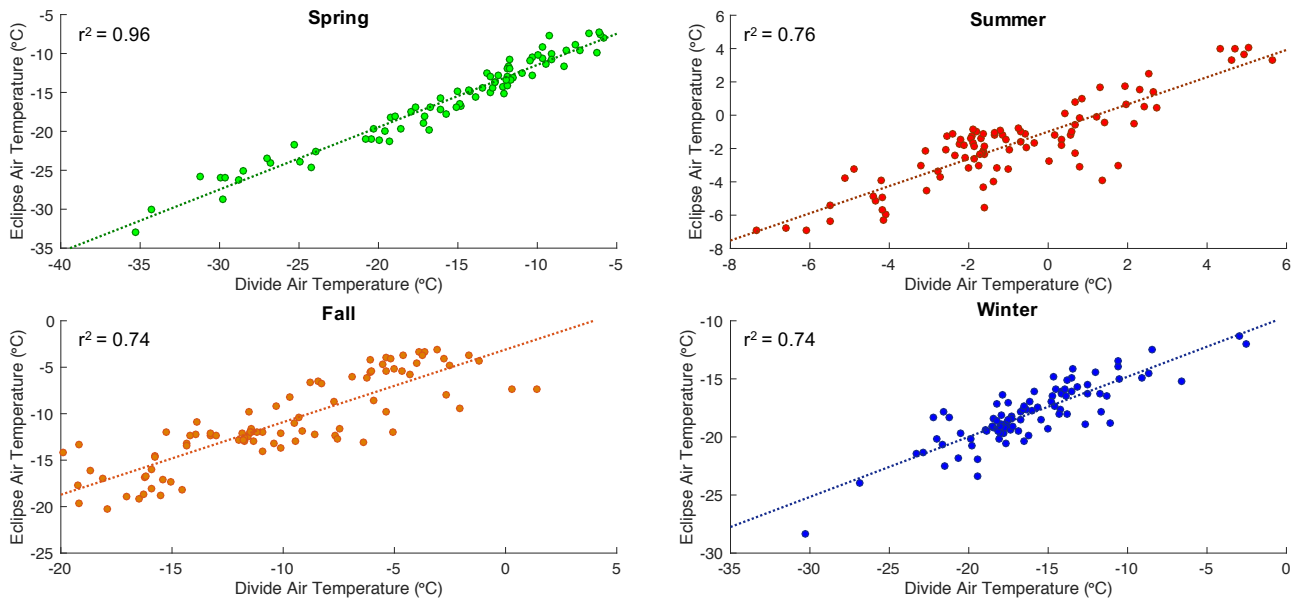
Figure 2.7 Seasonal Air Temperature Scatter Plots from *In Situ* Records. Plots of daily average air temperatures at Eclipse (y-axis) vs. Divide (x-axis) (2016 – 2017) in spring (green), summer (red), fall (orange), and winter (blue), with r-squared values listed. All correlations are significant at p<0.0001.

Table 2.2 Eclipse and Divide Air Temperature Statistics. Monthly means, differences in monthly mean (Eclipse – Divide), and variances of daily temperature (calculated per month) for air temperatures measured at each site by *in situ* instrumentation.

Timespan	Eclipse Mean (°C)	Divide Mean (°C)	Temperature Difference (°C)	Eclipse Variance	Divide Variance
5/21/16 – 6/19/16	-5.25	-3.84	-1.41	2.60	6.76
6/20/16 – 7/19/16	-0.15	0.58	-0.73	5.48	7.03
7/20/16 – 8/18/16	-1.02	-0.57	-0.45	1.75	2.83
8/19/16 – 9/17/16	-3.43	-3.21	-0.22	1.80	3.69
9/18/16 – 10/17/16	-9.36	-8.45	-0.91	7.35	24.16
10/18/16 – 11/16/16	-12.90	-11.89	-1.01	1.46	7.31
11/17/16 – 12/16/16	-18.52	-16.81	-1.71	2.50	6.85
12/17/16 – 1/15/17	-17.44	-14.99	-2.45	10.37	29.08
1/16/17 – 2/14/17	-17.86	-16.02	-1.84	4.72	11.20
2/15/17 – 3/16/17	-22.01	-23.03	1.02	20.92	42.97
3/17/17 – 4/15/17	-16.49	-15.24	-1.25	7.09	9.06
4/16/17 – 5/15/17	-11.51	-10.76	-0.75	6.99	9.97

2.3.3. Meteorological Comparison: MODIS LST Data (2002 – 2017)

2.3.3.1. Eclipse vs. Divide Land Surface Temperatures MODIS LSTs showed strong spatial temperature coherence between Eclipse and Divide over the 16-year timespan from 2002 – 2017, with correlation coefficients ranging from 0.96 – 0.98 (p<0.0001) (Figure 2.8). Eclipse was consistently colder than Divide

for each of the studied years. Differences in annual average temperature between the two sites ranged

from 1 – 3 °C (Table 2.3), with an average difference of -1.8 °C between Eclipse and Divide.
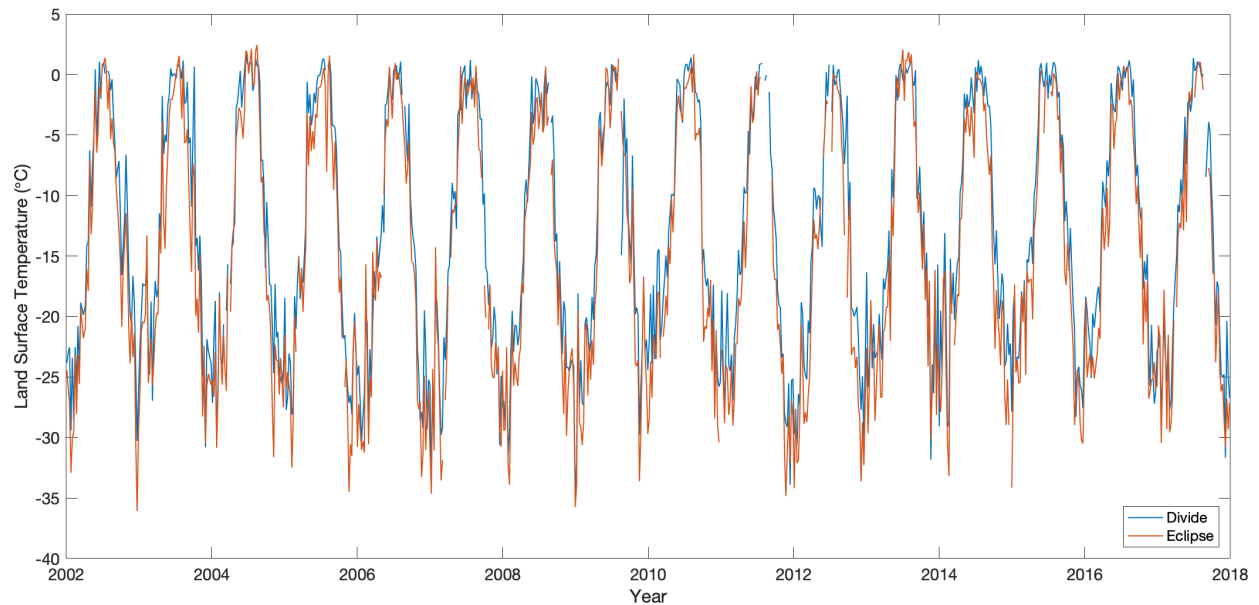
Figure 2.8 Weekly Land Surface Temperatures. Data recorded by MODIS instrumentation from 2002
– 2017 at Eclipse and Divide. Missing data results from cloud cover.

Broken into seasonal resolution, the strongest LST coherence between the two sites consistently

occurred during spring (Figure 2.9). Spring correlation coefficients for each year ranged from 0.95 to

0.99. The poorest seasonal correlations, as well as the largest spread in correlation coefficients over the

16-year timespan, were consistently found in the summer season. Summer correlation coefficients

ranged from 0.50 to 0.89. Fall and winter correlation coefficients ranged from 0.79 to 0.97 and from

0.67 to 0.92, respectively. These correlations are significant at $p<0.0001$, with the exception of the

summer correlations, which are significant at $p<0.02$.

Table 2.3 Eclipse and Divide Annual Land Surface Temperature Statistics. Annual mean land-surface temperatures, differences (Eclipse – Divide), maxima, and minima from NASA MODIS dataset.

Year	Eclipse Mean (°C)	Eclipse Max/Min (°C)	Divide Mean (°C)	Divide Max/Min(°C)	Temperature Difference (°C)
2017	-17.74	2.63/-39.59	-15.59	1.79/-44.61	-2.15
2016	-14.88	1.47/-32.01	-13.15	1.91/-32.79	-1.73
2015	-15.68	1.91/-41.35	-13.69	2.25/-37.85	-1.99
2014	-14.19	1.61/-34.65	-12.37	2.53/-31.45	-1.82
2013	-14.34	2.47/-37.65	-13.33	2.33/-33.49	-1.01
2012	-18.80	0.85/-37.85	-16.10	1.41/-38.13	-2.70
2011	-18.52	1.11/-39.31	-16.26	1.45/-41.77	-2.26
2010	-15.02	2.39/-37.77	-12.77	1.95/-31.45	-2.25
2009	-16.09	2.95/-38.93	-14.29	1.45/-39.93	-1.80
2008	-17.08	0.87/-37.87	-15.48	2.19/-36.39	-1.60
2007	-15.69	2.35/-37.11	-14.65	1.65/-36.49	-1.04
2006	-17.83	1.95/-42.13	-16.05	1.25/-38.53	-1.78
2005	-14.55	2.73/-37.27	-12.96	2.03/-40.55	-1.59
2004	-13.76	3.73/-35.99	-12.75	3.21/-33.25	-1.01
2003	-15.18	1.95/-35.17	-12.98	1.93/-31.63	-2.20
2002	-16.04	2.27/-39.19	-13.65	2.33/-35.89	-2.39
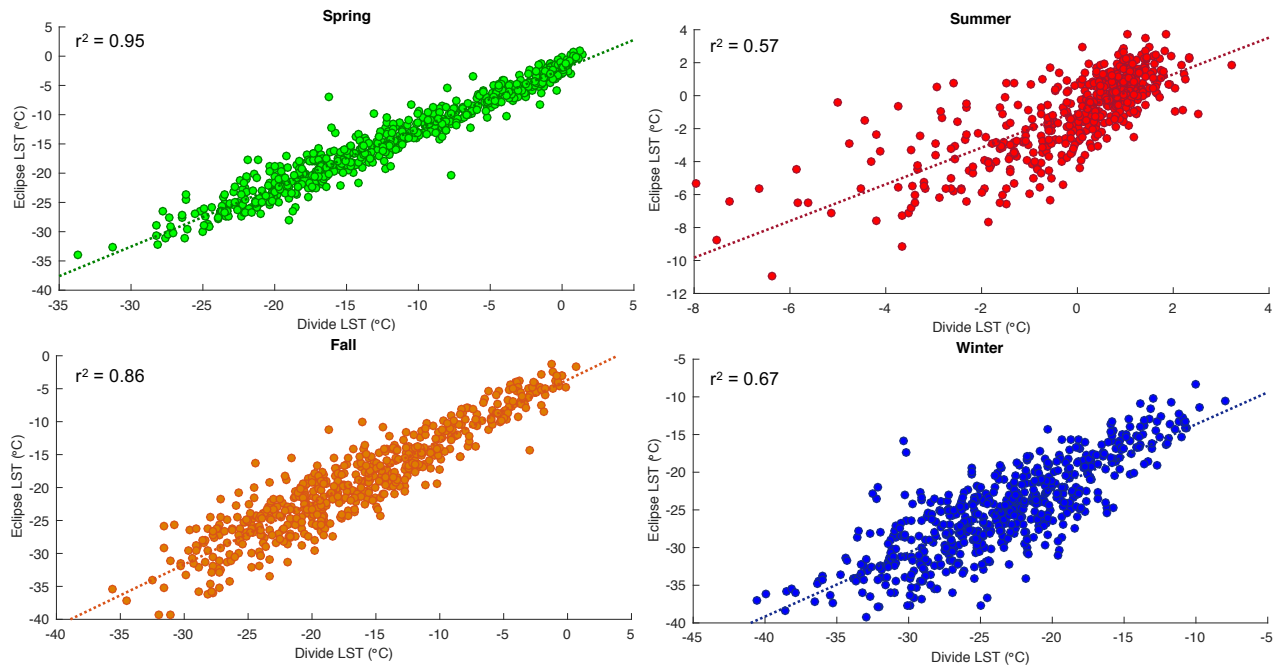
Figure 2.9 Seasonal Land Surface Temperature Scatter Plots. Plots use MODIS data. Plots of daily land surface temperatures (LST) at Eclipse (y-axis) vs. Divide (x-axis) (2002 – 2017) in spring (green), summer (red), fall (orange), and winter (blue), with r-squared values listed. All correlations besides summer are significant at p<0.0001. Summer correlation is significant at p<0.02.

2.3.3.2. *In Situ* vs. MODIS Land Surface Temperatures Comparing MODIS LST data with air temperature data from the Divide AWS, I found that the strength of correlations between these two data types are seasonally-dependent and that MODIS consistently reports cooler temperatures than those measured by *in situ* instrumentation. This MODIS cold bias is illustrated in Figure 2.10 and was previously observed in snow-covered areas within the Yukon, Canada region by Williamson et al. (2017). While MODIS-AWS correlations for 61 of the 62 seasons analyzed between 2002 – 2017 were significant at p<0.01 (with the exception of summer 2007), the correlations were strongest in spring (r^2=0.90 – 0.96), weaker in fall (r^2=0.70 – 0.95) and winter (r^2=0.45 – 0.79), and weakest in summer (r^2=0.34 – 0.76). The MODIS cold bias compared with the *in situ* record was practically non-existent in spring (average difference = -0.01 °C), generally weak in summer (-0.70 °C), stronger in fall (-4.68 °C), and most pronounced in winter (-7.50 °C) (Figure 2.11).

27
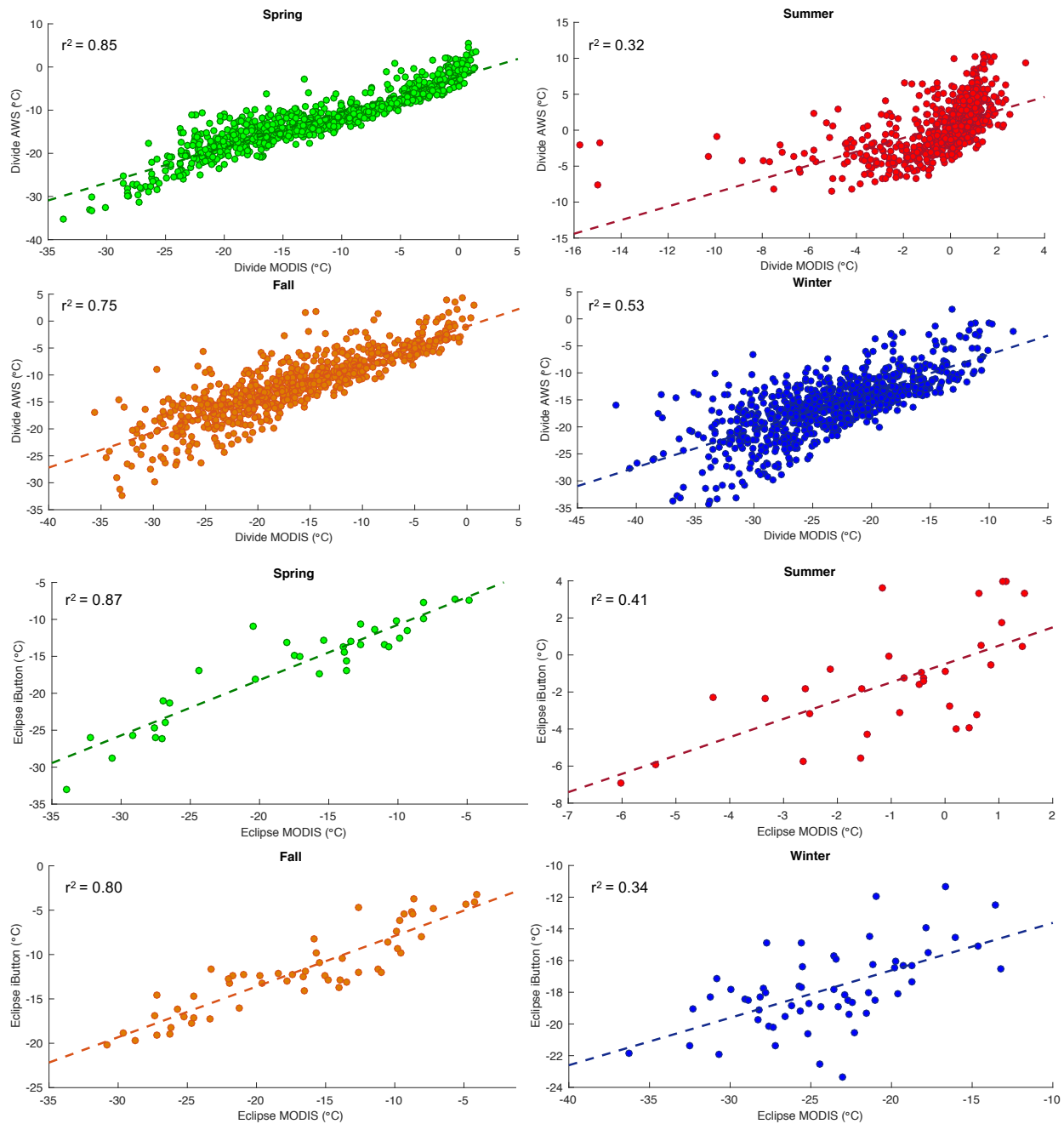
Figure 2.10 Seasonal MODIS vs. *In Situ* Temperature Scatter Plots. Plots of LST measured via MODIS (x-axis) vs. air temperature measured via AWS (y-axis) at Divide (2002 – 2017) in spring, summer, fall, and winter (top 2 rows), and LST via MODIS vs. air temperature via iButton at Eclipse (2016 – 2017) in spring, summer, fall, and winter (bottom 2 rows) with r-squared values listed.

In a comparison of the year of Eclipse iButton temperature data (2016 – 2017) with the same timeframe of MODIS LST data, spring showed the strongest MODIS-iButton correlation ($r^2=0.93$), followed by fall ($r^2=0.90$), summer ($r^2=0.64$), and winter ($r^2=0.59$), with $p<0.0004$ for all correlations

(Figure 2.10). At Eclipse, the cold bias was nonexistent in summer (average difference = 0.48 °C), slight in

spring (-1.22 °C) and fall (-5.13 °C), and winter showed the strongest MODIS cold bias (-6.22 °C) (Figure

2.11).
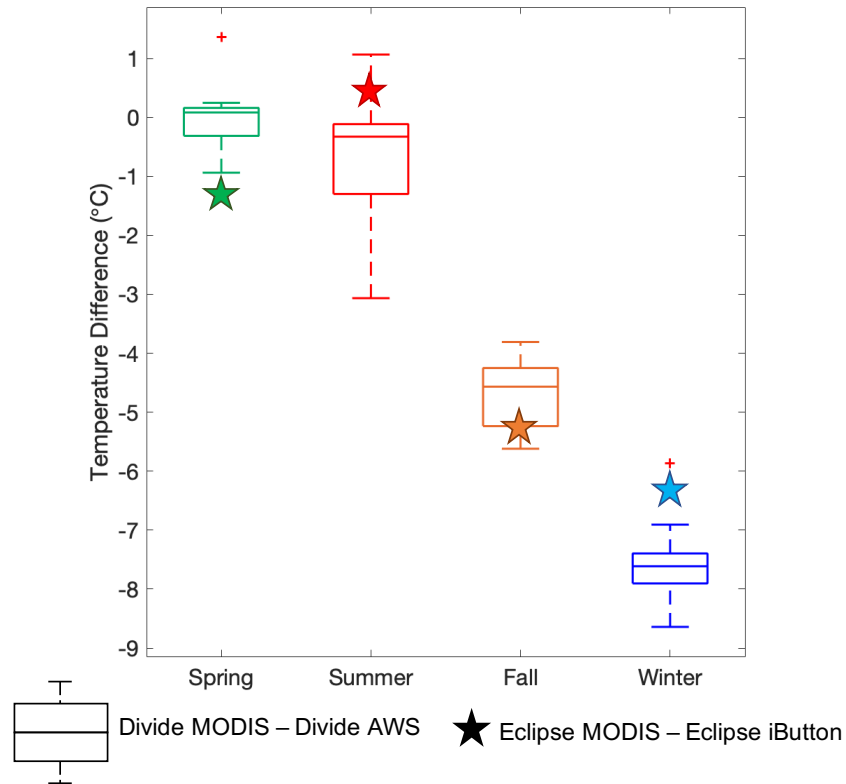
Figure 2.11 Seasonal MODIS vs. *In Situ* Temperature Differences. Average seasonal difference (difference = MODIS temperature – AWS or iButton temperature) for 2002 – 2017 at Divide (box plots) and 2016 – 2017 at Eclipse (stars). From left to right: spring, summer, fall, winter. Lines within boxes show the median, lines at edges of boxes indicate the 25th and 75th percentile range, whiskers show the range of values, and plus symbols represent outliers.

2.3.4. Snow Accumulation at Eclipse and Divide

2.3.4.1. Annual Accumulation Comparison Due to the timescale uncertainty introduced by isotope

signal amplitude reduction in the bottom ¾ of the Divide firn core, I used the AWS instead of the core to

calculate the accumulation rate. Of the 10 years during which Divide was equipped with a snow depth

sensor, five years (2003, 2004, 2005, 2006, and 2008) had complete data coverage from the end of the

melt season until the end of the year. The other years (2007, 2009, 2010, 2011, and 2012) were affected

by burial of the station by snow and/or tilt of the station's mast, so these years were excluded from

comparison with the Eclipse ice core accumulation record. Over the time period of snow depth data collection by the instrument, I estimate the accumulation rate at Divide to be 1.6 (± 0.2) m w.e. yr^{-1}. This value accounts for snow compaction that occurs between snowfall events.

In all five years with reliable datasets, water-equivalent accumulation totals calculated using the 2016 firn core at Eclipse and the AWS at Divide were within one standard deviation of one another (Figure 2.12). In four of the five years (2003 – 2006), I observed spatial coherence of the accumulation signal between Eclipse and Divide, i.e. when annual accumulation increases at Divide, it also increases at Eclipse, and vice versa.
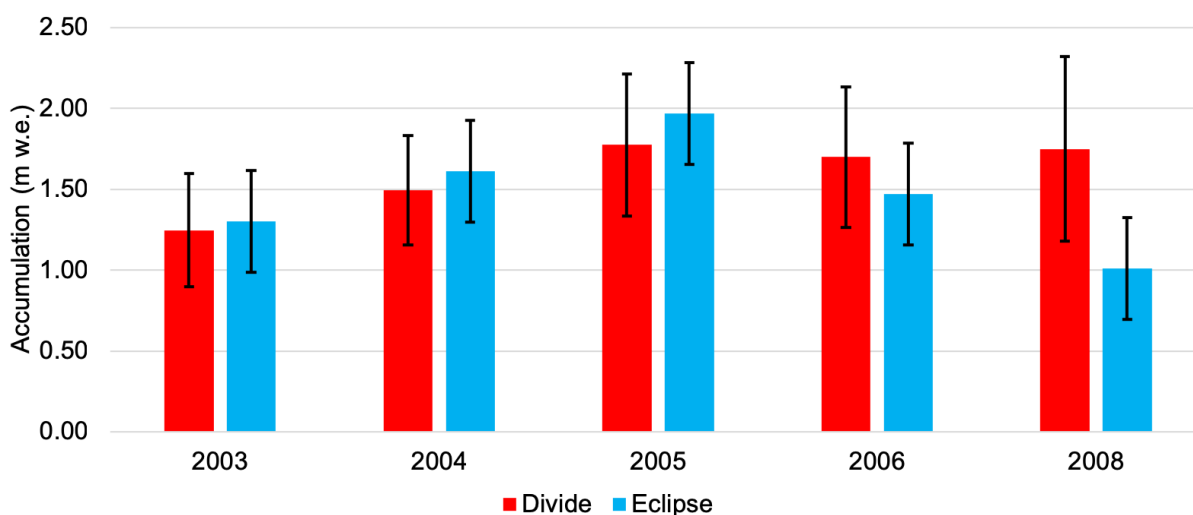
Figure 2.12 Accumulation at Eclipse and Divide. At Eclipse (blue), annual accumulation was measured using an ice core, and at Divide (red), it was recorded by a weather station snow depth sensor in 2003 – 2006 and 2008. Error bars show one standard deviation above and below the recorded values. Accumulation is reported in m water-equivalent.

2.3.4.2. Seasonality of Snowfall at Icefield Divide I examined the seasonal distribution of snowfall at Divide using twice-daily snow depth measurements recorded by the Divide AWS. Four years (2004, 2005, 2006, and 2008) contain complete records of snowfall. 2003, though included above in Figure 2.12, only contains the time frame from early melt season to year's end, as the snow depth sensor was installed in early summer 2003. 2004, 2005, 2006, and 2008 show a common pattern of snowfall at Divide over the course of a typical year (Figure 2.13). During these four years, little accumulation or

ablation occurs during spring, summer is dominated by ablation, and fall and winter experience most of the year's accumulation resulting from a series of snowfall events. Large snowfall events (greater than 1 standard deviation above the year's mean for snowfall in a 12-hour period) occur most often in the fall and winter and least often in the spring and summer (Figure 2.14). During the years 2004, 2005, 2006, and 2008, the fall season experienced an average of 21 large snowfall events, winter averaged 17 events, spring averaged 8.5, and summer averaged 7, suggesting that spring and summer are the driest seasons at Divide, while fall and winter are the wettest.
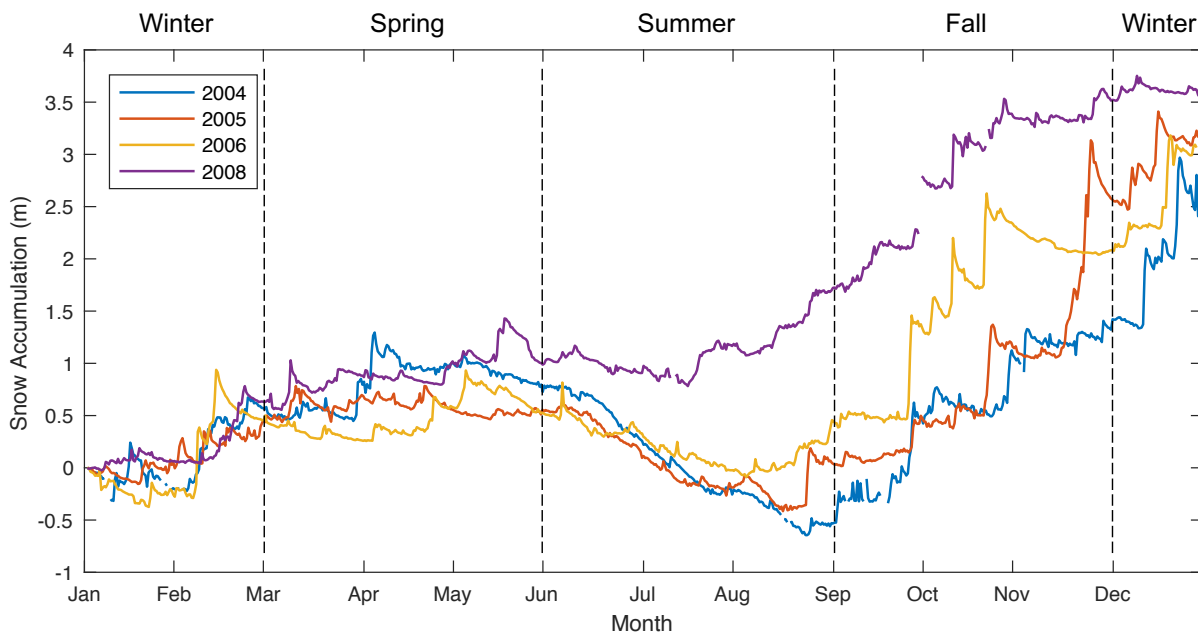
Figure 2.13 Snowfall Seasonality at Divide. Four years of snowfall data (2004, 2005, 2006, and 2008) from the Divide weather station show the typical distribution of snowfall over the course of the year. Seasonal delineations are marked with dotted lines.
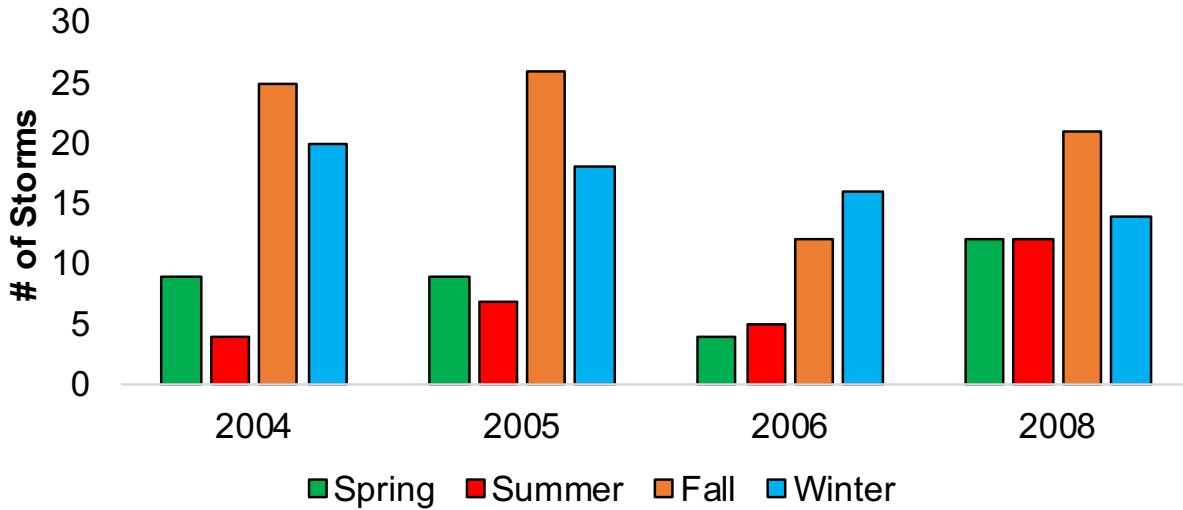
Figure 2.14 Seasonality of Large Snowfall Events at Divide. Four years of snowfall data (2004, 2005, 2006, and 2008) from the Divide weather station show the amounts of large snowfall events (> 1 standard deviation above the year's mean for snowfall in a 12-hour period) that occurred in each season. The leftmost bar in each annual grouping represents spring (green), followed by summer (red), fall (orange), and winter (blue).

2.3.4.3. Meteorology Associated with Snowfall Events at Icefield Divide I examined two multi-day

storm events at Divide versus two multi-day periods without snowfall, using NCEP/NCAR Reanalysis

data. The storm events were chosen based on their inclusion of at least one 12-hour period with

snowfall greater than one standard deviation above the mean for 12-hour snow depth change. For

comparison, I chose periods without snowfall from the same week as each storm event, defining a non-

snowfall event as a span of days in which net ablation occurred at Divide. I found storm events to be

characterized by warm temperatures, low sea level pressure (SLP), and an increased flux of moisture at

850 hPa from the subtropical Pacific basin as well as from the North Pacific region off the west coast of

Alaska (Figure 2.15). These storm events occurred during November 22-24, 2005 (1.2 m snowfall in two

days) and during October 9-10, 2006 (0.7 m snowfall in one day). Temperatures in the UKD region during

the November 2005 snowfall event were 10-15 °C warmer, SLP was 30 hPa lower, and the magnitude of

southerly moisture flux at 850 hPa was at least 0.02 g kg^{-1} m s^{-1} higher than during the non-snowfall

event. During the October 2006 snowfall event, temperatures were 0-10 °C warmer, SLP was 4 hPa

lower, and the magnitude of southerly moisture flux at 850 hPa was at least 0.06 g kg^{-1} m s^{-1} higher than

during the non-snowfall event. During both storm events, a low pressure center existed over the south-

central Alaskan coast (988 hPa, November 2005) or Aleutian Islands (984 hPa, October 2006) that was

not present during non-storm events.

a.
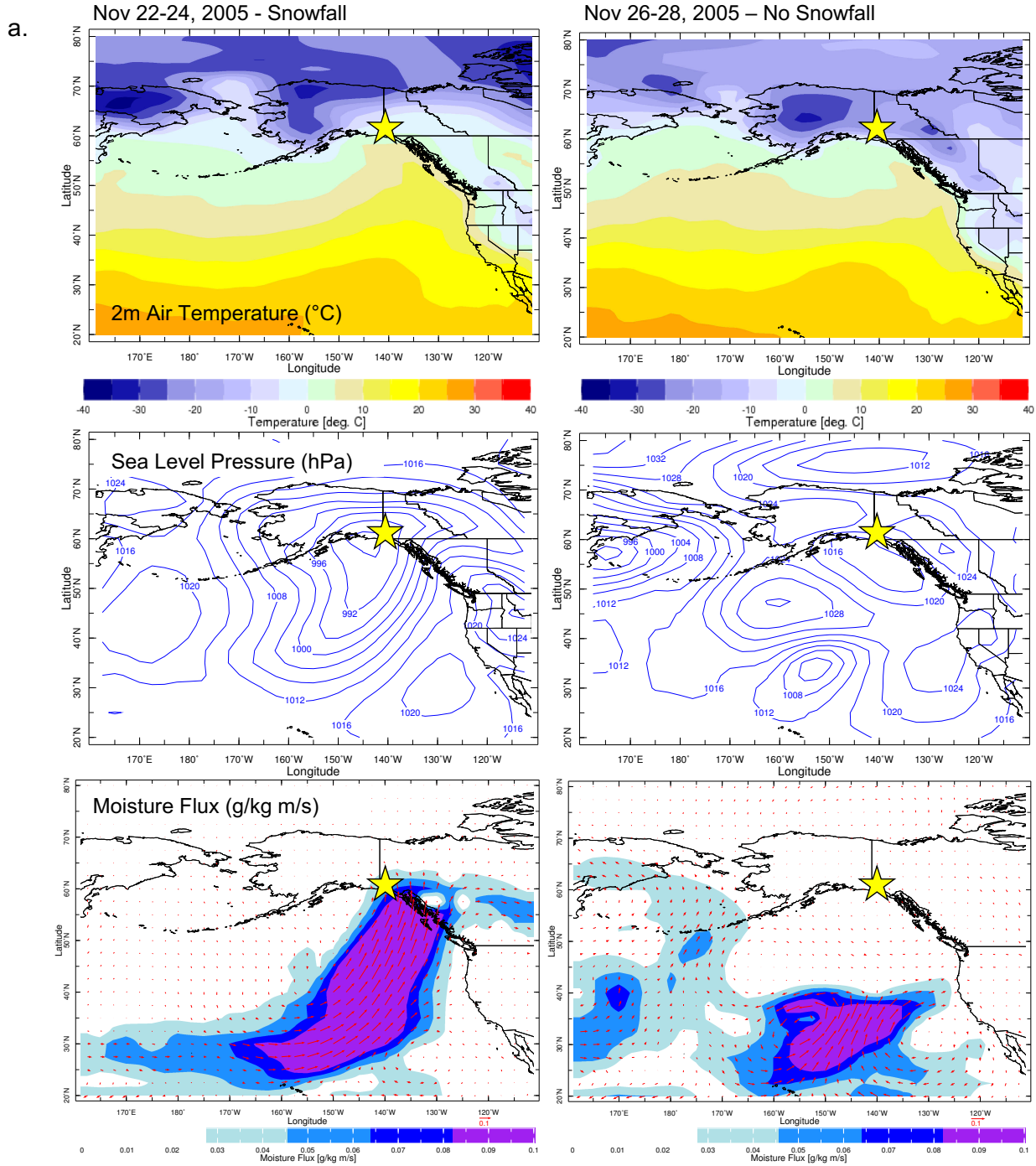
Figure 2.15 Meteorological Characteristics of Storm and Non-Storm Events

b.
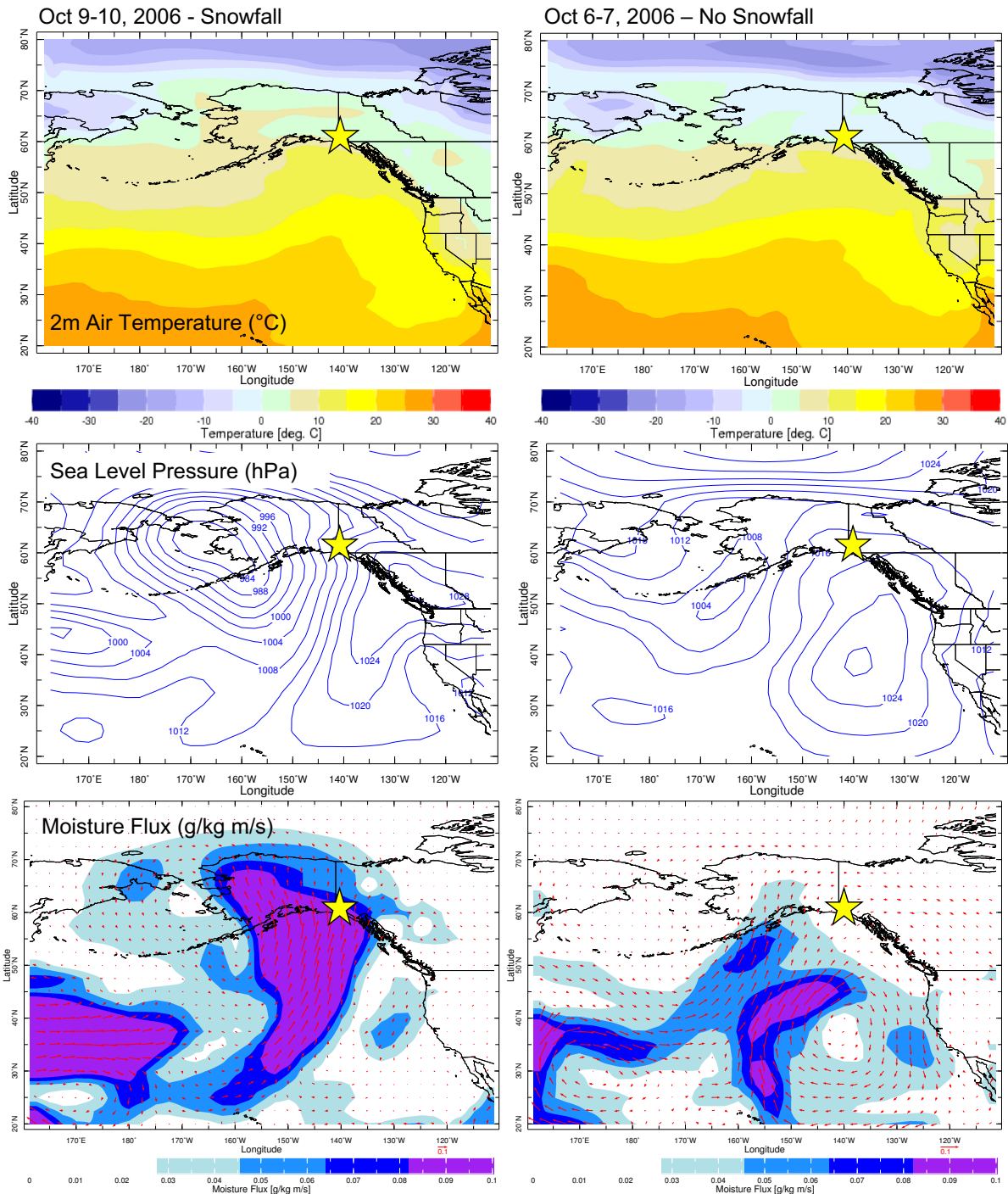
Figure 2.15 Continued. Meteorological Characteristics of Storm and Non-Storm Events. A timespan of days with heavy snowfall (left column) in (a) November 2005 (1.2 m in 2 days) and (b) October 2006 (0.7 m in 1 day), versus timespans of days in the same week with no snowfall (right column). Air temperature in top row, sea level pressure in middle row, and moisture flux at 850 hPa (magnitude indicated by color bar and length of red arrows, direction indicated by red arrows) in bottom row. Location of UKD region marked with yellow star. Data from NCEP/NCAR Reanalysis.

2.3.5. Melt and Isotope Signal Preservation in Arctic Ice Cores

While I found shared variability and spatial coherence of the temperature and accumulation signal in the UKD region, differences in the magnitude of temperatures between Eclipse and Divide leads to significant differences in melt and isotope signal preservation. The high accumulation rate and negligible amount of melt at Eclipse allows the climate record in Eclipse ice cores to be preserved, with no noticeable reduction in isotopic amplitude over at least a 14-year timespan (Figure 2.16). The matching structure, timing and amplitude of δD and d-excess peaks also indicates accuracy in the depth-age scales of these Eclipse cores.
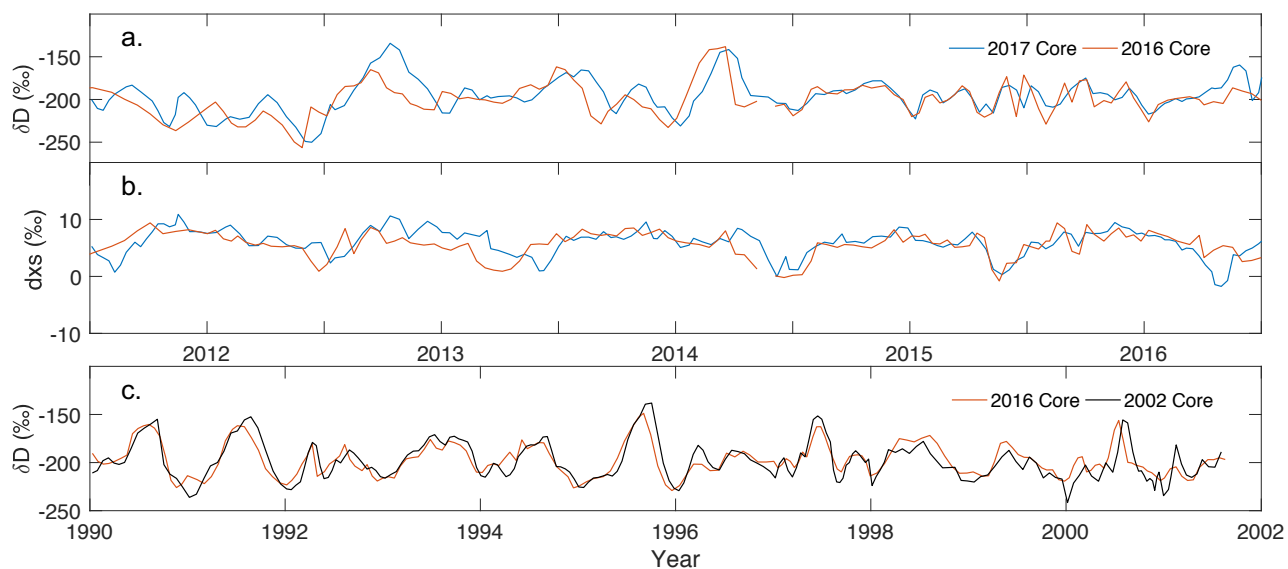
Figure 2.16 Eclipse Isotope Records. Timescale overlaps between (a) hydrogen isotopes and (b) deuterium excess, measured in ice cores drilled at Eclipse in 2017 (blue) and 2016 (orange), and (c) hydrogen isotopes measured in cores drilled at Eclipse in 2016 (orange) and 2002 (black).

The 2017 Eclipse firn core shows a reduction in isotopic range of only 2.13% from the top of the core to its base (Table 2.1). In contrast, the isotope signal measured in a firn core from Divide shows a reduction in isotopic range of 81.25% from top to base (Figure 2.17, Table 2.1). The isotope signal measured in the Eclipse and Divide firn cores is shown versus depth, as I was unable to confidently formulate a depth-age scale for the melt-affected Divide core. Despite the observed difference in signal preservation, the reduction in isotopic range at Divide does not appear to have caused its isotope record

to significantly alter the local meteoric water line (LMWL) (Figure 2.18). The LMWL refers to the linear relationship between $\delta^{18}O$ and δD observed at a particular location.

Extending my analysis to include Arctic ice coring sites outside of the St. Elias, I found warm mean summer temperatures (>-1.5 °C) and low accumulation rates (<1.2 m w.e. yr^{-1}) to be associated with the greatest loss in isotope signal amplitude from firn core top to base (>25% amplitude reduction) (Figure 2.19, Table 2.1).
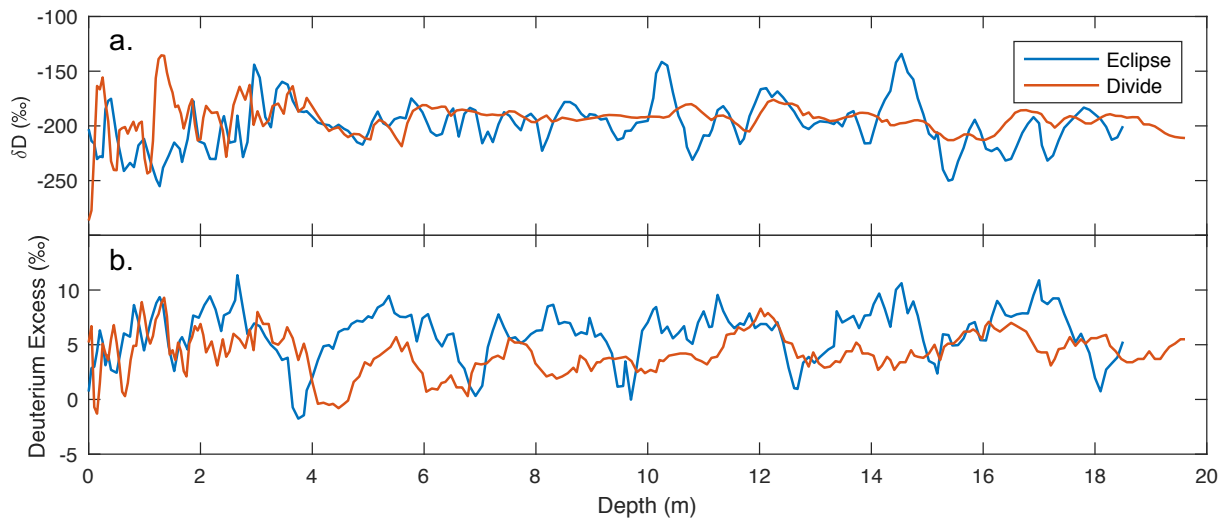
Figure 2.17 Comparison of Isotope Signal Amplitude in Eclipse and Divide Firn Cores. Hydrogen isotope (δD, a) and deuterium excess signals (b) for ~20 m firn cores drilled at Eclipse (blue) and Divide (orange) show severe melt-related reduction in amplitude with depth in the Divide core, but not in the Eclipse core. The reduced amplitude is not as evident in the d-excess record, although the Eclipse core still shows a larger isotopic range than the Divide core below ~5 m depth.
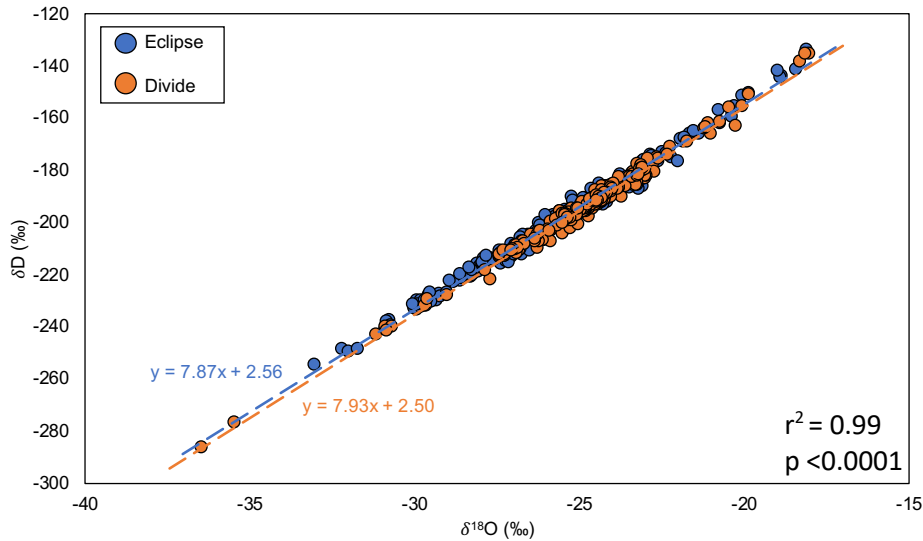
Figure 2.18 Upper Kaskawulsh-Donjek Region Local Meteoric Water Line. Linear equations and lines shown for scattered hydrogen (δD, y-axis) and oxygen (δ^{18}O, x-axis) isotopes measured in firn cores from Eclipse (blue) and Divide (orange).
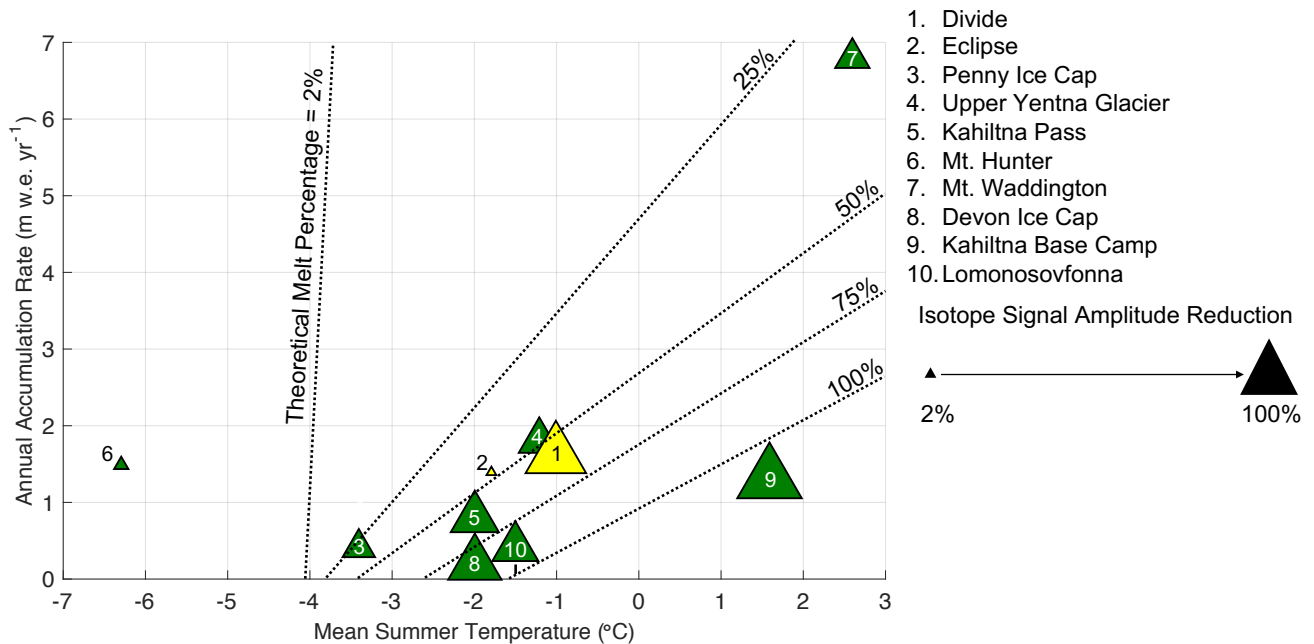
Figure 2.19 Factors Driving Arctic Isotope Signal Alteration from Melt. Arctic ice core sites are numbered according to the legend at right, with Divide and Eclipse in yellow and other sites in green. Isotope signal alteration, quantified by percent reduction in oxygen or hydrogen isotope amplitude from the top quarter to the bottom quarter of firn cores drilled in each location, is scaled according to the legend in top left. Larger markers represent more reduction in signal amplitude. Dotted lines delineate theoretical melt percentage values in relation to mean summer temperature and annual accumulation, based on the Meyer and Hewitt (2017) meltwater process model.

2.4. Discussion

2.4.1 Meltwater Percolation Dynamics

GPR profiles show evidence of a wetter snowpack (Figure 2.5) and firn aquifer (Figure 2.4) at Divide in contrast with a drier snowpack and no aquifer at Eclipse. Physical evidence of a firn aquifer was also found at approximately the same elevation as Divide in a different coring site on the Kaskawulsh Glacier (~2,600 m ASL), where Ochwat (2019) drilled into a layer of saturated firn at 35.6 m depth. The saturated layer extended at least 1 m in depth and prevented further drilling (Ochwat 2019). The observed differences in firn saturation at Eclipse and Divide occur despite an average temperature difference of <2 °C between the two locations.

Meyer and Hewitt (2017) constructed a continuum model for meltwater flow through compacting snow to investigate how meltwater runoff, refreezing, and englacial storage, as well as firn temperature and density profiles, respond to climatic forcing. Three model simulations demonstrate the effects of temperature and accumulation rate on the behavior of meltwater within firn (Meyer and Hewitt 2017). In the first simulation, which modeled an accumulation zone with an annual accumulation rate of 1.7 m w.e. yr^{-1} and a mean annual surface forcing of -141.4 W m^{-2}, firn temperature and porosity profiles show alteration via summer meltwater percolation, which feeds a perennial aquifer sitting below 10 m depth. In the second simulation, with the same accumulation rate and a lower mean annual surface forcing of -200 W m^{-2}, melt is limited and no firn saturation or aquifer occurs. In the third, with the same accumulation rate and a higher mean annual surface forcing of -117 W m^{-2}, the most melt occurs of the three simulations, leading to a rapid decrease in porosity with depth. This accumulation zone's low porosity prevents deep meltwater percolation into the firn, causing the meltwater to remain closer to the surface where it is less insulated from surface cooling in winter. Thus, meltwater refreezes rather than residing in a firn aquifer (Meyer and Hewitt 2017). Kuipers Munneke et al. 2014 and Steger

et al. 2017 similarly found that perennial firn aquifers occur where there is sufficiently high

accumulation and where an intermediate amount of melting occurs.

Several of the Arctic ice core sites included in my investigation empirically demonstrate the

climatological characteristics necessary for the formation of a firn aquifer. Divide and Eclipse, with

accumulation rates of 1.6 m w.e. yr^{-1} and 1.4 m w.e. yr^{-1}, would represent the first and second

simulations, respectively, in the Meyer and Hewitt (2017) model. In this case, a small temperature

difference with a constant accumulation rate leads to a large amount of melt and the formation of a firn

aquifer at Divide, yet less melt and no aquifer at Eclipse. This concept is illustrated in Denali National

Park as well, where UYG (mean summer temperature -1.2 °C, annual accumulation rate 1.8 m w.e. yr^{-1})

contains a firn aquifer and a melt-altered isotope signal. The existence of the aquifers at Divide and UYG

indicates that (1) firn temperatures in these sites are warm enough to preserve melted snow in the

liquid state rather than allowing it to refreeze into melt layers, and (2) porosity allows for meltwater to

percolate to depths at which it is insulated from winter surface cooling. In contrast, Mt. Hunter (mean

summer temperature -6.3 °C, annual accumulation rate 1.5 m w.e. yr^{-1}) experiences neither melt nor a

firn aquifer.

Because the meltwater residing in firn aquifers at Divide and UYG has not refrozen within the

snowpack, calculations of melt percentage (MP) in these locations based on melt layer stratigraphy are

likely underestimations of the true MP. Divide and UYG have MPs of 4.8% and 3.4% respectively, based

on melt layer stratigraphy. However, the observed isotope signal degradation and theoretical MPs in

each site suggests higher MPs (60% and 45%) than were calculated using the melt layer stratigraphy

method (Figure 2.19, Table 2.1). For this reason, mean summer temperature and accumulation rate

appear to be better metrics of isotope signal amplitude reduction than MP in sites with isothermal

snowpacks that preserve water in the liquid state. Most of the Arctic sites without firn aquifers similarly

have higher theoretical MPs than is calculated using melt layer stratigraphy.

In sites without firn aquifers, percolated meltwater is able to refreeze into melt layers within the snowpack. In these sites, MP may be used as a measurement of meltwater percolation, which can result in isotope signal degradation depending on the typical thickness of annual accumulation layers in the site. In Figure 2.19, the Mt. Waddington ice core site on Combatant Col (British Columbia, Canada) is a notable outlier from the rest. One might expect it to suffer more signal degradation given its relatively high mean summer temperature (2.6 °C) in comparison to the other sites. However, Mt. Waddington is much wetter than the other sites, receiving an average of 6.8 m w.e. snow accumulation annually. Because melt cannot percolate completely through the annual snowpack, the isotope signal at Mt. Waddington shows only a 26.27% signal amplitude reduction from melt (Neff et al. 2012). KBC and Divide, despite cooler mean summer temperatures, experience near-total melt-induced signal loss (81.25% and 92.23%). They receive much less accumulation than Mt. Waddington, which allows meltwater to percolate throughout the annual snowpack. The effect of annual accumulation rate is also evident in the cases of Eclipse, Kahiltna Pass, and DIC, all of which experience mean summer temperatures of between -1.8 °C and -2 °C, yet have different accumulation rates. Eclipse receives 1.4 m w.e. yr^{-1} and retains its signal amplitude over time, while Kahiltna Pass and DIC receive 0.8 m w.e. yr^{-1} and 0.2 m w.e. yr^{-1} with signal amplitude reductions of 51.32% and 63.14%, respectively.

2.4.2. Spatial Coherence of Temperature in the UKD Region

My comparison of *in situ* instrumental temperature records from Eclipse and Divide shows spatial coherence of the temperature signal over the Divide – Eclipse distance, indicated by high ($r^2>0.95$) and significant ($p<0.0001$) correlations between temperature records from each site, with Divide consistently at least 1 °C warmer than Eclipse (Figures 2.6 and 2.7). Eclipse also shows a more dampened signal, which is likely explained by different instrumentation. Placement of the Eclipse iButton temperature sensor inside of a sealed plastic container and shielded by rocks, while necessary for the device's protection and retrieval, could also have prevented it from recording temperature extremes. In

contrast, the temperature sensor attached to the Divide AWS was directly exposed to ambient air temperature with only minor shielding for protection against solar radiation. This difference would not be expected to, and does not appear to have, impacted the shared variability in temperature between Eclipse and Divide. However, shielding would be expected to cause a warm bias in the Eclipse air temperature readings, meaning that the observed 1 °C drop in temperature from Divide to Eclipse is a real climate phenomenon and may even be an underestimation. MODIS measured a temperature drop of 1.8 °C from Divide to Eclipse, further indicating that shielding of the Eclipse instrumentation results in a warm air temperature bias.

The MODIS remotely-sensed dataset, composed of daily average LSTs collected over a 16-year timespan, confirmed that annual temperature is strongly correlated between Eclipse and Divide using consistent instrumentation in both sites (Figures 2.8 and 2.9). The 414 m elevation increase from Divide to Eclipse and the -1.8 °C temperature change measured by MODIS gives a lapse rate of -4.3 °C km^{-1}, a value nearly in agreement with that of southeast Alaska's Denali National Park (-4.6 °C km^{-1}) and with the lapse rate of -4.4 °C km^{-1} in the alpine region of Spitsbergen, Svalbard (Pohjola et al. 2002).

2.4.3. Implications of Melt for Remotely-Sensed Temperatures in the UKD Region

In the MODIS LST dataset, the summer season showed the weakest spatial temperature coherence (r^2 = 0.57, Figure 2.9). This result was not matched by the *in situ* air temperature data, which showed summer, fall, and winter to have a similarly coherent spatial temperature signal (r^2 = 0.74 – 0.76, Figure 2.7). Overall, summer also showed the poorest correlations between MODIS and *in situ* records (Figure 2.10). This anomaly is likely due to a component of the MODIS post-processing method. To derive LST values from snow-covered surfaces, the MODIS LST algorithm assigns the land cover type as "snow and ice" and assumes an emissivity value accordingly (ε = 0.993 and 0.990 for MODIS bands 31 and 32, respectively) (Wan 2008). Spectral albedo of alpine snowpacks has been shown to be dependent upon grain size and impurity content (Grenfell et al. 1981), and grain size is dependent upon snow

41

temperature. Because I have established that Divide experiences more melt than Eclipse and maintains

a snowpack at or above freezing during the summer melt season, Divide's surface albedo would be

expected to differ from that of Eclipse in summer. I hypothesize that the delineation of "snow and ice"

in the LST algorithm is too broad to accurately reflect site-specific differences in surface emissivity

related to diverse snow types in alpine regions.

The emissivity assumption in the algorithm may also play a role in the seasonal dependence of

the MODIS cold bias in comparison with *in situ* temperatures (Figure 2.11). A prior study in the Yukon

found a systematic cold bias of 5 – 7 °C in average LST for locations with >90 % snow cover in

comparison with downscaled air temperatures (Williamson et al. 2017). Others have attributed this cold

bias to the clear-sky nature of MODIS LST readings, which exclude days with cloud cover from the

dataset (Westermann et al. 2012). Because cloud cover is associated with higher minimum skin

temperatures, this introduces a cold bias. In the MODIS dataset from Divide, LSTs were colder than the

in situ air temperatures by an annual average of about 3.5 °C over 2002 – 2017 at Divide and by an

average of 3.6 °C over 2016 – 2017 at Eclipse. Seasonally, however, the cold bias between MODIS

sensors and the AWS ranged from negligible in spring to as much as -8.6 °C in winter (Figure 2.11). This

seasonal relationship is of importance in studies drawing analyses entirely from MODIS LST readings in

snow-covered areas, as assuming a consistent cold bias year round may result in flawed interpretations.

2.4.4. Spatial Coherence of Accumulation in the UKD Region

Despite different sampling methods at Eclipse (ice core) and Divide (automated snow depth

sensor), the accumulation signal appears spatially coherent. Accumulation at Divide (~1.6 m w.e. yr^{-1})

was within one standard deviation of that at Eclipse (~1.4 m w.e. yr^{-1}) for all five years of reliable data

coverage (Figure 2.12).

At Eclipse, annual accumulation was derived from the 2016 ice core. Uncertainty inherent in the

Eclipse ice core depth-age scale results either from human error in manual layer counting using

glaciochemical signals, or from the influences of atmospheric circulation and topography on the isotope

signal, which can reduce the clarity of the isotope-air temperature relationship (discussed in depth in

Chapter 3). The well-matched isotope signal peaks between the 2016 and 2002 cores (Figure 2.16), as

well as the use of known reference horizons in constructing the 2002 core chronology, make it unlikely

that the 2016 core timescale is off by more than ±1 year. However, in this analysis, even an error of one

year could result in a timescale mismatch between the Eclipse ice core record and the Divide AWS

accumulation record.

The Divide snow depth instrument has several sources of uncertainty as well. Burial of the

station by snow as well as tilt of its mast caused significant data loss over the station's decade of data

collection and ultimately resulted in its removal in 2012. While it is difficult to quantify the uncertainty

introduced by mast tilt, I removed station readings that were clearly impacted by it. The amount of wind

scour at Divide is another unknown, which has the potential to redistribute snow and introduce error in

readings of accumulation and ablation.

While I cannot draw certain conclusions from five years of data collection, the shared

accumulation variability in four out of five years despite many sources of uncertainty inspires confidence

that the Eclipse ice core record is a reasonable approximation of the local annual accumulation signal.

Over greater distances in the region, precipitation has been shown to be more spatially variable than

temperature (Rupper et al. 2004, Kelsey et al. 2012). A study of the Wolverine and Gulkana Glaciers in

Alaska showed that glacier mass balance, driven by accumulation and ablation, correlated poorly with

local weather station precipitation records (Bitz and Battisti 1999). Similarly, correlations between Mt.

Logan accumulation and precipitation recorded by regional weather stations are low and inconsistent,

which has been attributed to complex regional topography and the spatial heterogeneity in precipitation

that results from it (Rupper et al. 2004). Kelsey et al. (2012) found higher correlations between Eclipse

ice core stable isotope fluctuations and regional weather station temperatures than between Eclipse ice

core accumulation and weather station precipitation. They posit that this results from the differing spatial scales of variability for each phenomenon (Kelsey et al. 2012). The proximity of Eclipse and Divide in space and elevation compared with the coastal stations used for ice core comparisons in previous work likely results in a more consistent accumulation pattern between them. For this reason, the Divide AWS dataset is unique in providing a means of investigating relationships between the Eclipse ice cores and instrumental records that accurately reflect climate patterns at the ice core site. This is discussed in depth in Chapter 3.

2.4.5. Examination of Temperature Coherence in the Spring Season

In both the *in situ* and MODIS temperature records, the spring season showed the strongest spatial temperature signal coherence (Figures 2.7 and 2.9). The replication of this finding using two different methods of instrumental temperature data collection indicates that this is a real climatic phenomenon rather than simply a bias introduced by instrumental sampling.

I hypothesize that the strong spring temperature coherence between Eclipse and Divide relates to spring being one of the UKD region's driest seasons. Divide AWS snowfall data at 12-hour resolution shows spring and summer to be the driest seasons of the year, whereas fall and winter frequently experience large precipitation events (Figures 2.13 and 2.14). During precipitation events, southerly moisture flux moves northwards from where it first reaches land in the coastal Gulf of Alaska region. Where precipitation is occurring, air temperature is warmer than in locations where no precipitation is occurring (Figure 2.15). While accumulation appears to be spatially consistent in the UKD region on an annual timescale (Figure 2.12), it is less consistent on a daily timescale, where precipitation tends to reach Divide before it reaches Eclipse to the north. During seasons with frequent storm events, i.e. fall and winter, this spatial precipitation pattern would lead to poorer temperature coherence in both *in situ* and remotely-sensed records during these seasons.

Additionally, spatial differences in daily snowfall would cause Eclipse and Divide to contain more variable snow types during seasons with frequent storms. As discussed above, the MODIS LST algorithm does not differentiate between snow types, which are more variable during seasons in which Divide and Eclipse contain new and old snow on different days. Spring and summer MODIS LST data also showed smaller cold biases in comparison to *in situ* data, likely related to fewer cloudy days in these seasons, thus fewer days excluded from the "clear-sky" MODIS LST dataset. As cloudy days tend to be warmer, this would tend to decrease the cold bias in seasons with less cloud cover.

I hypothesize that poorer summer temperature coherence in comparison to spring in the *in situ* dataset relates to differences in snow type due to differential melting. The Divide snowpack contains more liquid water in the summer than the Eclipse snowpack, which would result in differing albedos and surface heating in each location. Additionally, the shielding of the Eclipse iButton temperature sensor (discussed above) could have prevented extreme warm temperatures from being recorded at Eclipse during the summer, whereas warm temperature extremes are less likely to occur in the UKD region during spring.

2.4.6. Preservation of the Deuterium Excess Signal at Icefield Divide

The d-excess signal measured in the Divide firn core shows a higher amplitude throughout the core than the δD signal alone (Figure 2.17). I hypothesize that this is due to either (1) the derivation of d-excess using the global meteoric water line (d-excess = $\delta D - 8*\delta^{18}O$) rather than the LMWL at Divide, which replaces the multiplicative factor of 8 with a factor of 7.93 (Figure 2.18), or (2) a slight seasonal difference in the LMWL, with the warm season (April – September) $\delta D/\delta^{18}O$ slope equal to 7.94, while the cold season (October – March) slope is equal to 7.98. Either of these, or both, would result in a d-excess signal that appears more amplified throughout the firn core than either stable water isotope alone.

2.4.7. Implications of Melt-Related Isotope Signal Loss in the Arctic

In my case study of Eclipse and Divide, I identified a distinct temperature threshold of <2 °C between signal preservation and melt-induced signal alteration in the UKD region (Figures 2.17 and 2.19). Similar threshold processes have also been observed in other locations, in which relatively small increases in temperature are associated with disproportionate increases in melt. On the Antarctic Peninsula, a 1.6 °C warming since the late 1400s is associated with a tenfold increase in melt (Abram et al. 2013), and at Mt. Hunter, a summer temperature increase of at least 1.7 °C over the past 400 years resulted in a sixtyfold increase in melt (Winski et al. 2018). The increase in average summer temperature from -6.3 °C at the Mt. Hunter summit plateau (62.93°N, 151.08°W, 3,912 m ASL) to -2.0 °C at Kahiltna Pass (63.07°N, 151.17°W, 2,970 m ASL) results in a much higher signal amplitude loss of 51.32% from the top to the base of a Kahiltna Pass firn core, compared to an amplitude loss of only 4.56% in a Mt. Hunter firn core (Figure 2.19).

I also observed a threshold process related to differences in annual accumulation rate between Arctic sites with comparable summer temperatures. The mean summer temperature of Lomonosovfonna Icefield in central Spitsbergen (-1.5 °C, 1,255 m ASL) is close to Eclipse's -1.8 °C. Yet Lomonosovfonna's low annual accumulation rate of 0.4 m w.e. yr^{-1} and MP of 33% leads to a near-halving in isotope signal amplitude from 0 – 9 m depth to 27 – 36 m depth (Pohjola et al. 2002), compared to the negligible isotope signal loss at Eclipse with its accumulation rate of 1.4 m w.e. yr^{-1}.

The isotope signal preservation observed at Eclipse inspires confidence that the site contains a complete and unaltered Holocene paleoclimate record. At present, Arctic temperatures in northwestern Canada are estimated to exceed those of the HTM by 1.7 ± 0.7 °C, based on a ~13.6 ka summer temperature reconstruction using precipitation isotopes measured in permafrost (Porter et al. 2019). From this, it can be inferred that if Eclipse does not experience signal loss due to melt at present, its ice is likely to contain a preserved climate record of at least the past ~12,000 years. However, given its

proximity to the observed meteorological threshold between signal preservation and melt-induced alteration, it is likely that the Eclipse isotope record will begin to show reduced amplitude akin to the signal observed at Divide if climate change continues unchecked and temperatures rise greater than ~2 °C above pre-industrial norms. Considering rapid warming in the Arctic, the current climate approaches a threshold of warmth such that the climate of the mid- to late 21st century and beyond may not be recorded in ice core proxy records from temperate Arctic glaciers.

2.5. Conclusions

In my case study of two sites in the St. Elias with similar accumulation rates, I found a 1 – 2 °C temperature difference to have a large effect on the degree to which isotope signal amplitude is affected by meltwater percolation. In Arctic ice coring sites in general, sites with mean summer temperatures of approximately -1.5 °C and above tend to show melt-related signal alteration, unless they receive high accumulation rates. Sites with low accumulation rates ($<$~1.2 m w.e. yr^{-1}) require colder summer temperatures for isotope signal preservation. In relation to other Arctic coring locations, Eclipse is a site with a well-preserved isotope signal, while Divide's is one of the most altered, indicating that signal preservation can vary significantly even between sites that are relatively close in distance and elevation. This makes the selection of a coring site challenging when addressing research questions that rely on the preservation of a clear isotope signal throughout the Holocene. Awareness of the relationship between snowpack meltwater content, snow type, and surface albedo is also important when using remotely-sensed surface temperature products that do not differentiate between snow types.

Despite observed differences in temperature, melt amount, and isotope signal preservation, I found the temperature and accumulation signals to show strong spatial coherence (i.e. shared variability) between Eclipse and Divide. This result indicates that I can confidently use meteorological records from the Divide AWS to investigate relationships between the Eclipse isotope record and

47

meteorological data recorded by instruments, provided that I account for the consistent temperature

offset between Eclipse and Divide. This investigation will be the focus of the remainder of this thesis and

will supplement past work that focused on examining atmospheric characteristics associated with

anomalous isotopes in the St. Elias Mountains.

CHAPTER 3

INVESTIGATION OF CLIMATIC SIGNIFICANCE AND SEASONALITY IN STABLE ISOTOPE RECORDS FROM

ECLIPSE ICEFIELD, ST. ELIAS MOUNTAINS, YUKON, CANADA

3.1. Background and Motivation

3.1.1. Ice Core Isotope Records: The δ Thermometer

Polar ice core-based isotope paleotemperature reconstructions rely on the well-established linear

relationship observed in the middle and high latitudes between annual stable isotope ratios measured in

precipitation and mean annual temperature at the precipitation site (Dansgaard 1964). This relationship

is known as the spatial delta (δ)/temperature (T) slope. The temporal δ/T relationship refers to the

change in isotope δ as regional climate regimes shift over time, and some past inferences of warming

and cooling in polar regions have used the spatial δ/T relationship as an analogue for the temporal (e.g.

Grootes et al. 1993), built on the assumption that the spatial δ/T slope remains constant over time

(Guan et al. 2016). However, factors specific to a location and its climatic history can reduce the ability

of an isotope δ/T relationship to reflect an accurate temperature record over space and time. Several

studies have reported observed discrepancies between spatial and temporal δ/T relationships. For

example, a borehole temperature reconstruction in Greenland revealed a warming of ~23 °C ± 2 °C since

the Last Glacial Maximum (LGM), indicating a temporal slope of 0.35‰°C^{-1}. This value is approximately

half of the present spatial slope (Cuffey et al. 1995, Jouzel et al. 1997).

Low-frequency noise in a site's isotope record can be introduced by changes in large-scale

atmospheric circulation that affect the isotopic composition of an air mass from moisture source to

precipitation site (Jouzel et al. 1997). Changes in circulation and climate regime can also alter the

seasonality of precipitation, which in turn influences the isotopic composition of precipitation and its

dependence on site temperature. Model simulations suggest that a shift in the seasonality of

precipitation at the LGM is responsible for a warmer bias in temperature reconstructions inferred from

the temporal δ/T slope than from the spatial slope (Krinner et al. 1997, Werner et al. 2000).

Precipitation is an atmospheric process characterized by large seasonal variability and relatively small

long-term variability, so its deposition is inherently sensitive to shifts in seasonal timing (Steig et al.

1994).

High-frequency noise in isotope records results from spatial variability in snowfall deposition

(Jouzel et al. 1997) and microphysical properties within clouds (Fisher 1991). An additional source of

error in reconstructing temperatures from isotope records results from the fact that stable water

isotopes only record air temperature during precipitation events. Particularly in polar regions, this can

cause overestimations of mean annual temperature (Jouzel et al. 1997).

Empirical results and most general circulation models (GCMs) support the use of an "isotope

paleothermometer" in interpreting local temperature variability, as long as the isotope record is

calibrated with site-specific temperatures (Jouzel et al. 1997). Calibration can be accomplished in several

ways, including inferring temperature change over time using melt layer stratigraphy (Koerner and

Fisher 1990, Winski et al. 2018), modelling isotope fractionation using GCMs fitted with isotope tracer

diagnostics (Jouzel et al. 1997), and empirically comparing isotope records in snow and firn layers with

instrumental temperature records.

Empirical calibration with time-stamped meteorological records is the most accurate method

and has been used in ice core sites in Antarctica and Greenland, as well as in at least one alpine site in

South America. At South Pole station, an instrumental temperature record is available since 1958 and

shows mean annual and maximum hydrogen isotopes to be correlated with mean annual and summer

temperatures, while minimum hydrogen isotopes are only weakly correlated with winter temperatures

(Jouzel et al. 1983). In Greenland, isotope records show many of the major features that are present in

weather station temperature records, with a δ/T calibration slope of ~0.5 ‰/°C (Shuman et al. 1995).

Hurley et al. (2015) used snow pit and short core δ^{18}O data along with instrumental snow-height

measurements on Peru's Quelccaya Ice Cap to develop an understanding of the atmospheric dynamics

associated with regional snow deposition. Their analysis suggests that ice core records from the

Quelccaya Ice Cap may be useful in reconstructing past South American summer monsoon dynamics

(Hurley et al. 2015).

3.1.2. Relationships Between North Pacific Ice Core Isotope Records and Atmospheric Circulation

Most alpine ice core sites lack reliable, local long-term instrumental temperature records, making local

isotope-instrumental comparisons difficult. Past work in the St. Elias Mountains and North Pacific region

has studied relationships between ice core chemistry and large-scale atmospheric circulation to identify

factors other than local temperature at the time of snowfall that influence isotope records in the North

Pacific (Figure 3.1). These studies have also built understanding of the influence of atmospheric

variability on North Pacific climate.

Hydroclimate in the North Pacific is dominated by the Aleutian Low Pressure System (ALow), a

predominantly wintertime semi-permanent feature in the Gulf of Alaska (GOA) region. The intensity of

the ALow is influenced by tropical Pacific Ocean sea-surface temperatures (SSTs) through the Pacific

North America (PNA) teleconnection pattern (Wallace and Gutzler 1981). Atmospheric teleconnection

patterns facilitate moisture transport from moisture source to precipitation site. In the PNA region, the

cyclonic circulation of the ALow carries moisture from south of the GOA into south-central Alaska and

northwestern Canada. A recently observed doubling of precipitation in the Alaska Range since ~1840

C.E., measured in an ice core record from Mt. Hunter (3,900 m above sea level [ASL]), reflects a rapid

strengthening of the ALow to its strongest levels within the past millennium (Winski et al. 2017). The

precipitation increase is also reflected in weather station records from southern Alaska, and it is driven

primarily by a rise in wintertime precipitation totals (Winski et al. 2017). Mechanically, this precipitation

increase results from the enhanced southerly flow of warm, moist air masses into the Gulf of Alaska

region during strong ALow regimes (L'Heureux et al. 2004). ALow intensification has been shown to

result from a Rossby wave extratropical response to warming SSTs in the tropical Pacific and Indian

Oceans, which manifests as the positive PNA pattern (Alexander et al. 2002, Deser et al. 2004), and the

record of ALow strength is similar to tropical proxy records of precipitation and El Niño Southern

Oscillation (ENSO) variability (Osterberg et al. 2014).
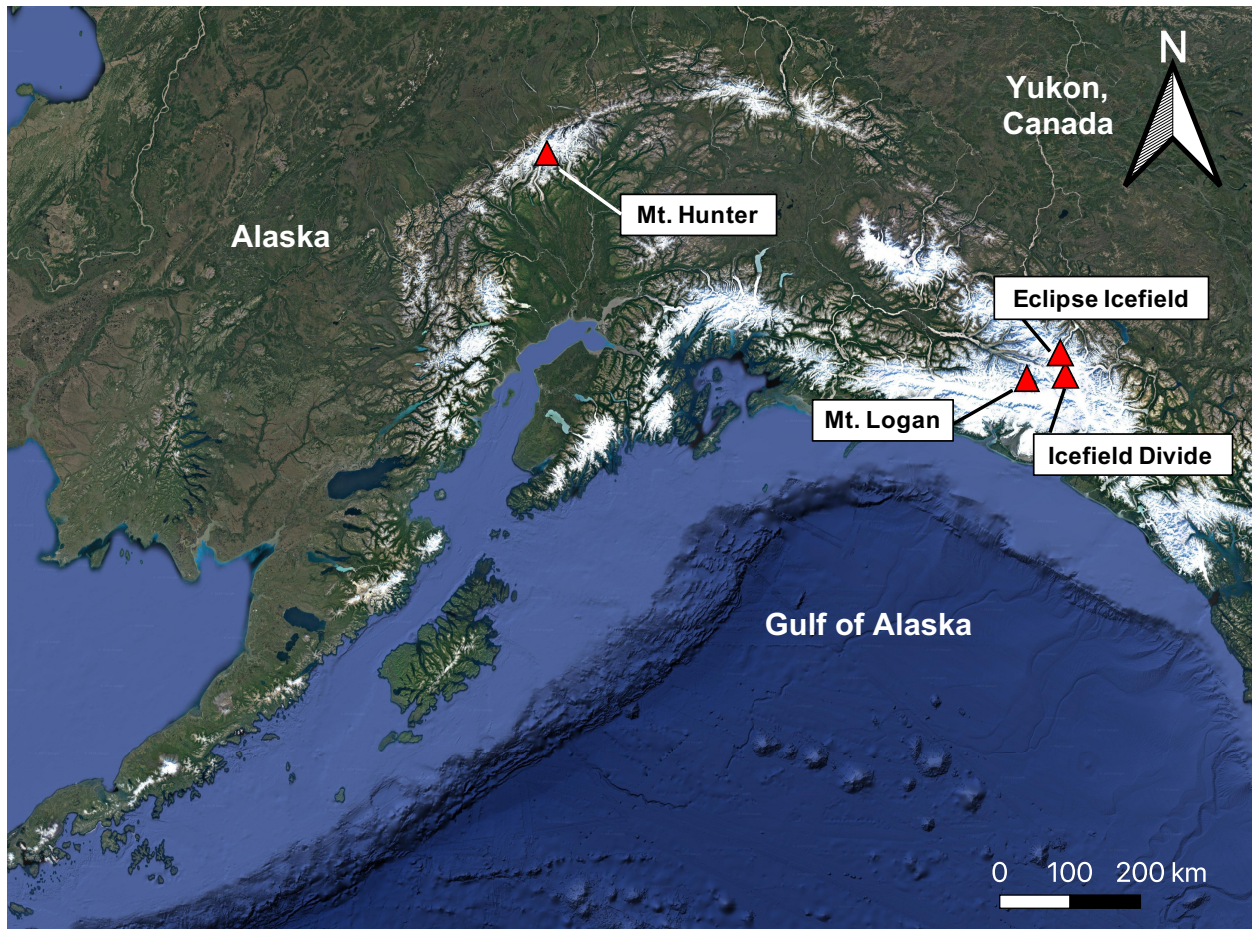
Figure 3.1 Map of Selected Ice Core Sites in the North Pacific. Ice core records from Mt. Hunter (Winski et al. 2017) and Mt. Logan (Holdsworth et al. 1992, Moore et al. 2002b, Fisher et al. 2004, 2008, Field et al. 2010, Osterberg et al. 2014) show significant relationships with tropical ocean conditions and El Niño Southern Oscillation variability. Eclipse Icefield is a focus of this chapter, and its ice core isotope records have been compared with regional temperature, with mixed results (Wake et al. 2002, Kelsey et al. 2012). An ice core was drilled at Icefield Divide by our University of Maine group in 2018, and the weather station temperature record from Divide is a focus of this chapter. Image obtained from Google Earth.

Ice core records collected from high-altitude sites in the St. Elias similarly reveal strong relationships with atmospheric circulation and distant ocean conditions. Summit areas are able to sample from free-troposphere conditions without local effects masking the tropical climate signal, which can occur at lower sites and coastal weather stations (Pepin and Seidel 2005), and the St. Elias mountain range is located at the ending point of extratropical Pacific storm tracks (Blackmon 1976, Orlanski 2005). The first ice core collected in the St. Elias was retrieved from the Northwest Col (NW Col) of Mt. Logan in 1980, at 5,340 m ASL (Holdsworth et al. 1992). The NW Col stable oxygen isotope (δ^{18}O) record shows features distinct from the records of cores collected in Canadian Arctic and Greenland sites near the North Atlantic (Holdsworth et al. 1992). If the NW Col δ^{18}O record were interpreted solely as a record of past temperature, one would conclude that the Little Ice Age in the southwest Yukon was warmer than the time period after it (Holdsworth et al. 1992, Moore et al. 2002b, Zdanowicz et al. 2014); however, other temperature-sensitive paleoclimate proxies from the Yukon show that this was likely not the case (Wiles et al. 2004, Youngblut and Luckman 2008, Bunbury and Gajewski 2009). Thus, isotopes from Mt. Logan ice cores are thought to represent atmospheric circulation rather than temperature.

Identifying relationships between local and distant atmospheric circulation patterns, such as ENSO, and North Pacific ice core records is integral to the calibration of records with climate dynamics on a broader scale. By comparing an altitudinal transect of stable isotope timeseries from the lower troposphere (Jellybean Lake) to the upper troposphere (Mt. Logan summit plateau), along with model simulations, Fisher et al. (2004) attributed abrupt shifts in the St. Elias isotope records to past changes in atmospheric circulation from zonal to meridional flow regimes. Fisher et al. (2008) expanded on this interpretation by associating these δ^{18}O shifts with variations in ENSO. This is based on an observed correspondence between zonal (meridional) moisture transport characteristic of weak (strong) ALow, and strong La Niña (El Niño) regimes (Fisher et al. 2008, Osterberg et al. 2014). Later work introduced a different explanation for the observed variability in the Mt. Logan δ^{18}O record. Using an isotopically-

equipped atmospheric GCM, Field et al. (2010) associated time periods of elevated (lowered) $\delta^{18}O$ with

a stronger (weaker) ALow and enhanced (weakened) southerly moisture transport, particularly during

the cold season. While this interpretation disagrees with Fisher et al. (2004, 2008)'s previous

explanation of Mt. Logan $\delta^{18}O$ variability, and the disagreement has yet to be resolved, both findings

suggest that the Mt. Logan isotope record is predominantly influenced by moisture source and transport

rather than by temperature.

In the St. Elias, distinct differences in ice core records from different sites reflect the effect of

altitude on isotopes in regions of complex topography. Holdsworth et al. (1991) identified a step-

function phenomenon in the isotopic depletion vs. altitude relationship between low elevations and

high elevations in the St. Elias. The authors attribute this observation to topography, with sites between

1,750 and 3,350 m sampling moisture from different air masses than sites above 5,300 m (Holdsworth et

al. 1991). Due to this altitudinal difference, ice core records collected from the NW Col and Prospector

Russell (PR) Col sites on Mt. Logan have distinctly different features compared with cores collected from

Eclipse Icefield (3,017 m ASL) in 1996 and 2002 (Wake et al. 2002, Kelsey et al. 2012) despite the

relatively small distance (45 km) between the two areas (Zdanowicz et al. 2014). Fisher et al. (2004)

observed a 3.5‰ shift in $\delta^{18}O$ at ~A.D. 1840 in a core from PR Col on Mt. Logan, which was matched in a

core from NW Col, but not in the isotope record from Eclipse. The high accumulation rate at Eclipse

(~1.4 m w.e. yr^{-1}) compared with Mt. Logan (~0.42 m w.e. yr^{-1}) also leads to a higher signal-to-noise ratio

at Eclipse, with Eclipse records correlating more strongly with each other than Mt. Logan records

correlate with each other (Kreutz et al. 2004).

Eclipse stable isotope records have been compared with temperature and indices of

atmospheric circulation to elucidate the factors controlling isotope variability in the lower St. Elias.

Stable isotope records from Eclipse display a seasonal pattern, characterized by distinct summer maxima

and winter minima. This pattern is similar to the isotopic seasonality observed in Greenland (Dansgaard

1964) and other Arctic sites (Grumet et al. 1998, Koerner 1997, Goto-Azuma et al. 2006), seemingly

indicating that temperature may be a driver of short-term Eclipse isotope variability. However, an

empirical orthogonal function (EOF) analysis of instrumental temperature records from the North Pacific

in comparison with the 1996 Eclipse oxygen isotope timeseries revealed the temperature-isotope

relationship to be relatively weak, suggesting that non-temperature influences play a dominant role in

driving the isotope variability observed at Eclipse. Using a regional temperature record of combined

data from 31 weather stations, Wake et al. (2002) found that summertime $\delta^{18}O$ signals at Eclipse

represent only a small amount (5 – 10%) of the temperature variability in the broad region extending

from Ketchikan to Kodiak, AK, to the Alaskan interior north of the Alaska range, and at inland sites in the

Yukon and northern British Columbia. Kelsey et al. (2012) found that the 2002 Eclipse core annual stable

isotope record explained 18% of the variability (r = 0.42) shared by 26 regional weather station

temperature records, suggesting that Eclipse isotopes may vary with the type of air mass moving across

the region, and that regional temperature may be regulated by transient large-scale air masses. In an

examination of Eclipse isotopes vs. 500 hPa geopotential height (GPH) patterns, the strongest and most

consistent 500 hPa GPH anomalies were associated with the lowest-ratio cold season isotopes (Kelsey et

al. 2012). The observed GPH anomaly for these seasons closely resembled the negative Pacific-North

America (PNA) pattern. In contrast, cold seasons with the highest isotope ratios, as well as the warm

seasons, were found not to be associated with consistent 500 hPa GPH patterns, although high-ratio

cold seasons were associated with positive Pacific Decadal Oscillation (PDO) and PNA indices (Kelsey et

al. 2012). The cold season stable isotope record was found to be significantly correlated with the PDO,

PNA, and North Pacific Index (NPI), and cold seasons with the highest isotope ratios showed the

strongest potential as proxies of the PNA and PDO, being associated with both atmospheric patterns at

80% confidence (Kelsey et al. 2012). In addition, Wake et al. (2002) found the $\delta^{18}O$ and glaciochemical

timeseries from the 1996 Eclipse core to show significant correlations with Northern Hemisphere sea level pressure (SLP).

3.1.3. Deuterium Excess in the St. Elias

Deuterium excess (traditionally calculated as d-excess = $\delta D - 8*\delta^{18}O$) (Merlivat and Jouzel 1979, Jouzel et al. 1989) is influenced by the sea surface temperature (Jouzel et al. 1982, Johnsen et al. 1989, Dansgaard et al. 1989) and/or relative humidity (Pfahl and Sodemann 2014) of the moisture source region, as well as the temperature of the deposition site, which can cause the signal to differ from that of either stable water isotope alone. At the PR Col ice core site on Mt. Logan, $\delta^{18}O$ and d-excess were found to be in anti-phase on an interannual timescale (Fisher et al. 2004).

D-excess displays a sensitivity to elevation related to the differing moisture sources sampled by low- and high-elevation precipitation sites. This phenomenon has been illustrated in model simulations, which showed that d-excess is a proxy for moisture source only at higher elevations in the St. Elias (e.g. Mt. Logan) (Fisher et al. 2004). In an empirical study, Fisher et al. (2008) found differences in the Eclipse d-excess record in comparison to the record from PR Col on Mt. Logan, particularly in the way in which the ~A.D. 1840 shift in d-excess was recorded.

3.1.4. Scientific Goals and Strategy

In this chapter, I compare stable isotope records from a composite of three Eclipse ice cores with instrumental temperature data from Divide, which I showed in Chapter 2 to be strongly correlated with annual and seasonal Eclipse air and land surface temperatures ($p < 0.0001$). In addition, I compare averages and seasonal extremes of Eclipse ice core isotopes with regional temperature, sea surface temperature (SST), SLP, relative humidity (RH), and GPH fields in the mid-troposphere (500 hPa). I address three questions: *(1)* What is the relationship between the Eclipse ice core stable isotope record and local temperature? This tests the findings of Wake et al. (2002), who observed little coherence between the Eclipse isotope record and regional air temperature, e.g. 5 – 10% of regional temperature

variability explained by the Eclipse isotope timeseries. *(2)* What, if any, seasonality is displayed in relationships between the Upper Kaskawulsh-Donjek (UKD) region temperature, stable isotope data, and regional climate variables and indices? This builds on work by Kelsey et al. (2012), who found a distinct seasonality in the significance of relationships between Eclipse stable isotopes and broad-scale climate variability. (3) Is the Eclipse d-excess record a reliable proxy for moisture source conditions? This tests Fisher et al. (2004)'s conclusion that d-excess records from St. Elias locations lower than Mt. Logan do not accurately reflect moisture sources.

Because an ice core timescale with sub-annual accuracy is essential when testing isotope seasonality and coherence with instrumentally-measured variables, I use an updated Eclipse 2002 core chronology in the following analyses. I also introduce data from two new firn cores drilled at Eclipse in 2016 and 2017. These cores significantly lengthen the timescale overlap between proxy records and reanalysis products and unlike the 2002 Eclipse core, they were analyzed from surface to base for both δD and δ^{18}O. This makes it possible to formulate complete timeseries of d-excess for the 2016 and 2017 core records and examine relationships between Eclipse d-excess and local and broad-scale climate variability. The AWS temperature record from Divide gives a new and unique opportunity to build on past work that was limited by the lack of observational meteorological records in proximity to the Eclipse ice core site. Results enhance understanding of the isotope-temperature relationship in the UKD region, as well as the Eclipse ice core record's potential as a proxy for variability in atmospheric circulation.

3.2. Methods

Analysis procedures are modeled after those developed by Kelsey et al. (2012) and Wake et al. (2002) to investigate relationships between the Eclipse isotope record, regional temperature, large-scale atmospheric circulation, and climate indices. Both studies analyzed relationships between Eclipse ice core records from 2002 (Kelsey et al. 2012) and 1996 (Wake et al. 2002) versus temperature records

from weather stations in the GOA region, SLP and 500 hPa GPH records from the reanalysis products, and climate indices of the PDO, PNA, and ENSO.

3.2.1. Datasets

For this analysis, I incorporate instrumental, ice core, reanalysis, and climate index datasets. *In situ* temperatures from the UKD region were collected by the AWS at Divide. The AWS dataset spans 14 complete years from 2003 – 2016, and the data collection procedure is described in detail in Chapter 2. The stable isotope (δD) record from Eclipse is a composite record of data from three ice cores, drilled in 2002, 2016, and 2017. Drilling, laboratory analysis, and timescale development procedures for each of these cores are discussed in Chapter 2. The composite δD record compiles time frames from 2011 – 2017 from the 2017 core, 2002 – 2011 from the 2016 core, and 1948 – 2002 from the 2002 core. Because $δ^{18}O$ was not analyzed throughout the 2002 core, all d-excess data were obtained from the 2016 and 2017 cores. The d-excess dataset spans from 1990 – 2017.

Regional temperature, SLP, 500 hPa GPH, SST, and RH data were obtained from the National Centers for Environmental Prediction (NCEP)-National Center for Atmospheric Research (NCAR) reanalysis 2.5° x 2.5° horizontal-resolution dataset (Kalnay et al. 1996). Timespans included in the analysis are those for which each variable (temperature, δD, and d-excess) overlaps with the reanalysis dataset: 2003 – 2016, 1948 – 2016, and 1990 – 2016, respectively. The NCEP/NCAR reanalysis product effectively simulates spatial patterns of variability in the vicinity of the North Pacific basin (Saravanan 1998) and captures large-scale interannual variability in moisture transport associated with ENSO (Mo and Higgins 1996). It is frequently referenced in studies of proxy-climate relationships in the North Pacific (Moore et al. 2001, 2002a, 2002b, 2003, Rupper et al. 2004, Hartmann and Wendler 2005, Kelsey et al. 2010, 2012, Winski et al. 2017, 2018).

Because d-excess has been associated with moisture source conditions, i.e. SST (Jouzel et al. 1982, Johnsen et al. 1989, Dansgaard et al. 1989) and/or relative humidity (Pfahl and Sodemann 2014), I compare the d-excess timeseries, but not the temperature or δD timeseries, with these variables.

Monthly-averaged climate index values from 1950 – 2016 were obtained for the Pacific Decadal Oscillation (PDO, Zhang et al. 1997, Mantua et al. 1997), Multivariate ENSO Index (MEI, Wolter and Timlin 1993, 1998), Niño-3.4 (Trenberth 1997), Pacific-North America pattern (PNA, Wallace and Gutzler 1981), and Arctic Oscillation (AO, Higgins et al. 2000). These datasets were downloaded from the National Oceanic and Atmospheric Administration (NOAA) National Centers for Environmental Information webpage (https://www.ncdc.noaa.gov/). I calculated correlation coefficients for the temporal relationships between each climate index and UKD region temperature, δD, and d-excess using annually- and seasonally-averaged data.

3.2.2. Regional Climate Correlations and Composites

I created correlation maps using the Climate Reanalyzer (https://climatereanalyzer.org/), produced and maintained by the Climate Change Institute, University of Maine, USA. All correlation maps use the NCEP/NCAR Reanalysis Version 1 (NCEP/NCAR V1) dataset along with annually-averaged Divide temperature, Eclipse δD or d-excess data (2003 – 2016).

The high accumulation rate at Eclipse (~1.4 m w.e. yr^{-1}) allows for the delineation of two seasons within each annual accumulation layer. During the formulation of depth-age scales for the Eclipse ice cores, we picked the most probable beginning of each year based on seasonal δD oscillations, assigning a date of January 1st to each annual layer's depth of δD minimum. I then assigned each year's midpoint (July 1st) to each layer's depth of δD maximum and assumed a constant accumulation rate between these two dates. Henceforth, "warm season" refers to April – September, and "cold season" refers to October – March.

I created composite maps of temperature, SLP, 500 hPa GPH, SST, and RH anomalies, based on

1981 – 2010 climatological norms, using the NOAA Earth System Research Laboratory (ESRL) Physical

Science Division (Boulder, Colorado)'s Monthly/Seasonal Climate Composites tool

(http://www.esrl.noaa.gov/psd/). I divided seasonally-averaged temperature, δD, and d-excess values

into six groupings, outlined in Table 3.1 and Figure 3.2. Seasons included in each composite map are

based on these groupings. Hereafter, "anomalous" refers to values >1 standard deviation above or

below the mean for a given season and dataset, and "normal" refers to values within ±1 standard

deviation of the mean. To match the reference frame of the NOAA ESRL Climate Composites tool, for the

composite anomaly plots, I removed seasons from each group that belonged to years outside of the

1981 – 2010 time frame.

Table 3.1 Seasonal Data Groups

High Warm Season	Anomalously high temperatures/d-excess values/δD ratios in the warm season
Normal Warm Season	Normal temperatures/d-excess values/δD ratios in the warm season
Low Warm Season	Anomalously low temperatures/d-excess values/δD ratios in the warm season
High Cold Season	Anomalously high temperatures/d-excess values/δD ratios in the cold season
Normal Cold Season	Normal temperatures/d-excess values/δD ratios in the cold season
Low Cold Season	Anomalously low temperatures/d-excess values/δD ratios in the cold season
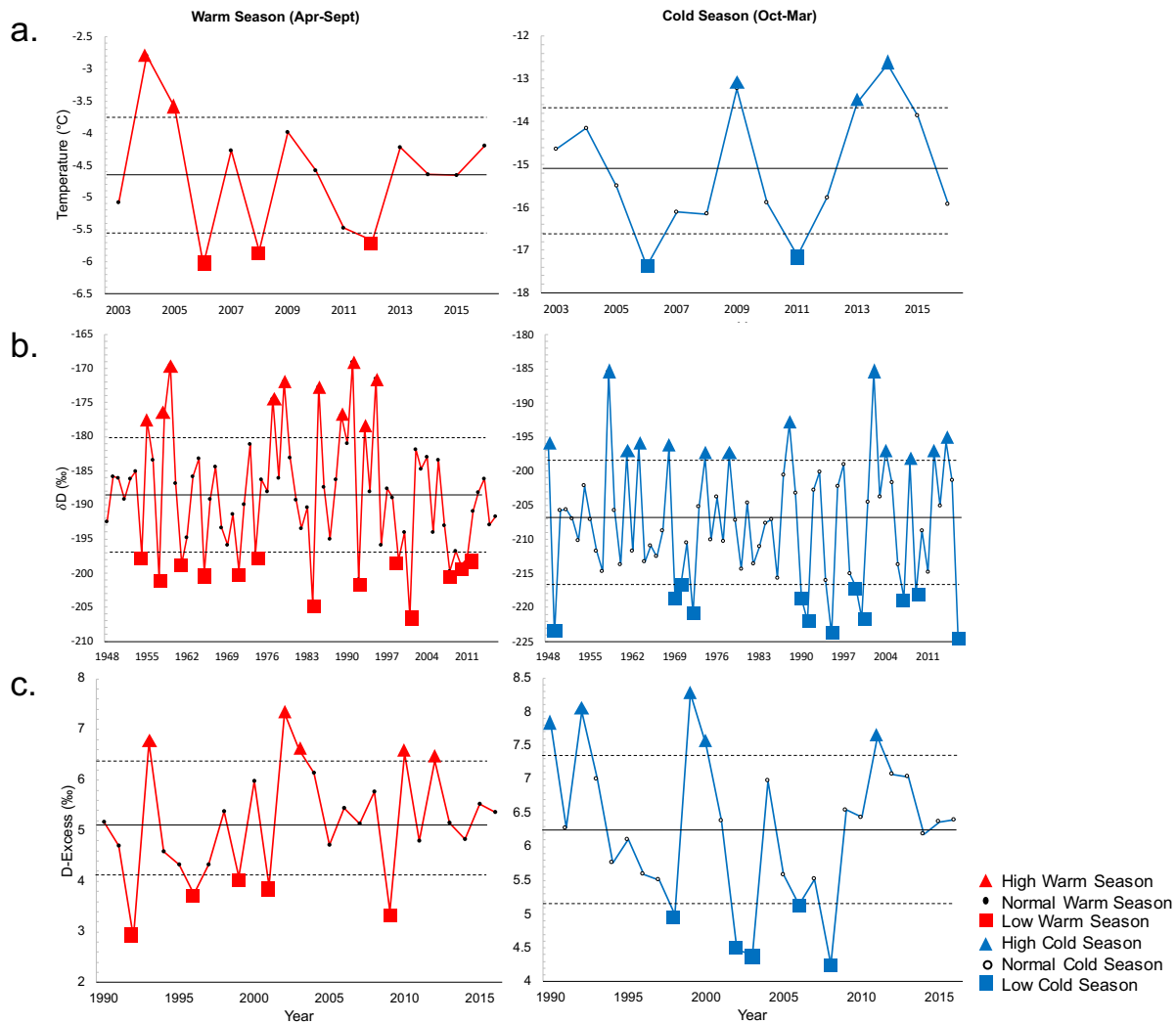
Figure 3.2 Seasonal UKD Region Temperature and Isotope Data Groupings. Seasonally-averaged warm (left column) and cold (right column) temperature data from the Divide weather station (2003 – 2016) (a), δD values from the Eclipse ice core record (1948 – 2016) (b), and d-excess values from the Eclipse ice core record (1990 – 2016) (c). Anomalously high warm season values are marked with red triangles, normal warm season values with closed circles, anomalously low warm season values with red squares, anomalously high cold season values with blue triangles, normal cold season values with open circles, and anomalously low cold season values with blue squares. Solid lines indicate the mean of each dataset, and dotted lines indicate ±1 standard deviation above and below the mean.

3.3. Results

3.3.1. Seasonality in Local Temperature, δD, and Deuterium Excess

Each UKD region variable (temperature, δD, and d-excess) displays a distinctive seasonal distribution

(Figure 3.3). The plots in Figure 3.3 were made using timeseries of each variable, with heat map colors

representing monthly averages over the entire timeseries of each. Warmer colors indicate the highest

density of values for each month. The seasonal distribution is most coherent in air temperature, which

peaks in July and reaches a minimum between December and March. δD displays a similar seasonal

pattern, tending to peak around June. D-excess shows the least consistent seasonal pattern, although it

tends to reach a minimum in April and peak in the vicinity of November – January.
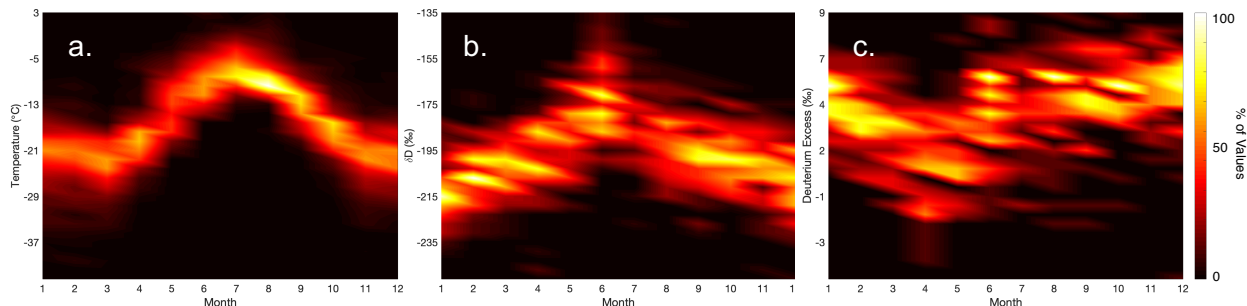
Figure 3.3 Seasonality of UKD Temperature, δD, and D-Excess. Monthly-averaged values of Divide temperature (a), Eclipse δD (b), and Eclipse d-excess (c) show the typical seasonal distribution of each variable according to the color bar (right), with the brightest colors representing the most common value for a particular time of year.

3.3.2. Relationships Between Eclipse Isotopes and UKD Region Temperature

Correlations between the Eclipse isotope record (δD and d-excess) and AWS temperatures were weak

and insignificant over the time frame of dataset overlap (2003 – 2016) (Figure 3.4). Correlation

coefficients (r) for mean annual AWS temperatures versus mean annual δD and d-excess were 0.29 and

0.08, respectively. Seasonal correlations between AWS temperatures and δD were weakly positive and

slightly stronger in the cold season than in the warm season (r = 0.15 for the warm season, r = 0.39 for

the cold season). Seasonal correlations between AWS temperatures and d-excess values were weakly

anticorrelated in the warm season (r = -0.23) and weakly correlated in the cold season (r = 0.18). None

of the annual or seasonal correlations were significant at p < 0.05.
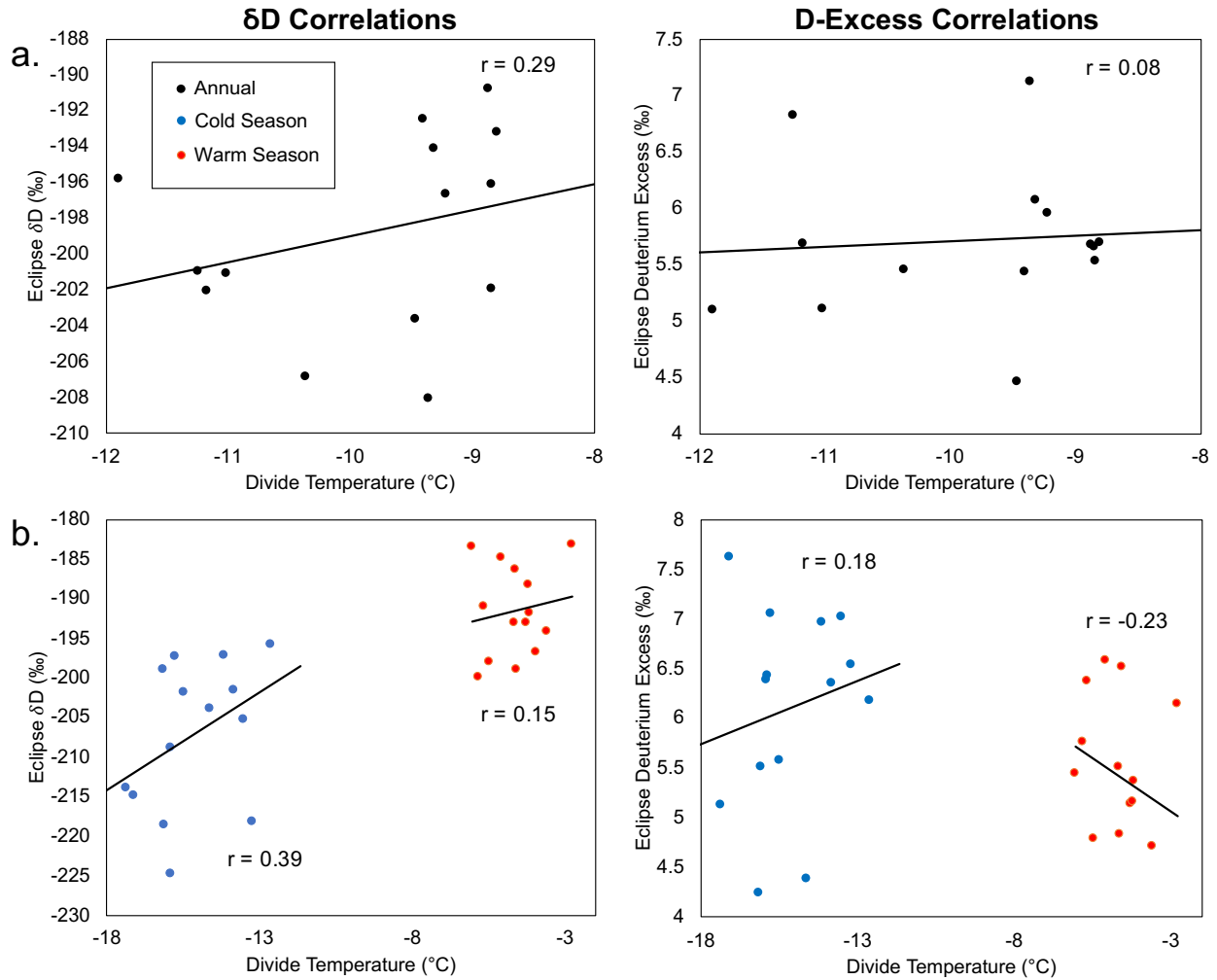
Figure 3.4 Scatter Plots of UKD Region Temperature vs. Eclipse Isotopes. Annual correlations (a) in black and seasonal correlations (b) for the cold season (blue) and warm season (red). Correlations between Divide weather station temperature and Eclipse δD are shown in the left panel, and correlations between Divide weather station temperature and Eclipse d-excess are shown in the right panel. Correlation coefficients are noted next to each scatter.

3.3.3. Annual Relationships Between UKD Region and Broader PNA Region

On an annual timescale, the Eclipse δD record and the Divide AWS temperature record show a similar correlation pattern with temperature variability in the PNA region (Figure 3.5). Correlations between annually-averaged δD and annual mean air temperature and 500 hPa GPH in the broader PNA region are weaker than correlations between annually-averaged UKD temperature and the same variables, yet still

significant at the 0.95 confidence level. SLP in the Aleutian Islands region and central Pacific is correlated with UKD temperature, but UKD δD is instead correlated with SLP in the eastern GOA and southern Yukon.
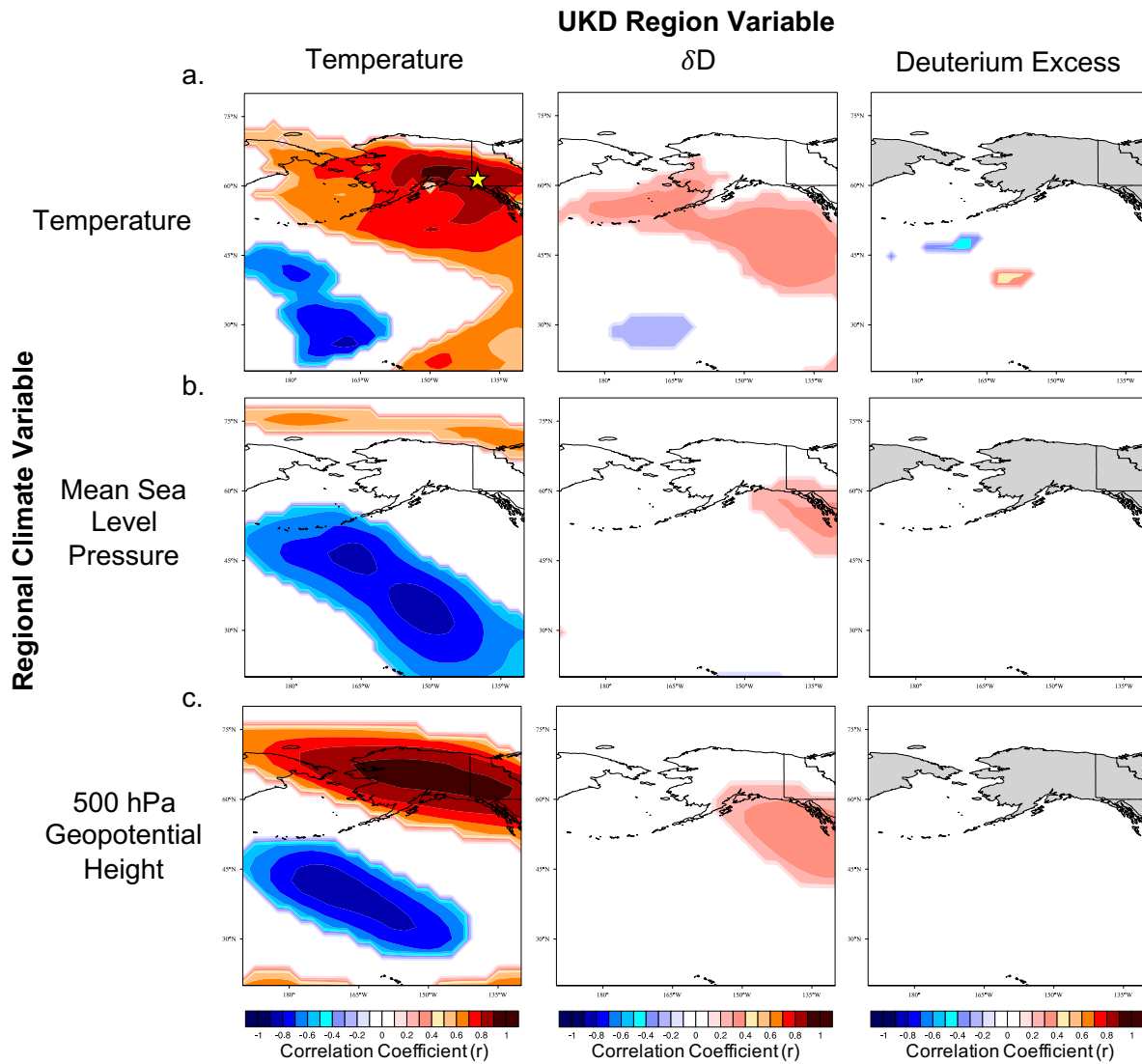
Figure 3.5 Annual Relationships Between UKD Region and Regional Climate Variability. Colored shading shows correlation coefficients at the 0.95 significance level (warm colors = positive correlations, cool colors = negative correlations) between UKD region temperature (leftmost column, 2003-2016), δD (center column, 1948-2016), and d-excess (rightmost column, 1990-2017); and mean 2m temperature (vs. temperature and δD)/ sea surface temperature (vs. d-excess) (row a), mean sea level pressure (row b), and geopotential height at 500 hPa (row c). UKD region is marked with a yellow star in the top left correlation map. Data from NCEP/NCAR Reanalysis V1, maps produced using Climate Reanalyzer, Climate Change Institute, University of Maine, USA.

The Divide AWS temperature record shows strong correlations with annual air temperature from the Alaska and northwestern Canada region (r = 0.5 – 0.9) to the subtropical Pacific (r = 0.5 – 0.7). The temperature record is strongly anticorrelated with SLP and 500 hPa GPH from the Aleutian Islands to the subtropical Pacific (r = -0.5 – 0.8). The temperature record is also correlated with 500 hPa GPH in the equatorial Pacific region (r = 0.5 – 0.7) and in the Alaska/northwestern Canada region (r = 0.3 – 0.9) and is anticorrelated with 500 hPa GPH just south of the Aleutian Islands (r = 0.2 – 0.8). All relationships are significant at the 0.95 confidence level.

While the annually-averaged Eclipse d-excess record shows no notable relationships with PNA-region climate variability at the 0.95 confidence level, the Eclipse δD record is correlated with annual air temperature (r = 0.5 – 0.8) and 500 hPa GPH (r = 0.5 – 0.7) in the Gulf of Alaska (GOA) and Aleutian Islands region. The δD record is correlated with SLP in northwestern Canada (r = 0.5 – 0.7). All relationships are significant at the 0.95 confidence level.

3.3.4 Seasonal Relationships Between UKD Temperature and Broader PNA Region Climate

Seasonal composites of climate variability in the PNA region, which includes the entire North American continent and Pacific basin, revealed a consistent agreement between station temperatures measured at Divide and air temperatures in the broader region during anomalous seasons (Figure 3.6). In general, anomalous cold seasons show composite anomaly patterns that are larger in magnitude and more spatially widespread than anomalous warm seasons. High warm and high cold seasons of the station temperature data are associated with warm temperature anomalies similar in magnitude (>1.5 °C above climatological mean) in the broader Alaska-northwestern Canada-GOA region covering the St. Elias Mountains. Additionally, high warm seasons are associated with a strong (>1.5 °C below climatological mean) cold anomaly in central Canada, and high cold seasons are associated with an equally-strong cold anomaly throughout the eastern to central United States, as well as a weaker cold anomaly in the subtropical Pacific Ocean—characteristic of the positive PNA pattern.

Anomalously cold seasons of the station temperature data show a similar pairing with anomalously cold regional temperatures. Low warm seasons are associated with anomalously cold air temperatures in the GOA and Aleutian Islands region, as well as warm air temperatures in central Canada. Low cold seasons are associated with a strong cold anomaly throughout Alaska and the GOA region, in addition to a warm anomaly covering eastern and central Canada and the United States.

Figure 3.6 Seasonal Anomaly Composite: UKD Region Air Temperature vs. PNA Region Air Temperature. Composites show air temperature anomalies in the PNA region, in relation to the 1981 – 2010 climatological mean, for seasons with anomalous and normal air temperature in the UKD region. Shading according to the color bar. Seasons included in each composite are those with (a) anomalously high warm season values, (b) normal warm season values, (c) anomalously low warm season values, (d) anomalously high cold season values, (e) normal cold season values, and (f) anomalously low cold season values in the Divide station temperature data.

Composites of SLP during anomalous seasons in the Divide AWS temperature dataset show a low SLP anomaly in the Aleutian Islands region during seasons with anomalously high temperature (Figure 3.7). During high warm seasons, this feature is positioned to the west of Alaska and the Aleutians and is characterized by a minimum SLP of 2.25 hPa lower than average. During high cold seasons, the feature shifts southward into the GOA and expands in both spatial extent and magnitude, reaching from the Aleutian Islands through the subtropical Pacific basin. The center of the low pressure system shows

66

a minimum SLP of more than 2.5 hPa below average. High cold seasons also show high pressure

anomalies of 0.25 – 2.25 hPa above normal flanking the low pressure feature to the east and west.
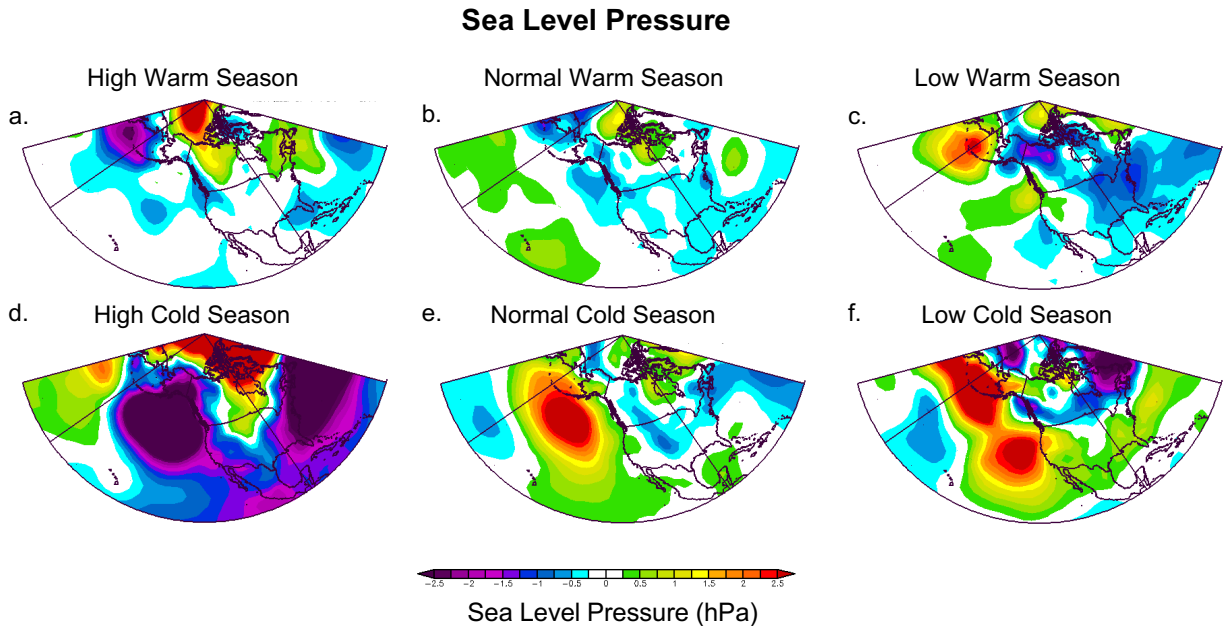
Sea Level Pressure

Figure 3.7 Seasonal Anomaly Composite: UKD Region Air Temperature vs. PNA Region Sea Level Pressure. Composites show sea level pressure anomalies in the PNA region, in relation to the 1981 – 2010 climatological mean, for seasons with anomalous and normal air temperature in the UKD region. Shading according to the color bar. Seasons included in each composite are those with (a) anomalously high warm season values, (b) normal warm season values, (c) anomalously low warm season values, (d) anomalously high cold season values, (e) normal cold season values, and (f) anomalously low cold season values in the Divide station temperature data.

Low warm and cold seasons show the opposite pattern, which is weaker in magnitude and

spatial extent in low warm seasons than in low cold seasons. Here, a high pressure anomaly of 2.25 – 2.5

hPa above normal is located in the Aleutian Islands region, extending down into the subtropics in low

cold seasons. In low cold seasons, the high pressure feature is paired with corresponding low pressure

features higher in the Arctic, centered in northeastern Canada and north of Alaska. In low warm

seasons, the high pressure feature is paired with a low pressure center in northwestern Canada. Normal

cold seasons resemble low cold seasons, showing a high SLP anomaly southeast of the Aleutians, but it is

smaller in distance and magnitude than in the low cold seasons.

In 500 hPa GPH anomaly composites during seasons with high, low, and normal UKD region

temperatures, both high warm and high cold seasons display a high GPH ridge (>40 gpm above normal)

extending from Alaska and northwestern Canada into the Arctic Ocean (Figure 3.8). In high cold seasons,

this feature is larger in magnitude and space, covering most of Canada and the Arctic Circle. It is paired

with a low trough (>40 gpm below normal) in the central Pacific basin. Low cold seasons show the

opposite pattern: ridges in the central Pacific region and west of Alaska, paired with a trough centered

over Alaska and northwestern Canada. Normal cold seasons show a ridge extending from the Aleutian

Islands region to the central Pacific basin, with no corresponding trough. Low warm seasons are

characterized by a ridge west of the Aleutians, a weak (5 – 15 gpm below normal) trough over Alaska,

and a ridge over the eastern Canadian Arctic.

500 hPa Geopotential Height

Figure 3.8 Seasonal Anomaly Composite: UKD Region Air Temperature vs. PNA Region 500 hPa Geopotential Height. Composites show 500 hPa geopotential height anomalies in the PNA region, in relation to the 1981 – 2010 climatological mean, for seasons with anomalous and normal air temperature in the UKD region. Shading according to the color bar. Seasons included in each composite are those with (a) anomalously high warm season values, (b) normal warm season values, (c) anomalously low warm season values, (d) anomalously high cold season values, (e) normal cold season values, and (f) anomalously low cold season values in the Divide station temperature data.

3.3.5. Seasonal Relationships Between Eclipse δD and Broader PNA Region Climate

Notable regional air temperature composite features in seasons with anomalous Eclipse δD values are present in the highest-ratio cold seasons and lowest-ratio warm and cold seasons (Figure 3.9). In high cold seasons, high δD ratios are associated with a cold anomaly throughout eastern Canada of 0.15 – 1.2 °C below normal. Normal cold seasons show a weak cold anomaly of up to 0.45 °C below normal in Alaska, northwest of Alaska, and western Canada. Low warm seasons both display a cold anomaly of up to 0.9 °C below normal west of Alaska, in the GOA, and along the west coast of Canada. Low cold seasons show a weak (up to 0.6 °C below normal) cold anomaly in the Aleutian Islands region and GOA, as well as a warm anomaly of up to 1.5 °C above normal northwest of Alaska.
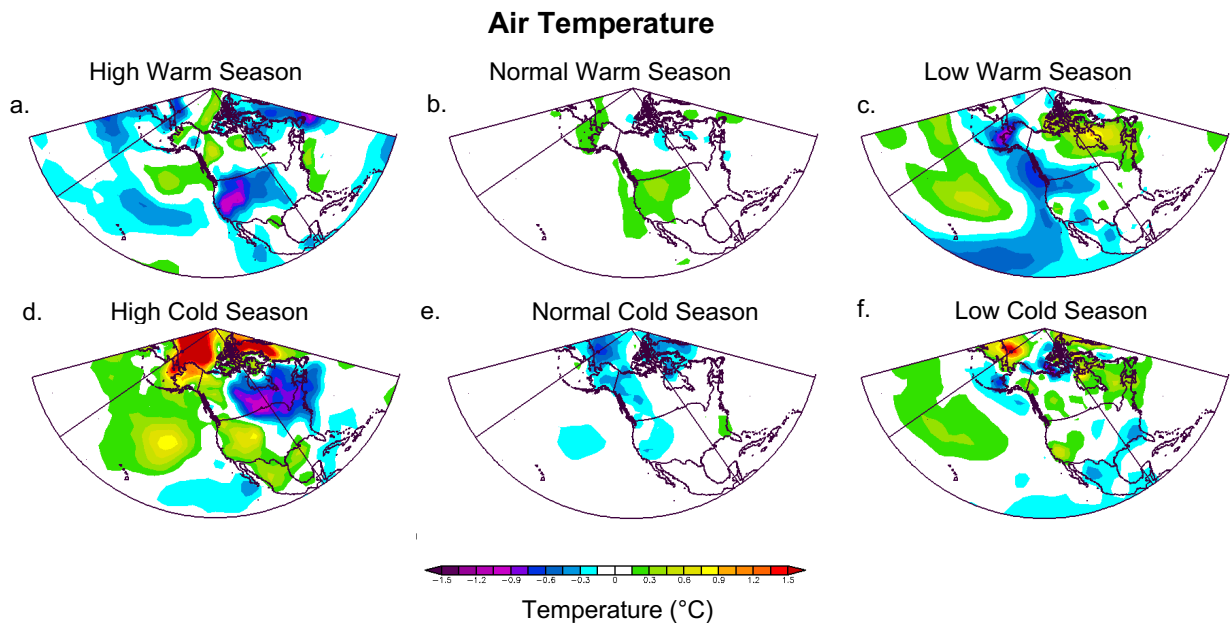
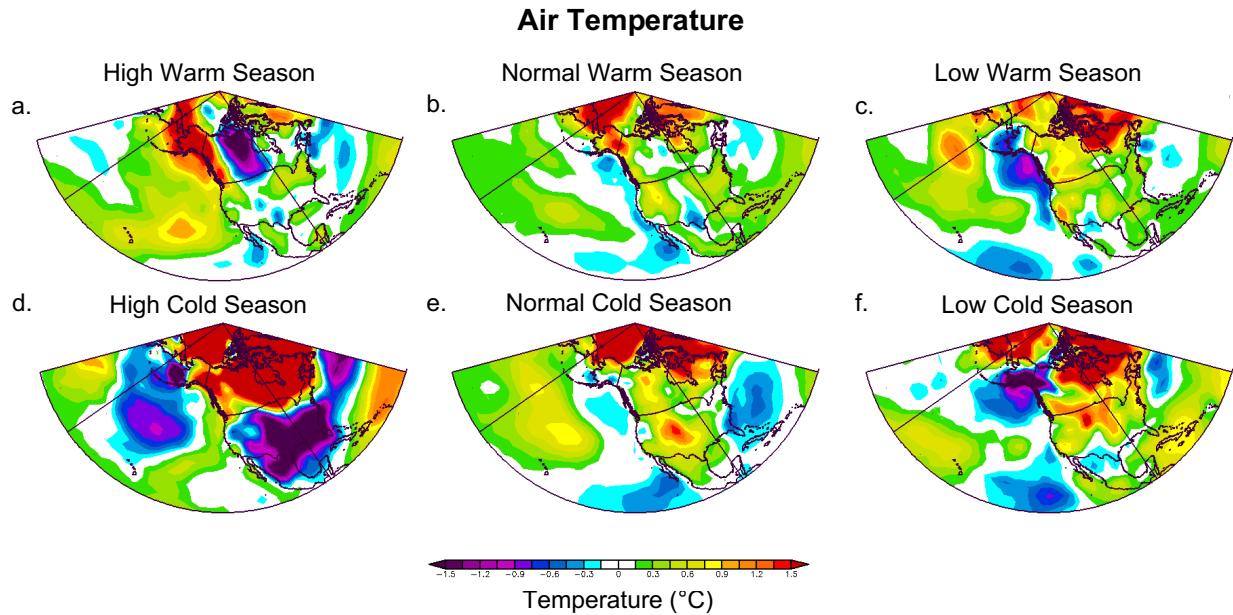

Figure 3.9 Seasonal Anomaly Composite: UKD Region δD vs. PNA Region Air Temperature. Composites show air temperature anomalies in the PNA region, in relation to the 1981 – 2010 climatological mean, for seasons with anomalous and normal hydrogen isotope ratios in the UKD region. Shading according to the color bar. Seasons included in each composite are those with (a) anomalously high warm season values, (b) normal warm season values, (c) anomalously low warm season values, (d) anomalously high cold season values, (e) normal cold season values, and (f) anomalously low cold season values in the Eclipse hydrogen isotope record.

The most prominent feature observed in regional SLP anomaly composites occurs during the highest-ratio cold seasons, which show a high pressure anomaly from the GOA to the central Pacific of

>2.5 hPa above normal at the feature's center (Figure 3.10). The other seasons show weaker composite

SLP patterns, with no notable features present during the normal seasons. High warm seasons show a

low SLP anomaly over the Aleutian Islands and a weak high SLP anomaly centered in the GOA. Low warm

seasons show a widespread weak (up to 1 hPa above normal) high SLP anomaly centered over the

Aleutians and extending downwards into the tropics. Low cold seasons show a weak (up to 1 hPa below

normal) low SLP anomaly in Alaska and extending westward.

Sea Level Pressure

Figure 3.10 Seasonal Anomaly Composite: UKD Region δD vs. PNA Region Sea Level Pressure. Composites show sea level pressure anomalies in the PNA region, in relation to the 1981 – 2010 climatological mean, for seasons with anomalous and normal hydrogen isotope ratios in the UKD region. Shading according to the color bar. Seasons included in each composite are those with (a) anomalously high warm season values, (b) normal warm season values, (c) anomalously low warm season values, (d) anomalously high cold season values, (e) normal cold season values, and (f) anomalously low cold season values in the Eclipse hydrogen isotope record.

The 500 hPa GPH composite for high cold seasons shows a ridge feature of >40 gpm above

normal centered in the GOA and extending to the north and south (Figure 3.11). This is paired with a

trough centered in eastern Canada of up to 40 gpm below normal. Normal and low cold seasons do not

show notable features. In high warm seasons, a trough (up to 30 gpm below normal) is centered near

the Aleutian Islands, paired with a weak ridge over northwestern Canada (up to 25 gpm above normal).

In low warm seasons, a trough of up to 20 gpm below normal is centered over northwestern Canada.

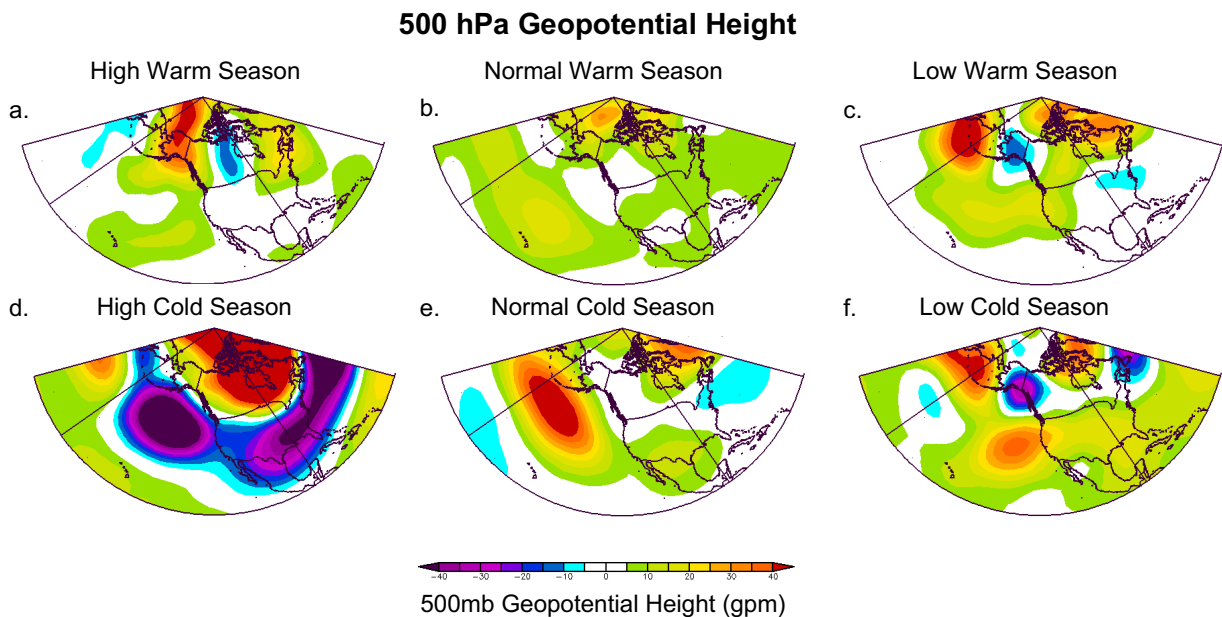Normal warm seasons show no notable features.

500 hPa Geopotential Height
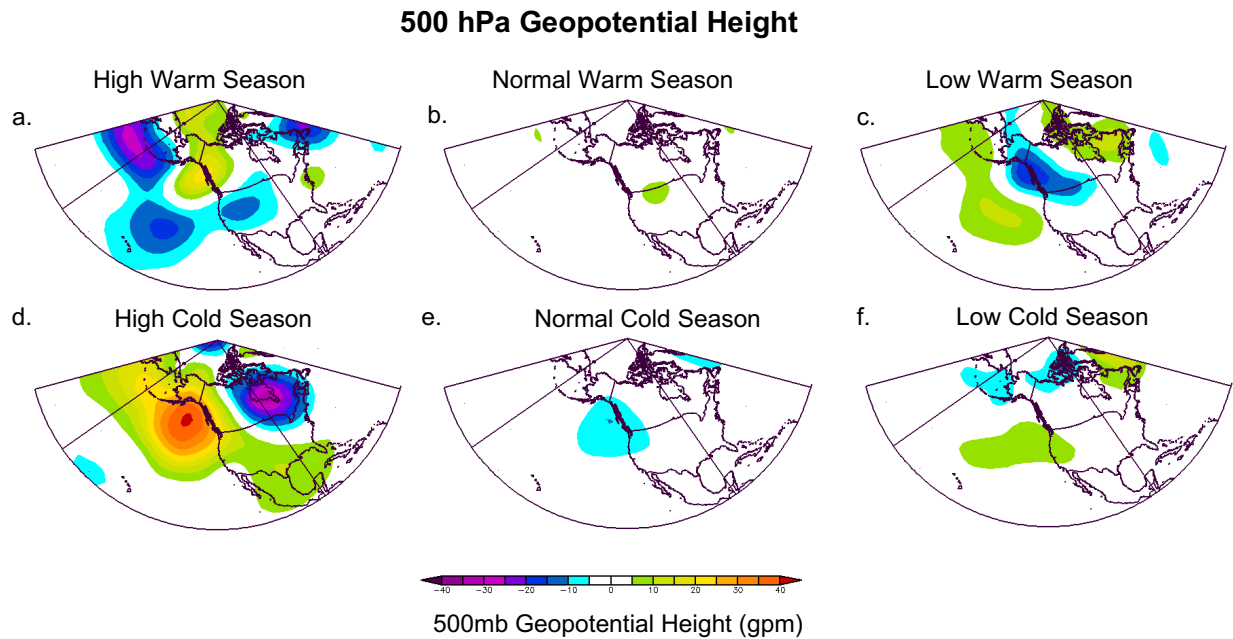
Figure 3.11 Seasonal Anomaly Composite: UKD Region δD vs. PNA Region 500 hPa Geopotential Height. Composites show 500 hPa geopotential height anomalies in the PNA region, in relation to the 1981 – 2010 climatological mean, for seasons with anomalous and normal hydrogen isotope ratios in the UKD region. Shading according to the color bar. Seasons included in each composite are those with (a) anomalously high warm season values, (b) normal warm season values, (c) anomalously low warm season values, (d) anomalously high cold season values, (e) normal cold season values, and (f) anomalously low cold season values in the Eclipse hydrogen isotope record.

3.3.6. Seasonal Relationships Between Eclipse Deuterium Excess and Broader PNA Region Climate

Because d-excess is commonly associated with the ocean temperature and humidity of the moisture source, I include SST composites instead of air temperature composites in this section and add composites of relative humidity (RH). Anomalously high d-excess warm seasons are characterized by a cold temperature anomaly (up to 0.6 °C below normal) in the tropical and subtropical Pacific and along the entire west coast of North America (Figure 3.12). Anomalously low d-excess warm seasons show a cold anomaly along the west coast of Canada, through the GOA region, and off the coast of western Alaska. Cold seasons with the highest d-excess values show a cold anomaly centered in the GOA, a

71

strong cold anomaly (>1.5 °C cooler than normal) in the high Arctic, and a warm anomaly (up to 0.75 °C warmer than normal) in the central Pacific. This pattern differs in anomalously low d-excess cold seasons, which display a strong warm anomaly throughout the Arctic Ocean and a weak cold anomaly of up to 0.3 °C below normal in the subtropical to tropical Pacific basin off the coast of North America.

Sea Surface Temperature

Sea Surface Temperature (°C)
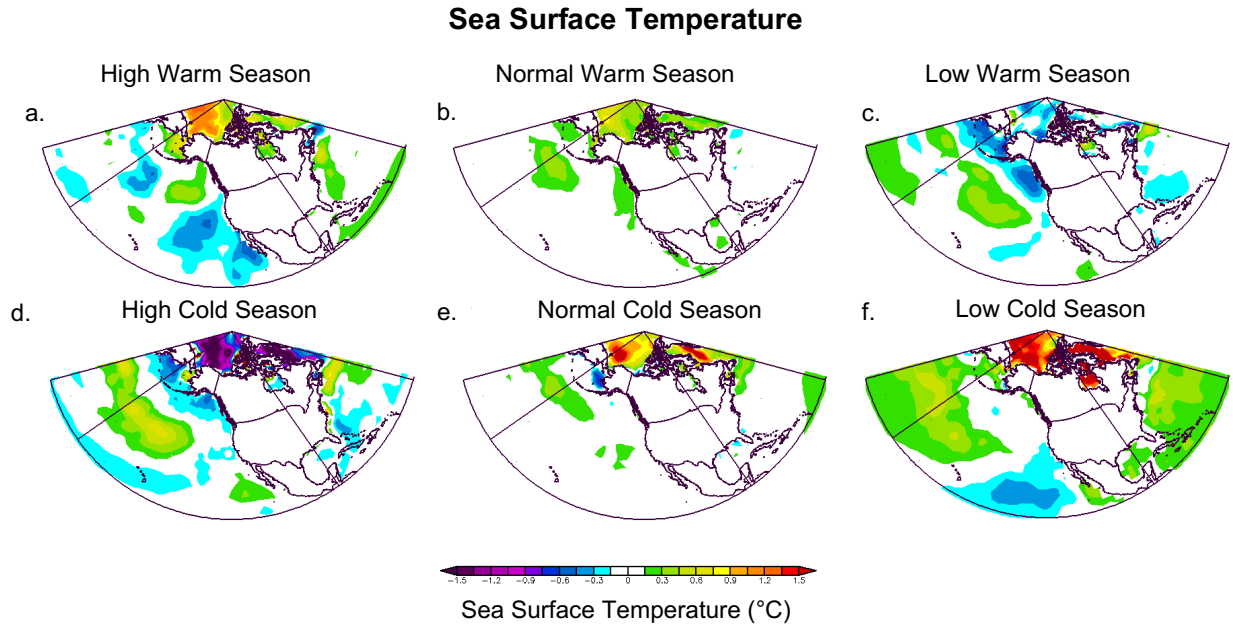
Figure 3.12 Seasonal Anomaly Composite: UKD Region Deuterium Excess vs. PNA Region Sea Surface Temperature. Composites show sea surface temperature anomalies in the PNA region, in relation to the 1981 – 2010 climatological mean, for seasons with anomalous and normal d-excess values in the UKD region. Shading according to the color bar. Seasons included in each composite are those with (a) anomalously high warm season values, (b) normal warm season values, (c) anomalously low warm season values, (d) anomalously high cold season values, (e) normal cold season values, and (f) anomalously low cold season values in the Eclipse d-excess record.

High cold seasons show a strong SLP anomaly of >2.5 hPa above normal in the southern GOA extending southwards into the subtropics (Figure 3.13). This feature is paired with a strong anomaly of up to 2.25 hPa below-normal SLP throughout north-central Canada and west of Alaska. Low warm seasons are characterized by a weak high SLP anomaly centered over the Aleutian Islands, paired with a weak low SLP anomaly in the central Pacific Ocean. Low cold seasons show a widespread area of high SLP anomalies up to 1.5 hPa above normal from the tropical Pacific to western Alaska.

Sea Level Pressure

High Warm Season	Normal Warm Season	Low Warm Season
a.	b.	c.

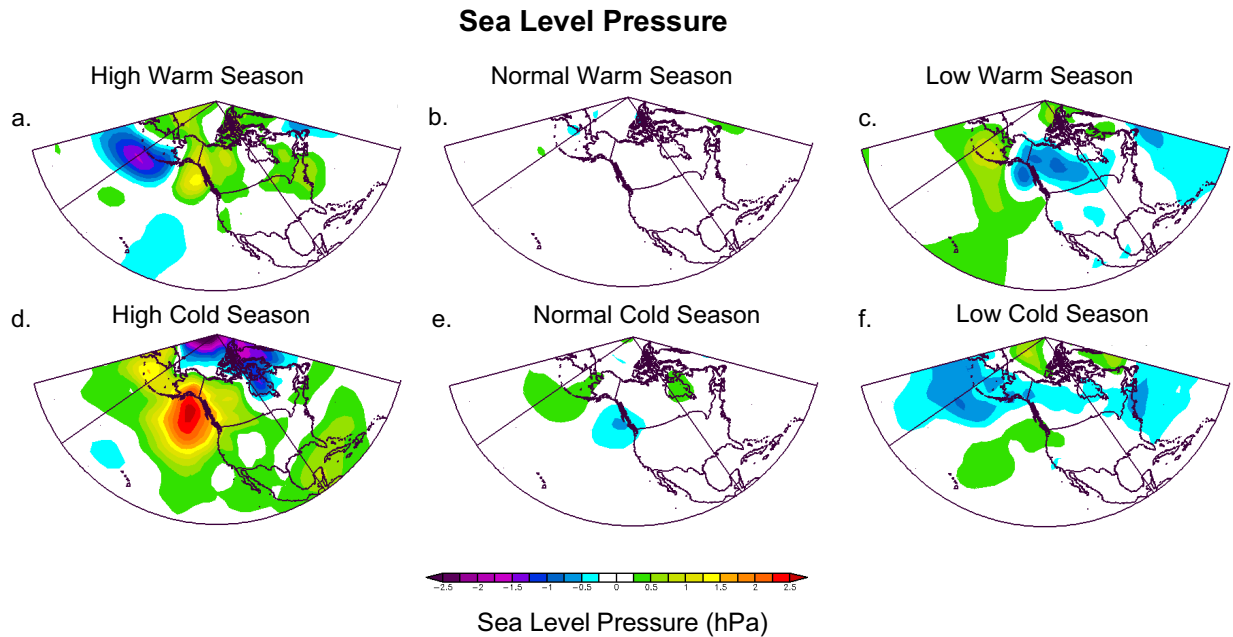| High Cold Season	Normal Cold Season	Low Cold Season
d.	e.	f.

Sea Level Pressure (hPa)
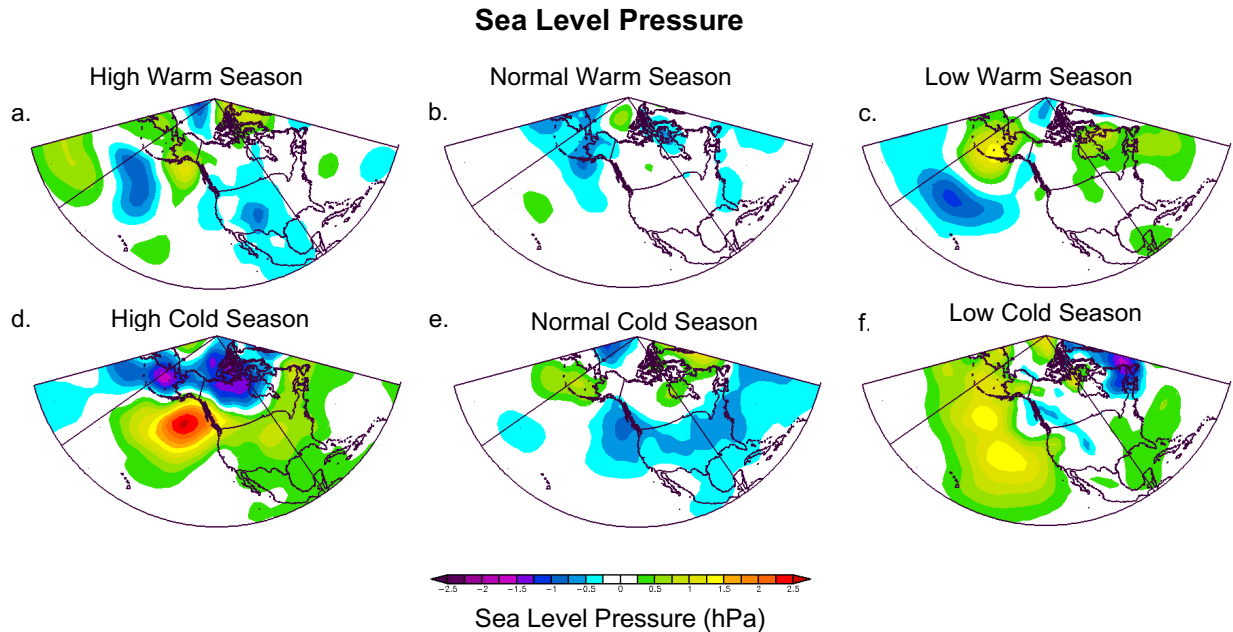
Figure 3.13 Seasonal Anomaly Composite: UKD Region Deuterium Excess vs. PNA Region Sea Level Pressure. Composites show sea level pressure anomalies in the PNA region, in relation to the 1981 – 2010 climatological mean, for seasons with anomalous and normal d-excess values in the UKD region. Shading according to the color bar. Seasons included in each composite are those with (a) anomalously high warm season values, (b) normal warm season values, (c) anomalously low warm season values, (d) anomalously high cold season values, (e) normal cold season values, and (f) anomalously low cold season values in the Eclipse d-excess record.

In the 500 hPa GPH composites, high cold seasons are characterized by a strong (up to 30 gpm below average) trough centered north of Alaska and extending through Alaska and northern Canada (Figure 3.14). This is paired with a ridge of up to 30 gpm above-average 500 hPa GPH south of the GOA. High warm seasons are associated with a ridge of up to 30 gpm above normal centered south of the GOA and extending to the north and south. Low warm seasons show anomalously low GPH (up to 20 gpm below normal) north and east of Alaska and a ridge over the Aleutian Islands equal in magnitude. Normal and low cold seasons do not show notable patterns.

With the exception of normal warm seasons, all RH composites show low RH anomalies in the southwestern United States (Figure 3.15). This feature is most pronounced in low cold seasons (>3.5% lower than normal). All seasonal groups are associated with anomalously low RH throughout Alaska and extending into northwestern Canada, with the exception of high cold seasons. The lowest RH in Alaska is

associated with low cold seasons: >3.5% below normal in south-central and northeastern Alaska. Low

cold seasons also show slightly higher-than-average RH south of the Aleutian Islands (up to 1% above

normal). Low warm seasons are associated with slightly above-average RH (up to 1% above normal) over

the subtropical Pacific Ocean.

500 hPa Geopotential Height

500mb Geopotential Height (gpm)
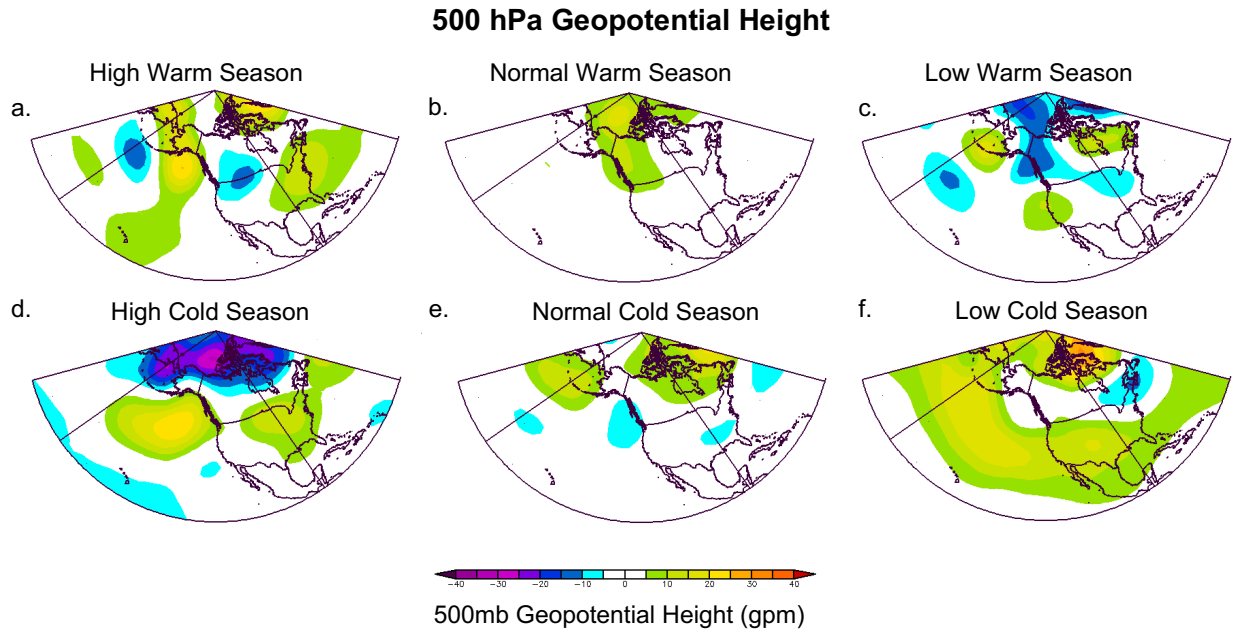
Figure 3.14 Seasonal Anomaly Composite: UKD Region Deuterium Excess vs. PNA Region 500 hPa Geopotential Height. Composites show 500 hPa geopotential height anomalies in the PNA region, in relation to the 1981 – 2010 climatological mean, for seasons with anomalous and normal d-excess values in the UKD region. Shading according to the color bar. Seasons included in each composite are those with (a) anomalously high warm season values, (b) normal warm season values, (c) anomalously low warm season values, (d) anomalously high cold season values, (e) normal cold season values, and (f) anomalously low cold season values in the Eclipse d-excess record.
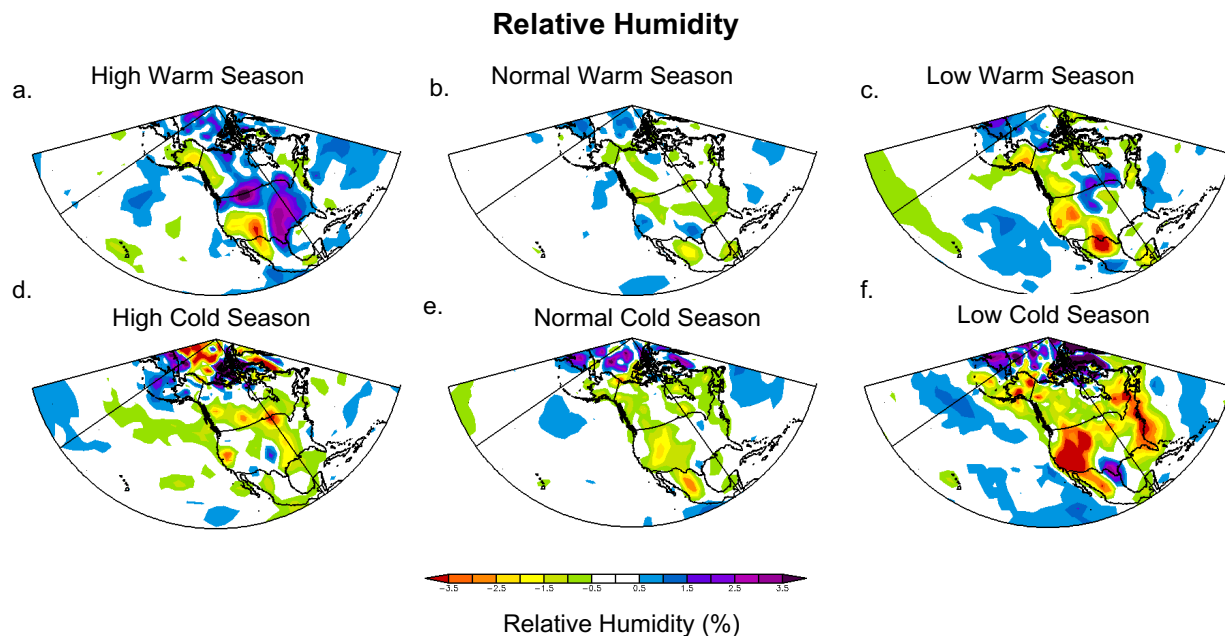
Relative Humidity

Figure 3.15 Seasonal Anomaly Composite: UKD Region Deuterium Excess vs. PNA Region Relative Humidity. Composites show relative humidity anomalies in the PNA region, in relation to the 1981 – 2010 climatological mean, for seasons with anomalous and normal d-excess values in the UKD region. Shading according to the color bar. Seasons included in each composite are those with (a) anomalously high warm season values, (b) normal warm season values, (c) anomalously low warm season values, (d) anomalously high cold season values, (e) normal cold season values, and (f) anomalously low cold season values in the Eclipse d-excess record.

3.3.7. Statistical Significance of Composite Anomaly Patterns in Broader PNA Region

I used a student's T-test to determine whether the mean of each climate variable (air temperature, SST, SLP, and GPH) within the region covering the GOA and Aleutian Islands (40 °N – 60 °N, 130 °W – 170 °W) during anomalous UKD seasons differed significantly ($p < 0.05$) from the seasonal mean over the entire NCEP/NCAR reanalysis timespan (1948 – 2016), or over the European Reanalysis (ERA)-Interim timespan (1979 – 2017; Berrisford et al. 2011) in the case of SST, which was not available for the NCEP/NCAR reanalysis. The mean air temperature in the GOA region during anomalously high and low warm seasons in the AWS temperature data differed significantly from the normal mean warm season temperature ($p = 3.4 \times 10^{-15}$ for high warm seasons, $p = 0.01$ for low warm seasons). The mean SLP in the GOA region during anomalously low cold seasons in the AWS temperature data was significantly higher than the

normal mean cold season SLP (p = 0.002), and the mean 500 hPa GPH during anomalously low warm

seasons in the AWS temperature data was significantly higher than the normal mean warm season 500

hPa GPH (p = 0.009). The means of other anomalous seasons of AWS temperature data, and of all

seasons of the anomalous isotope data (δD and d-excess) were not significantly different from the

normal regional mean. However, this outcome is likely due to the limited amount of datapoints in each

anomalous seasonal group (2 – 13 seasons per group), which lends few degrees of freedom to statistical

t-tests.

3.3.8. Relationships Between UKD Datasets and Climate Indices

The only significant relationship between *annually*-averaged UKD datasets and *annually*-

averaged climate indices occurred between UKD temperature and the PDO (r = 0.61, p = 0.02) (Figure

3.16). This relationship associates warmer temperatures with positive PDO conditions. Significant

relationships between *seasonally*-averaged UKD datasets and *seasonally*-averaged climate indices

occurred between UKD temperature and the PDO during the cold season (r = 0.70, p = 0.005), between

UKD temperature and the MEI during the cold season (r = 0.55, p = 0.04), and between UKD

temperature and Niño-3.4 during the cold season (r = 0.58, p = 0.03) (Figure 3.16). There were no

significant correlations between seasonally-averaged δD and d-excess and seasonally-averaged climate
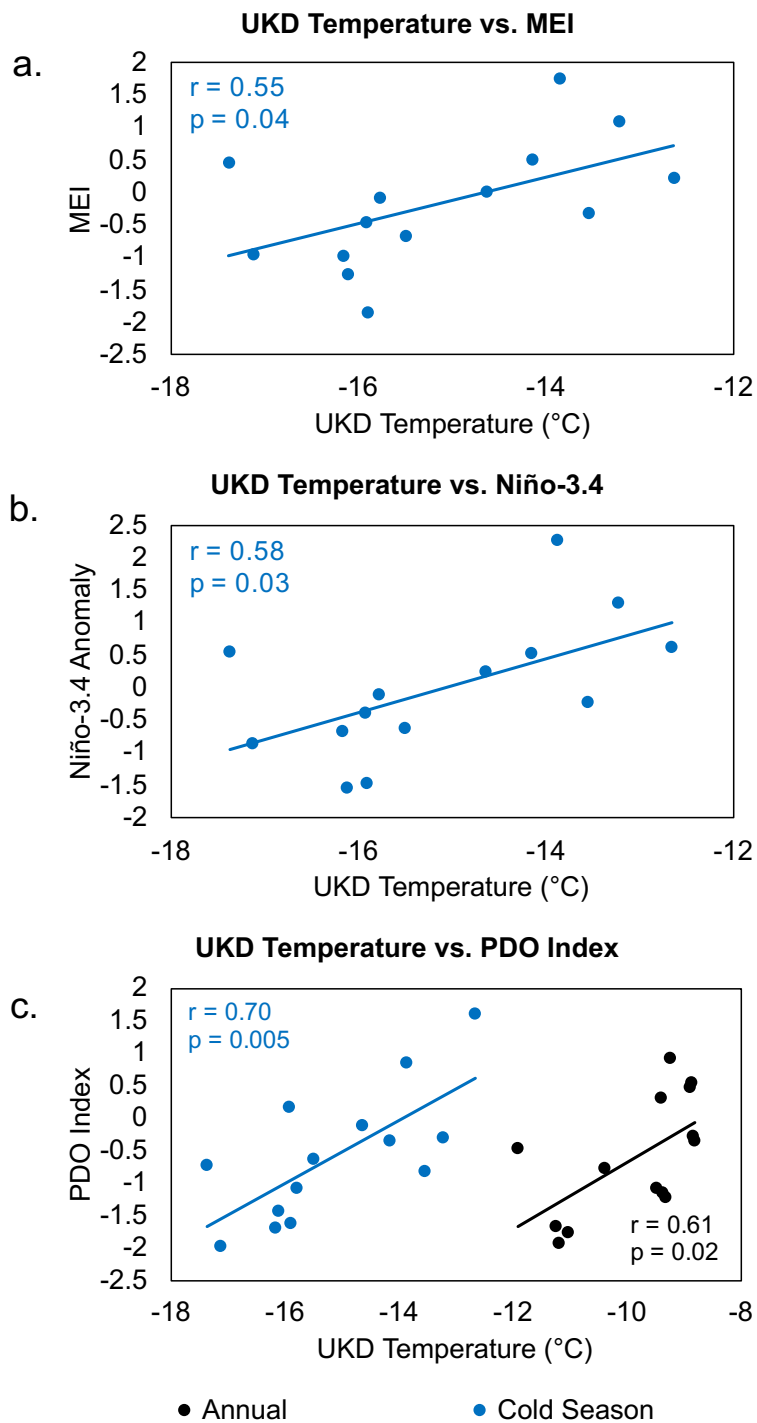
indices.

Figure 3.16 Relationships Between UKD Temperature and Climate Indices. UKD temperature versus: Multivariate ENSO Index during the cold season (a), Niño-3.4 anomaly during the cold season (b), and the Pacific Decadal Oscillation Index (c) (annual in black, cold season in blue). Correlation coefficients and p-values are noted next to scatter plots. All relationships cover the time frame from 2003 – 2016 and are based on annually- or seasonally-averaged data.

The only anomalous seasonal groupings with enough years to test significance between UKD data and climate indices were from the Eclipse δD record, which has the longest timescale overlap with climate index data. Of the high warm, high cold, low warm, and low cold seasons, the only significant relationships were found between high cold seasons versus the PDO (Figure 3.17). The highest-ratio cold seasons were significantly correlated with the PDO Index ($r = 0.60$, $p = 0.04$). The PDO Index is based upon SST measurements in the North Pacific region. Thus, correlations between cold seasons with anomalous isotope values versus SST in the GOA follow the same pattern as relationships between δD and the PDO index, although the anomaly patterns are not statistically significant. High cold seasons in the isotope record are weakly and insignificantly correlated with SSTs ($r = 0.25$, $p = 0.63$), while low cold seasons in the isotope record are insignificantly anticorrelated with SSTs ($r = -0.70$, $p = 0.08$). δD is significantly correlated with SSTs in the GOA on an annual timescale ($r = 0.56$, $p = 0.0003$), as seen in Figure 3.5.

In summary, relationships between UKD datasets and climate indices suggest that annual and cold-season UKD temperature, as well as δD during cold seasons with anomalously high isotope ratios, are indicative of PDO conditions. Because the PDO Index is a measure of SSTs in the North Pacific, this means that (1) UKD temperatures are representative of temperatures in the broader region, and (2) the process(es) driving regional temperatures are also a driver of isotope variability during high-ratio cold seasons. This makes sense considering the wintertime nature of the ALow, which is a known driver of temperatures in the GOA and surrounding region due to the increased southerly advection of warm air masses during its active phase. I have also shown the ALow to be a driver of isotope variability, as high-ratio cold seasons are associated with low SLP anomalies in the GOA—characteristic of a weaker-than-average ALow.

In addition to PDO conditions, cold season UKD temperatures are also significantly related ($p < 0.05$) to ENSO conditions, measured using the MEI and Niño-3.4 indices. This relationship demonstrates

78

the far-reaching atmospheric teleconnections driving temperature variability in the Pacific region, in which meteorological conditions in the tropics directly influence conditions in the North Pacific. A continued instrumental record of temperature at Divide may provide an increasingly valuable proxy for ENSO and PDO variability.

UKD δD vs. PDO Index
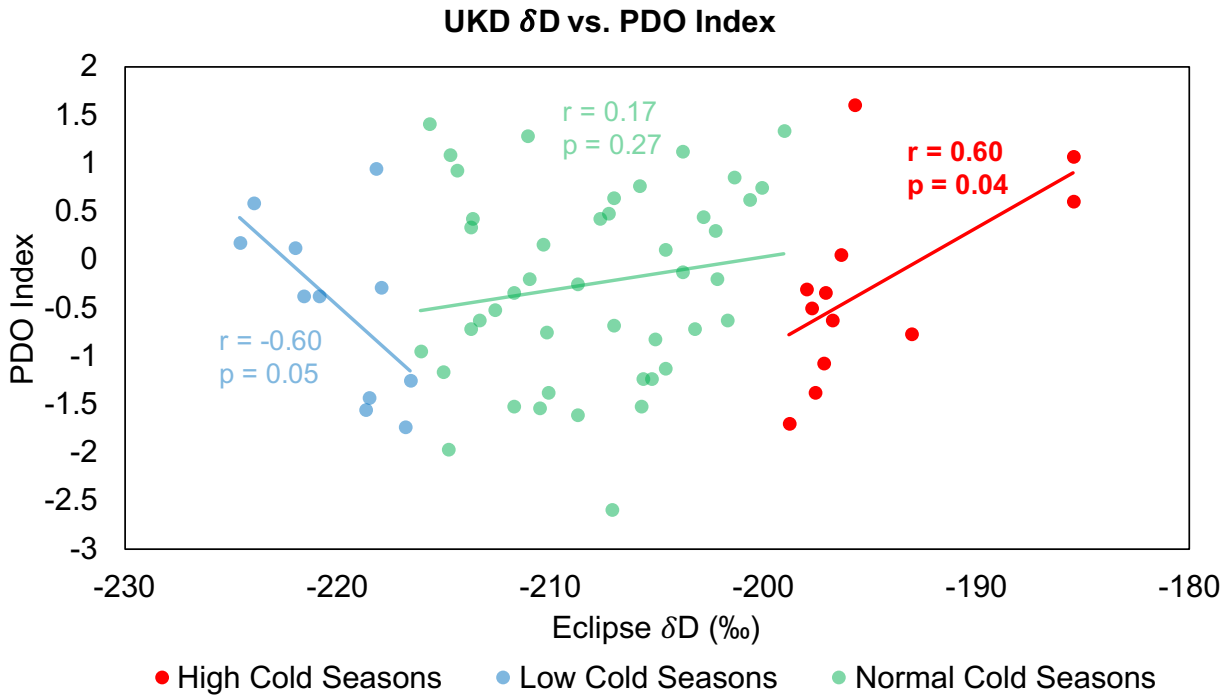
Figure 3.17 Significant Relationships Between UKD δD Values and the Pacific Decadal Oscillation Index. Eclipse low cold season δD versus low cold season PDOI values (blue), high cold season δD versus high cold season PDOI values (red), and normal cold season δD versus normal cold season PDOI values (green). Correlation coefficients and p-values are noted next to scatter plots, and significant correlations (high cold season) are bolded. Anomalous δD values were selected from seasonally-averaged data from 1948 – 2016.

3.4. Discussion

3.4.1. The UKD Region Ice Core Record vs. Local Climate Variability

I built on past work by Wake et al. (2002) and Kelsey et al. (2012) by comparing the Eclipse stable isotope record with a nearby weather station temperature dataset at Divide (~30 km away) rather than with distant weather station records from the broad surrounding region of Alaska and Canada. Despite the proximity of the instrumental dataset, I found weak, inconsistent relationships between the Eclipse

79

δD record and the Divide air temperature record on both annual and seasonal timescales, with only 2 –

15% of shared variance between the δD and temperature records (Figure 3.4). This is in agreement with

the findings of others, who found only 5 – 10% (Wake et al. 2002) and 18% (Kelsey et al. 2012) of shared

variance between Eclipse isotopes and regional temperatures.

In correlations of annually-averaged Divide temperature with annual mean air temperature, SLP,

and 500 hPa GPH in the North Pacific region, the temperature record shows strong and statistically

significant relationships with regional climate variability, indicating that temperatures in the UKD region

are representative of climate conditions in the broader region (Figure 3.5). The Eclipse isotope record

shows a similar, but weaker, spatial correlation pattern to the Divide station temperature dataset

(Figure 3.5). The significance of these correlations suggest that while local site temperature is not a

dominant factor controlling stable isotope variability at Eclipse on an annual timescale, temperature

patterns in the broader North Pacific region are representative of the atmospheric circulation patterns

that influence both regional temperature and Eclipse isotopes.

3.4.2. Seasonality in the UKD Temperature Record

Composites of regional climate anomalies associated with anomalous seasons in the Divide temperature

record support the conclusions of Kelsey et al. (2012) in that cold season UKD region conditions are

associated with stronger and more consistent climate anomaly patterns in the broader PNA region.

Anomalous temperatures at Divide correctly reflect anomalous regional temperatures: when it is colder

than average at Divide, it tends to be colder than average in the broader region as well, and similarly for

warm temperature anomalies (Figure 3.6).

In regional SLP composites, the ALow structure is apparent in cold seasons with anomalous

temperatures in the UKD region (Figure 3.7). The strongest observed ALow pattern is associated with

the warmest cold seasons, consistent with the increased advection of warm, moist air masses into the

GOA and surrounding landmass during strong ALow regimes, and with the wintertime nature of the

ALow pattern (Trenberth and Hurrell 1994, L'Heureux et al. 2004). I observed an anomalously weak

ALow pattern in SLP composites of the coldest cold seasons. In relation to climate indices, I found that

air temperature in the UKD region showed strong, significant correlations with the PDO Index (more so

in the cold season, but also annually), as well as with indices of ENSO variability (MEI and Niño-3.4)

during the cold season (Figure 3.16). Accumulation in the St. Elias Mountains, measured using a Mt.

Logan ice core, has also been found to be most strongly indicative of large-scale circulation during the

cold season: the accumulation timeseries shares variability with ENSO conditions in the tropical Pacific

on both interannual and interdecadal timescales (Holdsworth et al. 1992, Moore et al. 2002a, 2002b,

2005) and has been shown to be consistent with features of the PDO and PNA as well (Trenberth and

Hurrell 1994, Mantua and Hare 2002). These findings, along with my UKD temperature results,

demonstrate the interconnectedness of climate and atmospheric circulation throughout the Pacific

basin.

Anomalous cold seasons in the Divide temperature data also reflect consistent 500 hPa GPH

anomaly patterns in the regional composites (Figure 3.8). The trough (ridge) south of the GOA paired

with the ridge (trough) over Alaska and northwestern Canada in the warmest (coldest) cold seasons is

characteristic of the positive (negative) PNA pattern, although Divide temperature is not significantly

correlated with the PNA index during seasons with anomalous temperature. This is likely due to the

short timespan of the AWS dataset, which restricts the number of datapoints in anomalous seasonal

groups.

3.4.3. Seasonality in the Eclipse δD Record

Seasonality in the Eclipse δD record appears to match the seasonal distribution of temperatures in the

UKD region despite sharing, at most, only 15% of variability with UKD regional temperature on an annual

timescale (Figure 3.4). Composites of temperature anomalies in the PNA region during anomalous high-

and low-ratio seasons in the Eclipse δD record do not associate consistent regional temperature

patterns with any of the anomalous isotope groups (Figure 3.9). This is consistent with the observed

weak relationships between the Eclipse isotope record and local/regional temperature records on

seasonal timescales (described above, and outlined by Wake et al. 2002). The matched seasonality in

temperature and isotope records (Figure 3.3) may relate to seasonal features of atmospheric circulation,

as evidenced in composite maps of SLP (Figure 3.7) and 500 hPa GPH (Figure 3.8) anomalies during

seasons with anomalous isotopes. I found cold season anomaly composites to show the most consistent

atmospheric patterns during seasons with anomalous isotope values. This is in agreement with Kelsey et

al. (2012)'s association of cold season Eclipse isotopes with consistent atmospheric circulation patterns.

Similarly, Rupper et al. (2004) found the cold season in accumulation records from Mt. Logan to be the

most diagnostic of large-scale atmospheric circulation patterns.

In particular, I found the highest-ratio cold seasons to be associated with the most consistent

SLP and 500 hPa GPH anomalies in the PNA region. Anomalously high SLP and 500 hPa GPH centered in

the GOA are associated with high cold seasons in the Eclipse isotope record (Figures 3.7 and 3.8). These

pressure patterns are characteristic of the negative PNA pattern, which diverges from Kelsey et al.

(2012)'s association of the negative PNA pattern with the lowest-ratio cold seasons. This difference is

most likely due to a mismatch between chronologies, owing to my re-dating of the Eclipse 2002 core

since it was used for analysis by Kelsey et al. (2012). When interpreting precise meteorological data in

relation to isotope timeseries, a mis-match of even one year can lead to differing conclusions.

I found the Eclipse δD record to correlate with the PDO Index, but the correlation was only

significant during anomalously high-ratio cold seasons (Figure 3.17). The Eclipse δD record did not share

variability with indices of ENSO. The seasonality evident in the significance of correlations between UKD

region temperature and δD and broad-scale climate and atmospheric circulation suggests that cold

season records from the UKD region provide the most effective proxies for atmospheric circulation. This

82

result agrees with that of Kelsey et al. (2012), suggesting that strong cold season isotope-circulation relationships are a true characteristic of Eclipse isotope seasonality.

The long-term timeseries (1397 – 2017) of δD measured in Eclipse ice cores shows a weak (r = 0.04) yet significant (p = 0.006) positive relationship with time. However, only cold seasons with anomalously high isotope ratios showed significant relationships with indices of large-scale climate since 1948. Interpretations of the Eclipse isotope record over the entire 620-year timescale would benefit from a comparison of high-ratio cold seasons in the full composite record with proxy records of PDO and atmospheric variability in order to further test the significance of relationships between isotopes and climate variables with a larger dataset of anomalous seasons. High cold season isotope values may then be useful as a proxy for past variability in the PDO, PNA, and ALow, and to determine whether the positive relationship between Eclipse δD and time is due to industrial-age Arctic warming, trends in atmospheric circulation, or both.

3.4.4. Seasonality in the Eclipse Deuterium Excess Record

I found the most consistent regional climate anomalies to be associated with anomalous cold seasons in the d-excess time series, where high (low) d-excess cold seasons are associated with anomalously cold (warm) temperatures in the Arctic Ocean (Figure 3.12).

There exists a striking similarity between regional SLP (Figure 3.13) and 500 hPa GPH (Figure 3.14) anomaly composites in cold seasons with high δD and high d-excess values. Both high δD and high d-excess cold seasons are associated with a strong high SLP anomaly in the GOA, consistent with the negative PNA pattern, a weakened ALow, and a more zonal flow regime. 500 hPa GPH anomaly composites for warm season d-excess, and for normal and low d-excess cold seasons, do not show strong or consistent patterns (Figure 3.14), nor did these seasonal groups in the δD anomaly composites. This observation suggests that anomalously high δD and d-excess cold seasons may both result from zonal circulation, which is associated with local moisture sources. This pattern is consistent with isotope

fractionation theory in that an air mass traveling over a shorter distance experiences less fractionation, resulting in precipitation with higher isotope ratios. It is also consistent with Fisher et al. (2008)'s association of high isotope ratios with a weak ALow and a zonal moisture flow regime.

Low and inconsistent relationships between the Eclipse d-excess record and local temperature (Figure 3.4), as well as between the annually- and seasonally-averaged d-excess record and regional climate variables seem to support the conclusion of Fisher et al. (2004) that Eclipse d-excess is a poor tracer of moisture source during non-anomalous seasons; however, the coherence of d-excess and δD with consistent SLP and 500 hPa GPH patterns during anomalous cold seasons point to both variables' potential as a proxy for atmospheric circulation.

Relationships between d-excess and atmospheric circulation may change with time: the amplification of global warming in the Arctic has been associated with an increasing relevance of local contributions to atmospheric moisture due to the rapid decline in sea ice (Gimeno et al. 2019), which could result in a changing relationship between the Eclipse d-excess record and atmospheric circulation patterns as warming continues.

3.5. Conclusions

Addressing my first scientific question regarding the relationship between the Eclipse ice core stable isotope record and local temperature, I found all annually- and seasonally-averaged Eclipse δD and deuterium excess values to show weak and insignificant correlations with the Divide weather station temperature record over their timespan of overlap (2003 – 2016). This supports the conclusion of Wake et al. (2002) that Eclipse stable isotopes explain only a small fraction (5 – 10%) of temperature variability in the local region of Alaska and northwestern Canada. On an annual timescale, the Eclipse δD timeseries displays low yet significant (0.95 confidence level) relationships with mean air temperature, sea level pressure, and 500 hPa geopotential height in the broader PNA region, suggesting that temperature is one of various drivers of isotope variability in the Upper Kaskawulsh-Donjek region.

The timeseries of Divide temperatures reveals a distinct seasonality in its relationships with broader Pacific-North America region climate variability. The Divide weather station temperature record is representative of large-scale regional air temperature (r = 0.5 – 1.0 annually at the 0.95 confidence level), and it strongly reflects the influence of the ALow in modulating temperature in the GOA region, especially during the cold season. Temperature at Divide is also significantly correlated with indices of Pacific Decadal Oscillation variability annually (r = 0.61) and during the cold season (r = 0.70), and temperature is significantly related to measures of El Niño Southern Oscillation variability during the cold season as well (r = 0.58 and r = 0.55 for Divide temperature vs. Niño-3.4 and Multivariate ENSO Index, respectively).

The Eclipse δD record shows distinct seasonality, reflecting consistent atmospheric patterns in the cold season, as was shown by Kelsey et al. (2012). I found cold seasons with the highest δD ratios to be associated with the negative Pacific-North America pattern in composites of regional 500 hPa GPH and with a weak ALow in composites of regional SLP. The Eclipse d-excess record shows consistency with the δD record and the negative PNA pattern in cold seasons with anomalously high d-excess values, implicating zonal flow regimes as a mechanism facilitating high δD and d-excess values at Eclipse. This suggests that d-excess may be a better proxy for atmospheric circulation than has previously been posited by Fisher et al. (2004), who found no long-term relationships between d-excess and atmospheric circulation.

The extended timescale of overlap between the Eclipse ice core record and reanalysis products, the addition of local UKD region weather station data from Divide, and the addition of a complete Eclipse d-excess record from 1990 – 2016, allowed for more extensive analyses of relationships between isotopes and climate variability in the sub-Mt. Logan portion of the St. Elias Mountains than were possible in the past. In summary, I found that while local temperature does not control isotope fractionation at Eclipse, both local temperature and isotope variability are driven by temperature and

atmospheric circulation patterns in the broader Pacific region, particularly during the cold season.

Therefore, the shared seasonality between local temperature and stable isotopes in the UKD region is

due to seasonal patterns that drive moisture transport. This results in the observed relationship

between isotope variability and the degree to which moisture flow into the UKD region is zonal or

meridional—a relationship which may be examined on longer timescales further back in time in the

Eclipse isotope record. Further understanding of relationships between Eclipse isotopes and large-scale

climate variability will result from a longer Divide weather station record, longer overlaps between

Eclipse ice cores and reanalysis datasets, and reconciliation between Eclipse ice core chronologies.

CHAPTER 4

CONCLUSIONS AND FUTURE WORK

4.1. Summary of Findings

In this thesis, I examined some of the mechanisms driving ice core stable isotope variability in the Upper Kaskawulsh-Donjek region of the St. Elias Mountains in Yukon, Canada. In Chapter 2, I explored the effects of glacier surface melt on the amplitude of the isotope signal, focusing on a meteorological threshold of isotope signal preservation vs. alteration between Eclipse Icefield and Icefield Divide: two locations relatively close in space (~30 km) and elevation (~400 m difference). In this case study, an increase in mean summer temperature from ~-2 °C to ~-1 °C along the elevational transect from Eclipse down to Divide resulted in a marked loss of isotope signal preservation that prevented the Divide ice core record from being useful in comparisons with local meteorological data. Extending this analysis to the rest of the Arctic, I found mean summer temperatures of greater than approximately -1.5 °C to be associated with isotope signal alteration resulting from the downward percolation of meltwater through the snowpack. One notable exception to this trend was the ice core site at Combatant Col on Mt. Waddington in British Columbia, Canada (Neff et al. 2012), which experiences a relatively high mean annual temperature in comparison to other alpine ice core sites, yet retains ~75% of its original isotope signal amplitude over time. This is due to Mt. Waddington's high annual accumulation rate of nearly 7 m water-equivalent snowfall per year, which prevents meltwater from percolating throughout the annual layer.

Differences in the amounts of liquid water contained within the upper snowpack at Eclipse and Divide may also impact the spatial coherence of remotely-sensed land surface temperature records from the MODIS sensor, especially during the melt season when the snowpack at Divide contains more liquid water than the snowpack at Eclipse. I associate this observation with the fact that the MODIS land

surface temperature algorithm assumes spatially-consistent snow characteristics, even though differing

amounts of liquid water result in different surface reflectance values depending upon location.

In Chapter 3, I investigated relationships between the Eclipse stable isotope record and local

temperatures, regional climate variability, and climate indices. I found the stable isotope timeseries to

show weak and insignificant relationships with local temperatures measured at Divide, in agreement

with past work by Wake et al. (2002) and Kelsey et al. (2012), although it showed some significant

correlations with broader Pacific-North America regional temperature, sea level pressure, and mid-

troposphere height fields on an annual timescale. This suggests that regional temperature and

atmospheric conditions, rather than local conditions, play a role in modulating the Eclipse stable isotope

record. The stable isotope record was also significantly correlated with the Pacific Decadal Oscillation

Index during cold seasons with high isotope ratios ($p = 0.04$).

During cold seasons with anomalously high hydrogen isotope ratios and deuterium excess

values, composites of sea level pressure and 500 hPa geopotential height anomalies showed high

pressure fields in the Gulf of Alaska, indicative of a more zonal flow pattern during these anomalous

seasons. Zonal flow is associated with local moisture sources, suggesting that the seasonality observed

in Eclipse hydrogen isotope and deuterium excess records may reflect a seasonal pattern in atmospheric

circulation rather than in temperature. The significance of the cold season in reflecting consistent

atmospheric circulation patterns agrees with work by Kelsey et al. (2012).

4.2. Broader Implications and Significance

The preservation of the Eclipse isotope signal over time suggests that Eclipse contains a full Holocene

record of climate variability. This information is useful to those looking to select an alpine ice core site in

the North Pacific with a long climate record. However, the rapid warming trend in the Arctic at present

is unprecedented within the last 12,000 years and approaches a threshold such that the isotope record

at Eclipse, and at other Arctic sites with historically well-preserved isotope records, are likely to experience melt-related signal loss in the near future.

The prominence of the cold season in reflecting consistent atmospheric patterns in the Eclipse stable isotope record, as well as the coherence of atmospheric circulation patterns during cold seasons with anomalously high δD and deuterium excess values, suggests that the Eclipse isotope record may be a reliable proxy for cold season climate variability. Climate reconstructions using ice core records from the North Pacific are valuable in predicting how variables like temperature, precipitation, and storminess may respond to Arctic warming in populated regions, which allows for climate change adaptation. The relationship between Eclipse δD and the Pacific Decadal Oscillation (PDO) index is particularly relevant, as salmon populations respond to variability in North Pacific sea surface temperatures related to the PDO cycle. Looking further back in the Eclipse core record, high-ratio cold seasons may inform reconstructions of past Pacific-North America pattern and Aleutian Low Pressure System dynamics, as well as predictions of future salmon availability as temperatures in the Gulf of Alaska continue to warm.

4.3. Future Directions

In the future, I hope to examine high isotope ratio cold seasons further back in time in the Eclipse record, which extends back to approximately 1400 C.E. This analysis could provide a reliable record of variability in atmospheric circulation over time in the Pacific-North America region. In addition, adjusting the MODIS LST algorithm to account for spatial differences in snow type would benefit remotely-sensed temperature analyses in snow-covered regions.

BIBLIOGRAPHY

Abram, N. J., Mulvaney, R., Wolff, E. W., Triest, J., Kipfstuhl, S., Trusel, L. D., … Arrowsmith, C. (2013). Acceleration of snow melt in an Antarctic Peninsula ice core during the twentieth century. *Nature Geoscience*, *6*, 404–411.

Alexander, M. A., Bladé, I., Newman, M., Lanzante, J. R., Ngar-Cheung, L., & Scott, J. D. (2002). The atmospheric bridge: The influence of ENSO teleconnections on air-sea interaction over the global oceans. *Journal of Climate, 15,* 2205–2231.

Berrisford, P., Dee, D. P., Poli, P., Brugge, R., Fielding, M., Fuentes, M., Kållberg, P. W., Kobayashi, S., Uppsala, S., & Simmons, A. (2011). The ERA-Interim archive Version 2.0. *ERA Report Series, 1,* 1–23.

Bitz, C. M., & Battisti, D. S. (1999). Interannual to Decadal Variability in Climate and the Glacier Mass Balance in Washington, Western Canada, and Alaska. *Journal of Climate*, *12*(11), 3181–3196. https://doi.org/10.1175/1520-0442(1999)012<3181:ITDVIC>2.0.CO;2

Blackmon, M.L. (1976). A Climatological Spectral Study of the 500 mb Geopotential Height of the Northern Hemisphere. *Journal of the Atmospheric Sciences, 33*(8), 1607–1623.

Bunbury, J., & Gajewski, K. (2009). Postglacial climates inferred from a lake at treeline, southwest Yukon Territory, Canada. *Quaternary Science Reviews, 28*(3-4), 354–369. https://doi.org/10.1016/j.quascirev.2008.10.007

Campbell, S., Kreutz, K., Osterberg, E., Arcone, S., Wake, C., Introne, D., … Winski, D. (2012). Melt regimes, stratigraphy, flow dynamics and glaciochemistry of three glaciers in the Alaska Range. *Journal of Glaciology*, *58*(207), 99–109. https://doi.org/10.3189/2012JoG10J238

Cuffey, K. M., Clow, G. D., Alley, R. B., Stuiver, M., Waddington, E. D., & Saltus, R. W. (1995). Large arctic temperature change at the Wisconsin-Holocene glacial transition, *Science, 270*, 455–458.

Dansgaard, W. (1964). Stable isotopes in precipitation. *Tellus, 16*(4), 436–468. https://doi.org/10.3402/tellusa.v16i4.8993

Dansgaard, W., White, J. W., & Johnsen, S. J. (1989). The abrupt termination of the Younger Dryas climate event. *Nature, 339,* 532–534.

Deser, C., Phillips, A. S., & Hurrell, J. W. (2004). Pacific interdecadal climate variability: Linkages between the tropics and the North Pacific during boreal winter since 1990. *Journal of Climate, 17,* 3109–3124.

Divide, D., Isaksson, E., Martma, T., Meijer, H. A. J., Moore, J., Pohjola, V., van de Wal, R. S. W., & Godtliebsen, F. (2011). Thousand years of winter surface air temperature variations in Svalbard and Norway reconstructed from ice-core data. *Polar Research, 30(*1), 73–79. doi: 10.3402/polar.v30i0.7379

Field, R. D., Moore, G. W. K., Holdsworth, G., & Schmidt, G. A. (2010). A GCM-based analysis of circulation controls on δ^{18}O in the southwest Yukon, Canada: Implications for climate reconstructions in the region: CONTROLS ON δ^{18}O IN THE SW YUKON. *Geophysical Research Letters*, *37*(5), L05706. https://doi.org/10.1029/2009GL041408

Fisher, D.A. (1979). Comparison of 100,000 years of oxygen isotope and insoluble impurity profiles from the Devon Island and Camp Century ice cores. *Quaternary Research 11*, 299–304.

Fisher, D. A. (1991). Remarks on the deuterium excess in precipitation in cold regions, *Tellus*, *43B,* 401–407.

Fisher, D. A., Koerner, R. M., & Reeh, N. (1995). Holocene climatic records from Agassiz Ice Cap, Ellesmere Island, NWT, Canada. *The Holocene*, *5*(1), 19–24. https://doi.org/10.1177/095968369500500103

Fisher, D.A., et al. (2003). Penny Ice Cape Ice Core Data, IGBP PAGES/World Data Center for Paleoclimatology Data Contribution Series #2003-093. NOAA/NGDC Paleoclimatology Program, Boulder CO, USA.

Fisher, D. A., Wake, C., Kreutz, K., Yalcin, K., Steig, E., Mayewski, P., … Burns, S. J. (2004). Stable Isotope Records from Mount Logan, Eclipse Ice Cores and Nearby Jellybean Lake. Water Cycle of the North Pacific Over 2000 Years and Over Five Vertical Kilometres: Sudden Shifts and Tropical Connections. *Géographie Physique et Quaternaire*, *58*(2–3), 337. https://doi.org/10.7202/013147ar

Fisher, D., Osterberg, E., Dyke, A., Dahl-Jensen, D., Demuth, M., Zdanowicz, C., … Rupper, S. (2008). The Mt Logan Holocene—late Wisconsinan isotope record: tropical Pacific—Yukon connections. *The Holocene*, *18*(5), 667–677. https://doi.org/10.1177/0959683608092236

Fujii, Y., Kamiyama, K., Kawamura, T., Kameda, T., Izumi, I., Satow, K.,…Watanabe, O. (1990). 6000-Year Climate Records in an Ice Core from the Høghetta Ice Dome in Northern Spitsbergen. *Annals of Glaciology, 14,* 85–89.

Goto-Azuma, K., Koerner, R. M., Demuth, M. N., & Watanabe, O. (2006). Seasonal and spatial variations of snow chemistry on Mount Logan, Yukon, Canada. *Annals of Glaciology*, *43*, 177–186. https://doi.org/10.3189/172756406781812096

Grenfell, T.C., Perovich, D.K., & Ogren, J.A. (1981). Spectral albedos of an alpine snowpack. *Cold Regions Science and Technology, 4*(2), 121–127. https://doi.org/10.1016/0165-232X(81)90016-1

Grootes, P. M., Stuiver, M., White, J. W. C., Johnsen, S., Jouzel, J. (1993). Comparison of oxygen isotope records from the GISP2 and GRIP Greenland ice cores, *Nature, 366*(6455), 552–554, doi:10.1038/366552a0.

Grumet, N. S., Wake, C. P., Zielinski, G. A., Fisher, D., Koerner, R., & Jacobs, J. D. (1998). Preservation of glaciochemical time-series in snow and ice from the Penny Ice Cap, Baffin Island. *Geophysical Research Letters*, *25*(3), 357–360. https://doi.org/10.1029/97GL03787

Guan, J., Liu, Z., Wen, X., Brady, E., Noone, D., Zhu, J., & Han, J. (2016). Understanding the temporal slope of the temperature-water isotope relation during the deglaciation using isoCAM3: The slope equation, *J. Geophys. Res. Atmos., 121*, 10,342–10,354, doi:10.1002/ 2016JD024955.

Harada, Y., Kamahori, H., Kobayashi, C., Endo, H., Kobayashi, S., Ota, Y., … Takahashi, K. (2016). The JRA-55 Reanalysis: Representation of Atmospheric Circulation and Climate Variability. *Journal of the Meteorological Society of Japan. Ser. II*, *94*(3), 269–302. https://doi.org/10.2151/jmsj.2016-015

Harris, I., Jones, P. D., Osborn, T. J., & Lister, D. H. (2014). Updated high-resolution grids of monthly climatic observations - the CRU TS3.10 Dataset. *Int. J. Climatol.*, *34*, 623–642. doi: 10.1002/joc.3711

Hartmann, B., & Wendler, G. (2005). The Significance of the 1976 Pacific Climate Shift in the Climatology of Alaska. *Journal of Climate*, *18*(22), 4824–4839. https://doi.org/10.1175/JCLI3532.1

Higgins, R. W., Leetmaa, A., Xue, Y., & Barnston, A. (2000). Dominant factors influencing the seasonal predictability of U.S. precipitation and surface air temperature. *J. Climate, 13*, 3994–4017.

Holdsworth, G., Fogarasi, S., & Krouse, H. R. (1991). Variation of the stable isotopes of water with altitude in the Saint Elias Mountains of Canada. *Journal of Geophysical Research: Atmospheres*, *96*(D4), 7483–7494. https://doi.org/10.1029/91JD00048

Holdsworth, G. H., H. R. Krouse, & M. Nosal (1992). Ice core climate signals from Mount Logan Yukon A.D. 1700-1987. *Climate Since A.D. 1500*, R. S. Bradley and P. D. Jones, Eds., Routledge, 483–504.

Johnsen, S. J., Dansgaard, W., & White J. W. (1989). The origin of Arctic precipitation under present and glacial conditions, *Tellus, 41*, 452–469.

Jouzel, J., L. Merlivat, & C. Lorius (1982). Deuterium excess in an east Antarctic ice core suggests higher relative humidity at the oceanic surface during the last glacial maximum , *Nature, 299*, 688–691.

Jouzel, J., Merlivat, L., Petit, J. R., & Lorius, C. (1983). Climatic information over the last century deduced from a detailed isotopic record in the South Pole snow. *J. Geophys. Res., 88*, 2693–2703.

Jouzel, J., Alley, R. B., Cuffey, K. M., Dansgaard, W., Grootes, P., Hoffmann, G., … White, J. (1997). Validity of the temperature reconstruction from water isotopes in ice cores. *Journal of Geophysical Research: Oceans*, *102*(C12), 26471–26487. https://doi.org/10.1029/97JC01283

Kalnay, E., Kanamitsu, M., Kistler, R., Collins, W., Deaven, D., Gandin, L., … Joseph, D. (1996). The NCEP/NCAR 40-year reanalysis project, *Bull. Amer. Meteor. Soc., 77*, 437–470.

Kelsey, E. P., Wake, C. P., Kreutz, K., & Osterberg, E. (2010). Ice layers as an indicator of summer warmth and atmospheric blocking in Alaska. *Journal of Glaciology*, *56*(198), 715–722. https://doi.org/10.3189/002214310793146214

Kelsey, E. P., Wake, C. P., Yalcin, K., & Kreutz, K. (2012). Eclipse Ice Core Accumulation and Stable Isotope Variability as an Indicator of North Pacific Climate. *Journal of Climate*, *25*(18), 6426–6440. https://doi.org/10.1175/JCLI-D-11-00389.1

Koerner, R. M. & Fisher, D. A. (1990). A record of Holocene summer climate from a Canadian high-Arctic ice core. *Nature, 343,* 630–631.

Koerner, R.M. (1997). Some comments on climatic reconstructions from ice core drilled in areas of high melt. *Journal of Glaciology, 43*(143), 90–97.

Kreutz, K. J., Wake, C. P., & Yalcin, K. (2004). Signal-to-noise ratios and climate records from the Eclipse Icefield ice cores. *EOS Transactions, American Geophysical Union, 85*(47), Fall Meeting Supplement, Abstract PP21A-1346.

Krinner, G., Genthon, C. & Jouzel, J. (1997), GCM analysis of local influences on ice core δ signals, *Geophys. Res. Lett., 24*, 2825–2828, doi:10.1029/97GL52891.

Kuipers Munneke, P., Ligtenberg, S. R. M., Broeke, M. R., Angelen, J. H., & Forster, R. R. (2014). Explaining the presence of perennial liquid water bodies in the firn of the Greenland Ice Sheet, *Geophys. Res. Lett., 41,* 476–483, https://doi.org/10.1002/2013GL058389

L'Heureux, M. L., Mann, M. E., Cook, B. I., Gleason, B. E. & Vose, R. S. (2004). Atmospheric circulation influences on seasonal precipitation patterns in Alaska during the latter 20th century. *J. Geophys. Res.-Atmos. 109,* 17, https://doi.org/10.1029/2003jd003845

Mair, D., Burgess, D., & Sharp, M. (2005). Thirty-seven year mass balance of Devon Ice Cap, Nunavut, Canada, determined by shallow ice coring and melt modeling. *Journal of Geophysical Research*, *110*(F1), F01011. https://doi.org/10.1029/2003JF000099

Mantua, N. J., Hare, S. R., Zhang, Y., Wallace, J. M., & Francis, R. C. (1997). A Pacific interdecadal climate oscillation with impacts on salmon production. *Bulletin of the American Meteorological Society*, *78*(6), 1069–1079. https://doi.org/10.1175/1520-0477(1997)078<1069:APICOW>2.0.CO;2

Mantua, N. J., & Hare, S. R. (2002). The Pacific Decadal Oscillation. *Journal of Oceanography, 58,* 35–44. http://dx.doi.org/10.1023/A:1015820616384

McFarlane, G. A., & Beamish, R. J. (1992). Climatic Influence Linking Copepod Production with Strong Year-Classes in Sablefish, Anoplopoma fimbria. *Canadian Journal of Fisheries and Aquatic Sciences*, *49*(4), 743–753. https://doi.org/10.1139/f92-083

Merlivat, L. & Jouzel, J. (1979). Global climatic interpretation of the deuterium-oxygen 18 relationship for precipitation. *Journal of Geophysical Research, 84*(C8) : 5029–5033.

Meyer, C. R., & Hewitt, I. J. (2017). A continuum model for meltwater flow through compacting snow. *The Cryosphere*, *11*(6), 2799–2813. https://doi.org/10.5194/tc-11-2799-2017

Mingo, L., & Flowers, G. E. (2010). An integrated lightweight ice-penetrating radar system. *Journal of Glaciology*, *56*(198), 709–714. https://doi.org/10.3189/002214310793146179

Mo, K. C. & Higgins, R. W. (1996). Large-Scale Atmospheric Moisture Transport as Evaluated in the NCEP/NCAR and the NASA/DAO Reanalyses. *J. Climate, 9,* 1531–1545.

Moore, G. W. K., Holdsworth, G., & Alverson, K. (2001). Extra-tropical response to ENSO as expressed in an ice core from the Saint Elias Mountain Range. *Geophysical Research Letters*, *28*(18), 3457–3460. https://doi.org/10.1029/2000GL012397

Moore, G. W. K., Alverson, K., & Holdsworth, G. (2002a). Variability in the climate of the Pacific Ocean and North America as expressed in the Mount Logan ice core. *Annals of Glaciology*, *35*, 423–429. https://doi.org/10.3189/172756402781817185

Moore, G. W. K., Holdsworth, G., & Alverson, K. (2002b). Climate change in the North Pacific region over the past three centuries. *Nature*, *420*(6913), 401–403. https://doi.org/10.1038/nature01229

Moore, G. W. K., Alverson, K., & Holdsworth, G. (2003). The Impact that Elevation has on the ENSO Signal in Precipitation Records from the Gulf of Alaska Region. In H. F. Diaz (Ed.), *Climate Variability and Change in High Elevation Regions: Past, Present & Future* (Vol. 15, pp. 101–121). https://doi.org/10.1007/978-94-015-1252-7_6

Moore, G. W. K., Alverson, K., & Holdsworth, G. (2005). Mount Logan ice core evidence for changes in the Hadley and Walker circulations following the end of the Little Ice Age. In: Diaz, H. F., and Bradley, R.S., eds. The Hadley Circulation: Present, past, and future. Advances in Global Change Research 21. Dordrecht, The Netherlands: Kluwer. 371–395.

Moran, T., & Marshall, S. (2009). The effects of meltwater percolation on the seasonal isotopic signals in an Arctic snowpack. *Journal of Glaciology*, *55*(194), 1012–1024. https://doi.org/10.3189/002214309790794896

Moran, T., Marshall, S. J., & Sharp, M. J. (2011). Isotope thermometry in melt-affected ice cores: ISOTOPE THERMOMETRY. *Journal of Geophysical Research: Earth Surface*, *116*(F2). https://doi.org/10.1029/2010JF001738

Neff, P. D., Steig, E. J., Clark, D. H., McConnell, J. R., Pettit, E. C., & Menounos, B. (2012). Ice-core net snow accumulation and seasonal snow chemistry at a temperate-glacier site: Mount Waddington, southwest British Columbia, Canada. *Journal of Glaciology*, *58*(212), 1165–1175. https://doi.org/10.3189/2012JoG12J078

Ochwat, N. (2019). Firn Characterization of the Accumulation Zone of Kaskawulsh Glacier, Yukon Territory, Canada. *University of Calgary: Thesis Submitted to the Faculty of Graduate Studies in Partial Fulfilment of the Requirements for the Degree of Master of Science,* 1–130.

Ohmura, A. (2000). Physical Basis for the Temperature-Based Melt-Index Method. *Journal of Applied Meteorology*, *40*, 753–761.

Orlanski, I. (2005). A new look at the Pacific storm track variability: Sensitivity to tropical SSTs and to upstream seeding. *Journal of Atmospheric Sciences, 62*, 1367 – 1390. https://doi.org/10.1175/JAS3428.1

Osterberg, E. C., Mayewski, P. A., Fisher, D. A., Kreutz, K. J., Maasch, K. A., Sneed, S. B., & Kelsey, E. (2014). Mount Logan ice core record of tropical and solar influences on Aleutian Low variability: 500–1998 A.D. *Journal of Geophysical Research: Atmospheres*, *119*(19), 11,189–11,204. https://doi.org/10.1002/2014JD021847

Pepin, N. C., & Seidel, D. J. (2005). A global comparison of surface and free-air temperatures at high elevations. *Journal of Geophysical Research: Atmospheres, 110*.

Pfahl, S. & Sodemann, H. (2014). What controls deuterium excess in global precipitation? *Clim. Past, 10*, 771–781. doi:10.5194/cp-10-771-2014

Pohjola, V. A., Moore, J. C., Isaksson, E., Jauhiainen, T., van de Wal, R. S. W., Martma, T., Meijer, H. A. J., & Vaikmäe, R. (2002). Effect of periodic melting on geochemical and isotopic signals in an ice core from Lomonosovfonna, Svalbard. *Journal of Geophysical Research*, *107*(D4), 4036. https://doi.org/10.1029/2000JD000149

Porter, T. J., Schoenemann, S. W., Davies, L. J., Steig, E. J., Bandara, S., & Froese, D. G. (2019). Recent summer warming in northwestern Canada exceeds the Holocene thermal maximum. *Nature Communications*, *10*(1), 1631. https://doi.org/10.1038/s41467-019-09622-y

Pu, Z., Xu, L., & Salomonson, V. V. (2007). MODIS/Terra observed seasonal variations of snow cover over the Tibetan Plateau. *Geophysical Research Letters*, *34*(6). https://doi.org/10.1029/2007GL029262

Rodionov, S. N., Overland, J. E., & Bond, N. A. (2005). Spatial and temporal variability of the Aleutian climate. *Fisheries Oceanography*, *14*, 3–21. https://doi.org/10.1111/j.1365-2419.2005.00363.x

Rupper, S., Steig, E. J., & Roe, G. (2004). The Relationship between Snow Accumulation at Mt. Logan, Yukon, Canada, and Climate Variability in the North Pacific. *Journal of Climate*, *17*(24), 4724–4739. https://doi.org/10.1175/JCLI-3202.1

Saravanan, R. (1998). Atmospheric low-frequency variability and its relationship to midlatitude SST variability: Studies using the NCEP/NCAR Climate System Model. *Journal of Climate, 11*(6), 1386–1404.

Shuman, C. A., Alley, R. B., Anandakrishnan, S., White, J. W. C., Grootes, P. M., & Stearns, C. R. (1995). Temperature and accumulation at the Greenland Summit: Comparison of high-resolution isotope profiles and satellite passive microwave brightness temperature trends. *J. Geophys. Res., 100,* 9165–9177.

Steger, C. R., Reijmer, C. H., & van den Broeke, M. R. (2017). The modelled liquid water balance of the Greenland Ice Sheet. *The Cryosphere, 11*, 2507–2526, https://doi.org/10.5194/tc-11-2507–2017

Steig, E. J., Grootes, P. M., & Stuiver, M. (1994). Seasonal precipitation timing and ice core records. *Science, 266,* 1885–1886.

Taylor, S., Feng, X., Kirchner, J. W., Osterhuber, R., Klaue, B., & Renshaw, C. E. (2001). Isotopic evolution of a seasonal snowpack and its melt. *Water Resources Research*, *37*(3), 759–769. https://doi.org/10.1029/2000WR900341

Trenberth, K. E., & Hurrell, J. W. (1994). Decadal atmosphere-ocean variations in the Pacific. *Climate Dynamics, 9*, 303–319.

Trenberth, K. E. (1997). The definition of El Niño. *Bull. Amer. Meteor. Soc., 78,* 2771–2777.

Venrick, E. L., Mcgowan, J. A., Cayan, D. R., & Hayward, T. L. (1987). Climate and Chlorophyll a: Long-Term Trends in the Central North Pacific Ocean. *Science*, *238*(4823), 70–72. https://doi.org/10.1126/science.238.4823.70

Wake, C. P., Yalcin, K., & Gundestrup, N. S. (2002). The climate signal recorded in the oxygen-isotope, accumulation and major-ion time series from the Eclipse ice core, Yukon Territory, Canada. *Annals of Glaciology*, *35*, 416–422. https://doi.org/10.3189/172756402781817266

Wallace, J. M., & D. S. Gutzler (1981). Teleconnections in the geopotential height field during the Northern Hemisphere Winter. *Mon. Wea. Rev., 109*, 784–812.

Wan, Z. (2008). New refinements and validation of the MODIS Land-Surface Temperature/Emissivity products. *Remote Sensing of Environment*, *112*(1), 59–74. https://doi.org/10.1016/j.rse.2006.06.026

Wan, Z. (2014). New refinements and validation of the collection-6 MODIS land-surface temperature/emissivity product. *Remote Sensing of Environment*, *140*, 36–45. https://doi.org/10.1016/j.rse.2013.08.027

Werner, M., Mikolajewicz, U., Heimann, M., & Hoffmann, G. (2000). Borehole versus isotope temperatures on Greenland: Seasonality does matter, *Geophys. Res. Lett., 27*, 723–726, doi:10.1029/1999GL006075.

Westermann, S., Langer, M., & Boike, J. (2012). Systematic bias of average wintertime land surface temperatures inferred from MODIS at a site on Svalbard, Norway. *Remote Sensing of Environment, 118,* 162–167. https://doi.org/10.1016/j.rse.2011.10.025

Wiles, G. C., D'Arrigo, R. D., Villalba, R., Calkin, P. E., & Barclay, D. J. (2004). Century-scale solar variability and Alaskan temperature change over the past millennium. *Geophys. Res. Lett., 31,* L15203.http://dx.d0i.0rg/l 0.1029/2004GL0200

Williamson, S. N., Hik, D. S., Gamon, J. A., Jarosch, A. H., Anslow, F. S., Clarke, G. K. C., & Scott Rupp, T. (2017). Spring and summer monthly MODIS LST is inherently biased compared to air temperature in snow covered sub-Arctic mountains. *Remote Sensing of Environment*, *189*, 14–24. https://doi.org/10.1016/j.rse.2016.11.009

Williamson, S. N., Zdanowicz, C., Anslow, F. S., Clarke, G. K. C., Copland, L., Danby, R. K., Flowers, G. E., Holdsworth, G., Jarosch, A. H., & Hik, D. S. (in review). Amplified warming in the St. Elias Mountains, Alaska/Yukon, is regulated by the upper Troposphere (manuscript JCLI-D-19-0405).

Winski, D., Kreutz, K., Osterberg, E., Campbell, S., & Wake, C. (2012). High-frequency observations of melt effects on snowpack stratigraphy, Kahiltna Glacier, Central Alaska Range. *Hydrological Processes*, *26*(17), 2573–2582. https://doi.org/10.1002/hyp.9348

Winski, D., Osterberg, E., Ferris, D., Kreutz, K., Wake, C., Campbell, S., … Handley, M. (2017). Industrial-age doubling of snow accumulation in the Alaska Range linked to tropical ocean warming. *Scientific Reports*, *7*(1), 17869. https://doi.org/10.1038/s41598-017-18022-5

Winski, D., Osterberg, E., Kreutz, K., Wake, C., Ferris, D., Campbell, S., Baum, M., Bailey, A., Birkel, S., Introne, D., & Handley, M. (2018). A 400-Year Ice Core Melt Layer Record of Summertime Warming in the Alaska Range. *JGR Atmospheres, 123*(7), 3594–3611. https://doi.org/10.1002/2017JD027539

Wolter, K., & Timlin, M. S. (1993). Monitoring ENSO in COADS with a seasonally adjusted principal component index. *Proc. 17th Climate Diagnostics Workshop,* Norman, OK, NOAA*, 52–57.

Wolter, K., & Timlin, M. S., (1998). Measuring the strength of ENSO events—How does 1997/98 rank? *Weather, 53*, 315–324.

Yalcin, K., & Wake, C. P. (2001). Anthropogenic signals recorded in an ice core from Eclipse Icefield, Yukon Territory, Canada. *Geophysical Research Letters*, *28*(23), 4487–4490. https://doi.org/10.1029/2001GL013037

Yalcin, K., Wake, C. P., Kreutz, K. J., & Whitlow, S. I. (2006). A 1000-yr record of forest fire activity from Eclipse Icefield, Yukon, Canada. *The Holocene, 16*(2), 200–209. https://doi.org/0.1191/0959683606hl920rp

Yalcin, K., Wake, C. P., Kreutz, K. J., Germani, M. S., & Whitlow, S. I. (2007). Ice core paleovolcanic records from the St. Elias Mountains, Yukon, Canada. *Journal of Geophysical Research*, *112*(D8). https://doi.org/10.1029/2006JD007497

Yasunari, T. J., Shiraiwa, T., Kanamori, S., Fujii, Y., Igarashi, M., Yamazaki, K., … Hondoh, T. (2007). Intra-annual variations in atmospheric dust and tritium in the North Pacific region detected from an ice core from Mount Wrangell, Alaska: INTRA-ANNUAL DUST AND TRITIUM VARIATIONS. *Journal of Geophysical Research: Atmospheres*, *112*(D10). https://doi.org/10.1029/2006JD008121

Youngblut, D., & Luckman, B. (2008). Maximum June-July temperatures in the southwest Yukon over the last 300 years reconstructed from tree-rings. *Dendrochronologia, 25*(3), 153–166. http://dx.doi.Org/10.1016/j.dendro.2006.ll.004

Zdanowicz, C., Fisher, D., Bourgeois, J., Demuth, M., Zheng, J., Mayewski, P., … Goto-Azuma, K. (2014). Ice Cores from the St. Elias Mountains, Yukon, Canada: Their Significance for Climate, Atmospheric Composition and Volcanism in the North Pacific Region. *Arctic*, *67*, 35–57.

Zdanowicz, C., Copland, L., *et al.* (in prep.) Surface climatological observations in the St.Elias Mountains, Yukon, Canada, from automated weather stations, 2000–2018.

Zhang, Y., Wallace, J. M., & Battisti, D. S. (1997). ENSO-like interdecadal variability: 1900–93. *J. Climate, 10,* 1004–1020.

APPENDIX A: SUPPLEMENTARY INFORMATION

Table A.1 Acronyms and Abbreviations Used in Thesis

Acronym/Abbreviation	Meaning
ALow	Aleutian Low Pressure System
AO	Arctic Oscillation
ASL	Above Sea Level
AWS	Automated Weather Station
BP	Before Present
d-excess	Deuterium Excess
D/H	Deuterium/Hydrogen
DIC	Devon Ice Cap
Divide	Icefield Divide
Eclipse	Eclipse Icefield
ENSO	El Niño Southern Oscillation
EOF	Empirical Orthogonal Function
ERA	European Reanalysis
ESRL	Earth System Research Laboratory
GCM	General Circulation Model
GOA	Gulf of Alaska
GPH	Geopotential Height
GPR	Ground-Penetrating Radar
GSSI	Geophysical Survey Systems Incorporated
HTM	Holocene Thermal Maximum
JJA	June-July-August
KBC	Kahiltna Base Camp
LGM	Last Glacial Maximum
LMWL	Local Meteoric Water Line
LST	Land Surface Temperature
MEI	Multivariate El Niño Southern Oscillation Index
MODIS	Moderate Resolution Imaging Spectroradiometer
MP	Melt Percentage
NASA	National Aeronautics and Space Administration
NCAR	National Center for Atmospheric Research
NCEP	National Centers for Environmental Prediction
NCEP/NCAR V1	NCEP/NCAR Reanalysis Version 1
NOAA	National Oceanic and Atmospheric Administration
NPI	North Pacific Index
NW Col	Northwest Col
$^{18}O/^{16}O$	Oxygen-18/Oxygen-16
PDD	Positive Degree Day
PDO	Pacific Decadal Oscillation
PIC	Penny Ice Cap
PNA	Pacific-North America Pattern
PR Col	Prospector Russell Col

Table A.1 Continued.

RH	Relative Humidity
SLP	Sea Level Pressure
SST	Sea Surface Temperature
TWTT	Two-Way Travel Time
UEA CRU	University of East Anglia Climate Research Unit
UKD	Upper Kaskawulsh-Donjek
UYG	Upper Yentna Glacier
V-SMOW	Vienna-Standard Mean Ocean Water
w.e.	Water-Equivalent

BIOGRAPHY OF THE AUTHOR

Erin McConnell was born in Syracuse, New York on May 30, 1995. She grew up in Pompey, New York and graduated from Fabius-Pompey High School in 2013. She attended Dartmouth College and graduated in 2017 with a Bachelor's degree in Earth Science. In the fall of 2017, she entered the Quaternary and Climate Studies graduate program at the University of Maine Climate Change Institute. After receiving her Master's degree, Erin plans to pursue a career path in science writing to increase public awareness of, and advocacy for, the climate sciences. In her free time, she enjoys spending time outside—specifically, running, skiing, hiking, or just relaxing in her hammock with a book. Erin is a candidate for the Master of Science degree in Quaternary and Climate Studies from the University of Maine in August 2019.